

UC Riverside

UC Riverside Electronic Theses and Dissertations

Title

Electrochemical Synthesis of One-Dimensional Nanostructures for Sensor and Spintronic Applications

Permalink

<https://escholarship.org/uc/item/9ct388k0>

Author

Hangarter, Carlos Maldonado

Publication Date

2009

Peer reviewed|Thesis/dissertation

UNIVERSITY OF CALIFORNIA
RIVERSIDE

Electrochemical Synthesis of One-Dimensional Nanostructures for
Sensor and Spintronic Applications

A Dissertation submitted in partial satisfaction
of the requirements for the degree of

Doctor of Philosophy

in

Chemical and Environmental Engineering

by

Carlos Maldonado Hangarter

December 2009

Dissertation Committee:

Dr. Nosang V. Myung, Chairperson

Dr. Ashok Mulchandani

Dr. David Kisailus

Copyright by
Carlos Maldonado Hangarter
2009

The Dissertation of Carlos Maldonado Hangarter is approved:

Committee Chairperson

University of California, Riverside

ACKNOWLEDGEMENT

I would like to thank all my friends and family for their support and encouragement. Most of all I would like to thank my wife Sandy and daughter Tatiana. They fill my heart with heart with joy and inspired me to discover and achieve with creativity and imagination. Their friendship and love are invaluable and make my life complete. Thank you Sandy for also being my closest colleague and friend.

I also want to extend my gratitude to all of my labmates, past and present, for their friendship and assistance on all matters. In particular I would like to thank Sandip, Kumar, Mangesh, Mubeen, Ting, BY, Paul, Sylvia, Fang, Feng, Jae-Hong, Nicha, Hyunsung, and Young for the knowledge they have imparted and for taking the time from their own endeavors to assist me in my work.

Of course, none of this work would have been possible without the guidance of my advisor Dr. Nosang V. Myung, whom I am indebted to for teaching me first-hand the underlying theory and laboratory techniques of my research. His ingenuity and resourcefulness have educated me with a new approach to problems not only in the lab but in life as well. His strong work ethics push his students to excel and his interest in their careers has enabled them to achieve their goals.

The text of this dissertation, in part, is a reprint of the material as it appears in the following papers. The corresponding author Nosang V. Myung listed in these publications directed and supervised the research which forms the basis for this dissertation.

1. Carlos M. Hangarter, Mangesh Bangar, Sandra C. Hernandez, Wilfred Chen, Marc Deshusses, Ashok Mulchandani, and Nosang V. Myung, “Maskless Electrodeposited Contact for Conducting Polymer Nanowires”, *Applied Physics Letters*, 2008, 92, 073104.

ABSTRACT OF THE DISSERTATION

Electrochemical Synthesis of One-Dimensional Nanostructures for
Sensor and Spintronic Applications

by

Carlos Maldonado Hangarter

Doctor of Philosophy, Graduate Program in Chemical and Environmental Engineering
University of California, Riverside, December 2009
Dr. Nosang V. Myung, Chairperson

One-dimensional (1-D) nanostructures, such as nanowires and nanotubes, are attractive building blocks for electronics because of their small sizes, which provide for extremely high density devices, and their unique properties that emerge from their diminutive sizes and increased surface to volume ratios. In addition their extremely high aspect ratios offer researchers the potential to build striped and coaxial structures with different components aligned along the cylindrical or radial axis of the wire, respectively. Composition modulation can be used to incorporate multiple functionalities from intrinsic properties of the material or through interfacial phenomena. However, spatial manipulation and the ability to assemble and position nanostructures in a controlled manner so they are registered to lithographically defined contacts is a critical step toward scalable integration in high-density nanodevices. In this dissertation a generalized

template directed approach with ancillary assembly, contact, and displacement techniques were utilized to synthesize and characterize individual nanostructures from uniquely configured conducting polymer, magnetic, and semiconductor nanomaterials for sensor and spintronic applications.

Conducting polymers are particularly appealing because they exhibit tunable transport characteristics along with electronic, magnetic and optical properties of metals or semiconductors while retaining the attractive mechanical properties and processing advantages of polymers. In the first part of this work single component conducting polymer nanowires were electropolymerized, dielectrophoretically assembled, and contacted via maskless electrodeposition. Maskless electrodeposition was developed to selectively electrodeposit material on prefabricated microelectrode, embedding the nanowire ends. Two different conducting polymers were investigated, polypyrrole (PPy) and polyethylenedioxythiophene (PEDOT). Individual PPy nanowire devices demonstrated enhanced sensitivity to ammonia vapors, and PEDOT nanowire devices exhibited strong responses to volatile organic compounds. The gas sensing performances of these single nanowire devices were tuned by dopant type and synthesis conditions. Alternatively, single PEDOT nanowire devices were also completely coated in ferromagnetic material by implementing non-selective electrodeposition. The magnetoresistance (MR) of these devices displayed anomalous behavior, drastically deviating from typical anisotropic magnetoresistance responses. Additionally, multi-segmented noble/oxidizable nanowires were electrodeposited and subjected to galvanic displacement to create nanopeapod devices with Au peas and Te pods.

TABLE OF CONTENTS

Chapter 1: Introduction	1
1.1 Introduction.....	1
1.2 Conducting Polymers Nanosensors	2
1.2.2 Physical and Chemical Properties.....	4
1.2.3 Conducting Polymer Gas Sensor Background.....	5
1.3 Ferromagnetic Nanotubes	12
1.4 Nanopeapods.....	13
1.5 Research Objectives.....	15
Chapter 2: Individual Polypyrrole Nanowire Ammonia Sensor.....	18
Abstract.....	18
2.1 Introduction.....	19
2.2 Experimental Details.....	20
2.3 Results and Discussion	22
2.4 Conclusions.....	26
Chapter 3: Tuning the Sensing Performance of Single PEDOT Nanowire Based Gas Sensors	31
Abstract.....	31
3.1 Introduction.....	31
3.2 Experimental Details.....	34
3.3 Results and Discussion	39

3.3.1 Nanowire Synthesis and Device Fabrication	39
3.3.2 Electrical and Sensing Properties.....	43
3.4 Conclusions.....	50
Chapter 4: Anomalous Magnetoresistance of Ferromagnetic Nanotubes.....	61
Abstract	61
4.1 Introduction.....	62
4.2 Experimental Details.....	65
4.3 Results and Discussion	67
4.4 Conclusions.....	70
Chapter 5: Synthesis of Nanopeapods by Galvanic Displacement of Segmented Nanowires	78
Abstract	78
5.1 Introduction.....	79
5.2 Experimental Details.....	81
5.3 Results and Discussion	84
5.4 Conclusions.....	90
Chapter 6: Summary and Conclusion	107
Appendix 1: Pulsed Electrodeposition of Ni ₈₀ Fe ₂₀ /Cu Multilayer Nanowires	110
A1.1 Experimental Details.....	110
A1.2 Results.....	112

References..... 123

LIST OF FIGURES

- Figure 1.1: Schematic of template directed synthesis of conducting polymer nanowires, starting with a (A) nanoporous template (B) sputtering a gold seed layer (C) electrodeposition of the sacrificial layer and subsequent nanowire electropolymerization, (D) removal of the seed layer and sacrificial layer, and (E) dispersion of the nanowires. 17
- Figure 2.1: (Top): Optical images of a single PPy nanowire on gold electrodes before (left) and after (right) maskless electrodeposition of nickel. Scale bar represents $3\mu\text{m}$. (Bottom): (Left) Corresponding schematic of loosely bound nanowire crossing two gold microelectrodes. (Right) Selective maskless electrodeposition of metal (green) on electrodes to embed the nanowire for better electrical and mechanical contact..... 27
- Figure 2.2: SEM micrographs of DS-PPy nanowires on electrodes after maskless nickel electrodeposition at (a) -0.7V , (b) -0.8V , (c) -0.96V , and (d) -1.1V at a constant charge density of $3.53\text{C}/\text{cm}^2$. (scale bars represents $1\mu\text{m}$). The R/R_0 ratio (e) as a function of applied deposition potentials and (f) initial resistance for contacts deposited at -0.96V 28
- Figure 2.3: SEM micrographs of single polypyrrole nanowires after electrodeposition of (B) Ni, (C) Au, and (D) Cu at -0.96V , -0.5V , and -0.025V vs. Ag/AgCl, respectively. All scale bars represent $2\mu\text{m}$ 29

Figure 2.4: Sensor response of a loosely bound (a) and an embedded (b) single DS doped PPy nanowire as a function of different NH₃ concentrations. (c) The sensitivity of a loosely bound (■) and embedded nanowire (●)..... 30

Figure 3.1: Cyclic voltammograms of each PEDOT bath (A) PP1, (B) PC1, and (C) PC2 with and without the EDOT monomer..... 52

Figure 3.2: (A) Plot of the growth rate as a function of applied potential vs. a nonaqueous reference electrode for each PEDOT bath. (B) The nanowire length (μm) per unit charge density is plotted as a function of potential vs. a nonaqueous reference electrode for each bath. In both graphs the error bars represent standard deviations based on seven samples. 53

Figure 3.3: TEM images of (A, B) PP1, (C, D) PC1, and (E, F) PC2 nanowires..... 54

Figure 3.4: (A-B) Schematic of maskless electrodeposition, starting with a single aligned nanowire with selective electrodeposition of Au on the electrodes with no deposition on the PEDOT nanowire. (C) The resulting single nanowire structure was imaged with SEM. The current-voltage response for (A) PC2, (B) PC1, and (C) PP1 are shown before and after maskless electrodeposition. 55

Figure 3.5: (A) Normalized Arrhenius plot of single PEDOT nanowires for each of the three baths. The slopes of the lines indicate activation energies of 42, 120, and 304meV for PEDOT/PSS, PEDOT/ClO₄⁻ (mixed bath) and PEDOT/ClO₄⁻ (MeCN) nanowires, respectively (B) Temperature coefficient of resistance for the

same nanowires as function of temperature. The inset magnifies low TCR values.	56
Figure 3.6: Reduced activation energy for single nanowires from the three different electropolymerization baths.....	57
Figure 3.7: Normalized sensing profiles for single (A, D, G, J) PP1 (B, E, H, K) PC1 and (C, F, I, L) PC2 nanowires in response to (A-C) acetone, (D-F) water, (G-I) methanol, and (J-L) ethanol. The analyte exposures are reported in percent of their saturation concentrations with their scale shown only to the right of (C, F, I, L).....	58
Figure 3.8: Normalized responses for single (A, B) PP1, (C, D) PC1 and (E, F) PC2 nanowires to several VOCs and humidity at room temperature and a flow rate of 500 sccm. The $\Delta R/R_o$ scale is kept the same for visual comparison and the key for all plots is shown in (A).	59
Figure 3.9: Histogram of nanowire sensitivity to each analyte. The break was inserted to illustrate the relative sensitivity of most nanowire-analyte interactions in comparison to that of PC2 to both acetone and MEK.	60
Figure 4.1: SEM images of Ni nanotubes with room temperature resistances of (A) 25 Ω , (B) 15 Ω , and (C) 7 Ω . (D) A Ni ₃₀ Fe ₇₀ nanowire with a room temperature resistance of 29 Ω . All scale bars represent 2 μ m.....	72

Figure 4.2: Temperature coefficient of resistance for Ni nanotubes	73
Figure 4.3: Magnetoresistance characteristics of PEDOT/Ni core/shell nanostructure Measured at (a) 10, (b) 100, (c) 200 and (d) 300 K. (//; longitudinal and \perp : transverse direction).....	74
Figure 4.4: Temperature dependent MR properties for Ni thin films, nanowires, and nanotubes. Filled and open shapes correspond to transverse and longitudinal MR measurements, respectively.	75
Figure 4.5: Angle dependent magnetoresistance of (A) Ni and (B) Ni ₃₀ Fe ₇₀ nanotubes at 10K. The inset illustrates the MR hysteresis and minimums at low fields.....	76
Figure 4.6: Magnetoresistance for an (A) as-synthesized Ni nanotube (14 Ω) and after etching to (B) 31 Ω and (C) 87 Ω . MR curves are red and black for longitudinal and transverse direction, respectively.	77
Figure 5.1: Schematic of galvanic displacement reaction progression for Co/Au multisegmented nanowires. (A) The as synthesized Co/Au nanowire is (B) sheathed in a thin porous Te coating (C) that permits continued dissolution of the Co segments as the Te coating continues to grow, (D) until the Te tube with embedded Au particles is all that remains.	92
Figure 5.2: SEM images of (A) electrodeposited Co/Au multisegmented nanowires and (B, C) the corresponding Au/Te nanopeapod structure synthesized by galvanic	

displacement. (D) The EDX spectrum of image (C) indicates the presence of Te and no detectable concentration of Co. Additional peaks pertain to the Au segments, 2.12 keV, and substrate materials, Cu 8.04 keV and Al 1.48 keV..... 93

Figure 5.3: TEM images of (A-B) Co/Au multisegmented nanowires and (C-D) Te/Au nanopeapods. EDX and SAED patterns for Co/Au nanowires (E-F) before and after (G-H) galvanic displacement are also shown. Scale bars are 20nm and 200nm for (C) and (A, B, D), respectively 94

Figure 5.4: TEM images of Au/Te nanopeapods produced from a 30nm polycarbonate template. Scale bars are clearly indicated..... 95

Figure 5.5: SEM images of Ni/Au nanowires fabricated from (A) 200nm alumina templates and (C) 30nm polycarbonate membranes. The coated structures after galvanic displacement are shown in (B) and (D) for alumina and polycarbonate, respectively. The insets of (A-B) are EDX patterns for their corresponding images. (E-F) SEM images of (E) 200nm Ni/Au and (F) 50nm galvanically displaced Ni/Au nanowires with different segment lengths. Scale bars (A) 10, (B-C, E) 5, (D) 1, and (F) 0.2 μ m. 96

Figure 5.6: (A-B) Darkfield and (C-D) brightfield TEM images of Ni/Au nanowires. (A) The EDX line scan confirms segment contrast for (red) Ni and (blue) Au. (D) The brightfield TEM images corresponds to the (E-F) SAED patterns below. Scale bars (A) 1, (C) 0.5, and (B, D) 0.1 μ m. 97

Figure 5.7: (A-F) Brightfield TEM images of Ni/Au multisegmented nanowires synthesized from a 50nm polycarbonate template after galvanic displacement. The boxes in (C) correspond to the images in (D-F) and SAED patterns in (G-I). The SAED patterns (J), (K), and (L) are the exact same SAED patterns as (G), (H), and (I), respectively, with numbered spots and corresponding white rings for d-spacing values in Table 5.2 and 5.3. The scale bars are (A-B) 100, (C) 10, and (D-F) 2nm. 99

Figure 5.8: (A-C) Darkfield TEM images of Ni/Au nanowires fabricated with 50nm polycarbonate templates and subjected to galvanic displacement reaction with Te. The box in (C) indicates the area of the EDX mapping for (D) Te, (E) Au, and (F) Ni. Scale bars are (A) 200, (B) 20, and (C) 400nm. 103

Figure 5.9: (A-E) Brightfield TEM images of Ni/Au multisegmented nanowires from 30nm polycarbonate template after galvanic displacement. The boxes in (A) correspond to the images in (B-E) and SAED patterns in (F-K). The SAED patterns (I), (J), and (K) are the exact same SAED patterns as (F), (G), and (H) respectively, with numbered spots and corresponding white rings for d-spacing values from Tables 5.4 and 5.5. The scale bars are (A) 10 and (B-E) 2nm. 104

Figure A1.1: SEM images of (A) 200nm and (B) 30nm Au/NiFe/Au nanowires embedded in an alumina template..... 115

Figure A1.2: (A) Fe content, (B) magnetization saturation, (C) coercivity, and (D) squareness (M_S/M_R) as a function of the $[Fe^{+2}]/[Ni^{+2}]$ ratio in the electrodeposition bath for $1\mu\text{m}$ NiFe nanowires electrodeposited at 1.4 and 1.2 V. 116

Figure A1.3: The deposition content as a function of the $[Cu^{+2}]$ for NiFe/Cu multilayer baths. 117

Figure A1.4: (A) Linear sweep voltammogram and for the permalloy bath with 0, 1, and 10mM Cu^{+2} . The inset contains the full potential range of the voltammogram. (B) The polarization curve (semi-log plot) of the current density as function of the potential is used to determine the range of Cu electrodeposition. 118

Figure A1.5: SEM images of $Ni_{80}Fe_{20}/Cu$ multilayer nanowires electrodeposited with a charge density of 0.1204 and 0.03896 C/cm^2 , respectively, from baths with (A) 1, (B) 5, and (C) 10mM $[Cu^{+2}]$. The Cu was selectively etched to permit layers to be distinguished. The insets contain lower magnification of template cross-section for the same sample. The scale bars are (A) 1 and (B-C) $2\mu\text{m}$ 119

Figure A1.6: The chronopotentiogram for $Ni_{80}Fe_{20}/Cu$ multilayer electrodeposition shown at (A) small and (B) large current density scales for Cu and $Ni_{80}Fe_{20}$, respectively. 120

Figure A1.7: (A) SEM and (B-C) TEM images of $Ni_{80}Fe_{20}/Cu$ multilayer nanowires electrodeposited with a charge density of 0.01204 and 0.003896 C/cm^2 ,

respectively. The Cu was selectively etched in (A) to permit layers to be distinguished. The insets contain lower magnification of the same (A) template cross-section and (B) single nanowire sample. The scale bars are (A) 500, (B) 100, and (C) 10nm. (D) The SAED pattern corresponds to wire in (C). 121

Figure A1.8: (A) SEM image of a single $\text{Ni}_{80}\text{Fe}_{20}/\text{Cu}$ multilayer nanowire device. The inset is a lower magnification image of the device. (B) The magnetoresistance profile of the device. 122

LIST OF TABLES

Table 1.1: Comparison of chemical structures and electrical conductivities of selected conducting polymers.....	16
Table 5.1: D-spacing values for the numbered spots from Figure A1.2 (F) and corresponding element, plane, and unit cell edge length (a).....	98
Table 5.2: D-spacing, plane and unit cell edge length for Te from Figure 5.8 (I, L).	100
Table 5.3: D-spacing, plane and unit cell edge length for Au from Figure 5.8 (H, K)...	101
Table 5.4: D-spacing, plane and unit cell edge length for NiTe from Figure 5.8 (I, L).	102
Table 5.5: D-spacing, plane and unit cell edge length for Te from Figure 5.10 (I).....	105
Table 5.6: D-spacing, plane and unit cell edge length for NiTe from Figure 5.10 (I)....	105
Table 5.7: D-spacing, plane and unit cell edge length for Au from Figure 5.10 (K).....	106

Chapter 1: Introduction

1.1 Introduction

One dimensional (1D) nanostructures, such as nanowires and nanotubes, are critically important building blocks of nanotechnology for two reasons. First, their high aspect ratios and quasi-1D features are appealing for integration in high-density devices, giving rise to electronic devices that are lighter, more compact, and portable. Second, nanostructures begin to exhibit unique properties that diverge from the bulk due to quantum confinement effects, which translates to tunable behavior by control of shape and diameter.^{1,2} These features are crucial for enhancing and realizing applications such as nanoelectronics, spintronics, optoelectronics, sensors, and thermoelectric devices.

Furthermore, nanowires/tubes can be further complexed with axial and radial interfaces, for segmented, multilayered and core/shell structures. These intricate constructs can display novel properties due to interfacial and geometric characteristics. Their synergistic attributes usually arise due to marked differences in nanomaterial properties such as electron spin, work function, or carrier type. Consequently, heterostructures such as ferromagnetic/nonmagnetic, metal/semiconductor, and p-/n-type semiconductors have roused interest in the materials and nanoscience communities.³⁻⁶ Hybrid organic/inorganic nanostructures have attracted interest for similar reasons in addition to their added benefits of processability and robust mechanical properties.

However, to fully exploit these higher level configurations, nanomaterials must be engineered for specific properties and interfacial characteristics that give rise to enhanced

functionalities for communications, data storage, logic operations, sensing, and energy conversion. This ardent task requires a fundamental understanding of the synthesis approach on the structure-property relationship as well as size and shape dependent effects. Yet the true values of these physical properties are not always accurately measured at this level, as many can only be assessed by interrogation of individual nanostructures.⁷ Additionally, the commercialization of nanowire-based devices has been severely stunted by stunted by controllable integration, including alignment and contact, into existing technologies. Rational assembly and electrical contact are therefore not only crucial to nanomanufacturing, but are also necessary to interrogate true properties of single nanowires. This is especially applicable to nanowire/tube sensors and magnetic materials, as unpredictable nanowire-nanowire and nanowire-electrode contacts can diminish signals and magnetic interactions with neighboring nanostructures can obscure transport measurements, respectively.

Single nanowire/tube device fabrication is thus essential to measuring and nanoengineering the unique properties of 1D elements and is reviewed in the context of this chapter for conducting polymer nanosensors, hybrid polymer/ferromagnetic core shell nanowires, and metal/semiconductor nanopeapods.

1.2 Conducting Polymers Nanosensors

Conducting polymers (CPs) are unique materials because they exhibit electronic, magnetic and optical properties of metals and semiconductors while retaining the attractive mechanical properties and processing advantages of polymers.⁸ These features,

along with chemical sensitivity and tunable charge transport properties, have launched conducting polymers as a major class of chemical transducers, creating powerful thin films sensors for over two decades. Additionally, their chemical and physical properties (optical and electrochemical) are conducive to several sensor modalities. Traditionally, various sensor modes provided a tradeoff among sensor performance parameters, sensitivity and selectivity vs. response time and portability, however nanosensors are now facilitating overall device enhancement. Among the conducting polymer sensing modes poised to exploit nanoscale enhancements, chemiresistive platforms are perhaps the most rigorously studied because of their ease of fabrication and demonstrable improvement in sensitivity and response time.^{9, 10} These features are a consequence of dramatic decrease in characteristic length and increase in the ratio of surface to volume atoms, allowing for rapid diffusion into the bulk and for a more significant fraction of the atoms to participate in surface processes such as chemical/biological binding interactions.^{10, 11} Additionally, the Debye length, which is a measure of electric field penetration into the bulk of the material, is comparable to the diameter of the nanowire permitting charged adsorbates to impose a stronger influence on charge carrier transport. One-dimensional geometries also enhance response times by virtue of their two-dimensional mass transfer profile.¹² Furthermore, nanowires are heralded for device miniaturization and sensor arrays, enabling duplicate elements to reduce false positives/negatives and pattern recognition systems termed electronic noses/tongues where each sensor in the array has a unique response to every analytes creating a fingerprint type response that increases sensitivity and selectivity. Finally, conductometric sensors are also attractive for their proven

commercial viability, as this approach uses a single material behaving as both the sensitive layer and transducer to directly convert chemical information into an electronic signal without the need for labels, allowing for real-time and continuous monitoring.

1.2.2 Physical and Chemical Properties

Conducting polymers are repeat sequences of monomer units that contain π -conjugated backbones. The sp^2 hybridized structure gives rise to their conductivity, however, pristine CPs are insulating or semiconducting at best, and require the addition of dopants, typically anions, to achieve high conductivity. Oxidative radical polymerization induces positive charge in the polymer backbone, and hence most CPs are p-type semiconductors, that facilitate charge transport usually by polaron or bipolaron carriers. The chemical structures of the most commonly studied CPs are shown in Table 1 along with their conductivity ranges. Conducting polymers are typically amorphous or disordered materials composed of one-dimensional chains with both polydispersity and conformation. The disorder of CPs is highly dependent on the synthesis route and conditions and has been correlated to charge transport models. Although charge transport behavior is dominated by hopping or tunneling between chains, both inter- and intra-chain transport contribute to the overall conductivity. Chemicals that interfere with any of these transport processes can be conductometrically detected.

The addition of functional groups has also played several roles in the development of CPs. Thiophene, for example, has improved stability and decreased oxidation potentials by the addition of an alkylenedioxy substituent to the 3 and 4 positions, preventing cross linking or oxidation that can occur at these positions. Additionally,

side-chain functional groups, as in poly-3alkylthiophenes (P3ATs), have been utilized to induce longer conjugation lengths by inhibiting 2-4 linkages via steric hinderances. However the asymmetry introduced in the monomers can yield different regioregularities, head-to-tail vs. head-to-head and tail-to-tail linkages, which affect the planarity of the polymer, disrupting the π -conjugation and hence reducing the conductivity. Nevertheless highly regioregular P3ATs can produce more efficient chain packing for conductivities several orders of magnitude greater than their parent structure. Side chains and functional groups have also been recently involved in efforts to tailor CP affinity for different volatile organic compounds (VOCs).^{13, 14} While many of these derivative CPs have yet to be applied to nanosensors, their role in future directions and combinatorial efforts with nanostructured CPs will be important.

1.2.3 Conducting Polymer Gas Sensor Background

Gas sensors have become ubiquitous components in our lives, actively involved in the operation of the vehicles we drive, continuously monitoring air quality in our homes and place of employment, and enabling industrial process control/emission compliance. Recent advances have also spurred interest for medical diagnosis, agriculture/food processing applications, and efforts in long term environmental analysis. Expansion within existing fields and breadth of impact on emerging fields is largely contingent on anticipated improvements in portability, reliability, performance, and affordability of nanosensors. Although these improvements will rely on several technologies, CP nanosensors are among the most promising materials due to their bulk penetration by analytes and tunable selectivities/sensistivities.

The first demonstrations of conducting polymer gas sensors typically employed thick/thin films of PPy, PANI, PT, and their derivatives. These early experiments provided substantial insight on the utility of these sensing materials and the dominant mechanisms governing their performance. In general polar molecules were found to dope/dedope (oxidize/reduce) CPs resulting in a decrease/increase in resistance. VOC's absorb into the polymer causing conformational changes, either swelling or alignment of the chains. Swelling increases the average hopping distance between chains and therefore increases the resistance, while chain alignment increases the crystallinity, decreasing the resistance.^{15, 16} These interactions are reversible except in the case of chain alignment, in which a permanent conformational change is induced in the structure.⁸

Unlike traditional inorganic sensory materials, conducting polymers exhibit an innate porosity and rich collection of morphologies that are not only highly dependent on the monomer and synthesis route but were also shown to significantly affect their sensitivity and response times.^{17, 18} In many ways the first conducting polymer nanosensors were variants of these highly porous thin films or nanomeshes containing ligands of controlled nanoscale diameters. These nanofiber based sensors were polymerized both chemically and electrochemically with unique features to each approach.¹⁹⁻²² While chemically synthesized PANI nanomeshes exemplified the potential of nanostructured conducting polymer, these particular devices were subject to manufacturing and integration limitations, particularly in terms of adhesion and electrical contact. This is a continuing challenge with drop cast materials, sacrificing robust design

for facile synthesis, which has favored electropolymerization since nascent studies with thin films.

Although the practice of electropolymerizing nanostructured CPs was first studied by Martins group via template directed methods, Ramanathan et al. were the first to report functional CP nanowires using an in situ procedure to exploit the site specific nature of electrodeposition.²³ Shortly after, Tseng's group developed conducting polymer nanoframework junctions (CPNEJ) by electrochemical growth of PANI nanofiber networks from one microelectrode to the other. PANI CPNEJs displayed marked similarity with the sensing results from Kaner's aforementioned chemical route, but are more universal in that CPNEJs have been applied to liquid media sensing and were synthesized from other polymers such as PPy and PEDOT.²⁴

Most recently, a variation of this approach was applied toward the synthesis of Au nanoparticle decorated PANI nanofiber networks. The Au nanoparticles, electrodeposited by cyclic voltammetry, improved the sensitivity to H₂S by over four orders of magnitude with a remarkable lower detection limit of 100 ppt and impressive dynamic range (Figure 2).²⁵ These results are an elegant demonstration of deterministic CP hybridization for tailored sensing properties. This tunable sensing behavior is a key feature of nanostructured CPs that would benefit from combinatorial schemes to probe the effects of dopant level, dopant type and hybrid CP nanostructures.

Despite the improved sensitivity and ease of fabrication for random nanofiber networks, they forfeit true two-dimensional diffusion profiles that give rise to unprecedented temporal and spatial resolution, a specific objective in the pursuit of

miniaturization. The first study of individually addressable conducting polymer nanowire gas sensors was performed by Liu and coworkers.¹⁰ The results provided definitive proof of diameter dependent response times, accurately described by a diffusion equation for a cylinder, with a well defined dynamic range and reproducibility. The unique feature of this approach was the use of four point contacts, imparting the most precise electrical measurements by drastic reduction, if not elimination, of contact resistance, to establish key phenomenological aspects of single conducting polymer nanowires gas sensors. Unfortunately, the shortcoming was lack of manufacturability, utilizing a rotating substrate, with no indication of rational assembly, while depositing electrospun nanowires.

The substantiated utility of one-dimensional conducting polymer nanostructures still faces many scaling and manufacturing hurdles, but recent efforts have recognized the dilemma of randomly assembled nanosensors, unpredictable nanowire-electrode and nanowire-nanowire contact, and have made strides to this end. Most notably, assembly and integration schemes for template directed electrodeposited conducting polymer nanowires have been pursued by several researchers. This synthesis technique consists of a nanoporous template, usually polycarbonate or anodized alumina, to form nanowires within, followed by template removal to release the nanowires in solution as shown in Figure 1. The template provides fine control over the diameter and electrodeposition time/charge regulates the length. This process has been used to fabricate single component conducting polymer nanowires and multisegmented nanowires with densities of 10^{11} cm^{-2} , wherein functionality is integrated into each segment.

Naturally, one of the first demonstrations of gas sensing by an individual template directed CP nanowire consisted of a drop cast PPy nanowire bridging two prefabricated microelectrodes.²⁶ This free-standing nanostructure very likely suffered from instabilities in contact with the electrode that created high noise with a lower detection limit for NH₃ of only 40 ppm. In an alternate scheme Ni and Au segments were incorporated for magnetic assembly and electrical contact, respectively.²⁷ Although the approach showed promise the device performed poorly against the only analyte tested, NH₃, probably due to polymer reduction during electrodeposition of Ni on PPy.

In this respect, Mallouk's group developed an approach to fabricate Au/CP/Au segmented nanowires that preserved the electrical behavior of the polymer by preceding electrodeposition of Au onto the CP with an electroless seed layer.²⁸ Individual Au/PEDOT/Au nanowires were AC dielectrophoretically assembled to prefabricated microelectrodes with a serial capacitor to self-terminate assembly after bridging a single nanowire. These single wire sensors were exposed to several VOCs, displaying low sample to sample variation and excellent reproducibility.²⁹ The same process was later implemented to distinguish dopant-dependent transport properties and correlate them with their corresponding sensing properties.³⁰ Low temperature four point contact measurements provided a neat fit of the nanowire transport behavior to existing models.

A host of novel fabrication schemes have also shown promise in terms of manufacturability and/or application towards gas sensing. Briefly these include block copolymer lithography, dip pen nanolithography (DPN), and nanoimprint lithography.^{9, 31-34} The block copolymer litho was used to produce the highest density array of

PEDOT/PSS nanowires to date with a width and pitch of 15 and 30nm, respectively. These wires produced somewhat conflicting sensing results when compared to analogous thin films; sensitivities at low concentrations of ethanol were nearly identical while nanowire arrays demonstrated improvement at higher concentrations. Since CP sensitivity to gaseous analytes is a bulk property these results were rationalized in terms of a surface conformation/composition change due to the copolymerization process and kinetic limitations of thicker films. DPN has achieved analogous nanostructure resolution with several CPs,^{35, 36} but few papers report application towards gas sensing. Two different approaches have been investigated for nanoimprint lithography of CPs, an embossing technique and a lift-off process. Embossing fluidizes CPs, by thermal or solvent treatment, to physically transfer features from a hard mold onto the CP thin film. Although this embossing procedure was not applied to gas sensing, this technique was used to tune the chain alignment of PPy nanowires by width of the nanowire arrays, providing a combinatorial approach to conformation driven sensor performance. Alternatively, Fuchs group has developed adhesion promoters, surface treatments and a copolymer strategy, to improve lift-off lithography resolution/compatibility with CPs.^{9, 31, 32} The devices displayed a general increase in sensitivity to NH₃ with decrease wire width, which was not fully addressed but may be attributed to film inhomogeneities or confinement effects induced from the substrate anisotropy during chemical polymerization.^{37, 38} Although these are a few select reports, further charge transport measurements in general are needed to correlate size dependent shifts in CP nanosensor

performance to structural changes (e.g. disorder). This avenue of research could differentiate effects of synthesis route and aid in the design of future sensor devices.

A number of approaches now exist for the fabrication of conducting polymer nanosensors. While each has demonstrated its own subtle advantage and disadvantages, what differentiates these techniques is their potential to generate heterogeneous arrays of individually addressable nanosensors. This is a critical feature for E-nose devices or advanced gas sensors with multi-analytes recognition. This constraint can only be met with in-situ electropolymerization techniques and assembled nanowire devices. Recently, a system of sequential nanochannel electrodepositions and a pattern transfer technique were utilized to create an array of PPy, PT and PEDOT nanowires.³⁹ While this approach requires a series of steps, which appears time consuming and not likely competitive on a cost-benefit analysis, it is an important stride towards high density heterogeneous CP nanowire arrays. The key to their process was integration of several nanoscale fabrication techniques. Future directions for heterogeneous arrays will also likely include post synthesis modification, favoring electrochemical routes for their site specificity, to alter individual elements.⁴⁰

Through these preliminary studies on CP nanowire based chemiresistive or FET based sensors, the utility of one-dimensional CP nanostructures has been established. The significance of fabrication route and electrical integration were discussed with a variety of in-situ and ex-situ techniques. The nanoscale enhancement of temporal and spatial resolution was illustrated with single nanowire devices. Although CP gas sensitivity is generally understood as a bulk property, several examples connote synthesis

route dependent surface/interface inhomogeneities or confinement effects that give rise to greater sensitivities with decreasing size. Additional efforts should emphasize structural characterization by charge transport models or spectroscopic data to better understand features of CP nanosensors that give rise enhanced sensitivities. Future efforts to augment the role of these nanosensor materials should focus on novel fabrication schemes and post-synthesis routes to fully utilize the catalogue of available monomers and dopants for the production of high density, heterogeneous CP arrays.

1.3 Ferromagnetic Nanotubes

Since the discovery of giant magnetoresistance (GMR) in 1988, magnetic trilayers have formed the basis of spintronics, enabling simultaneous manipulation of electron charge and spin. This interface dependent technology is highly scalable and was responsible for the hard drive density explosion in the late 1990's.⁴¹ The spin valve, a sandwich structure with a magnetically pinned and free layer separated by a nanometers thin nonmagnetic layer, is the canonical structure for these devices that have become ubiquitous components of the information age.⁴² Today, spintronics are considered a viable platform for computer logic or solid state memory due to its non-volatility, low power requirements, fast read/write times, and improved scalability with spin torque transfer.⁴³ Additionally, unique magnetic nanostructures have also led to the discovery of the spin torque diode effect, furthering the utility of spintronics to include radio frequency communications devices, with recent demonstration of spin-based microwave detectors and emitters.⁴⁴

Extending spin-dependent transport into novel ferromagnetic nanostructures, both in terms of materials and geometric configuration, is an important goal for continued maturation of this field. Although most attention is given to multilayer and spin valve structures, shape factors may also provide a promising route to manipulate magneto-transport properties due to domain wall behavior and magnetization processes.^{45, 46} In particular, high surface area nanotube structures may enable a wall thickness spin dependent transport. More complex geometric shape and size arrangements, such as core/shell hybrid ferromagnetic nanostructures, are also of interest due to magnetic shape anisotropy and interfacial properties that may induce technologically significant aberrations in their magneto-transport characteristics.

Unfortunately, the difficulty of synthesizing ferromagnetic nanotubes has limited characterization to arrays, usually embedded in an alumina template due to extensive oxidation that occurs during template removal, prohibiting electrical contact, and their relative fragility.⁴⁷ As a consequence, most groups are limited to optical and magnetic property measurements without the means to measure and report magneto-transport properties.

1.4 Nanopeapods

One of the key directives of nanoscale research is the development of advanced electronic, optoelectronic, and magnetic functionalities through manipulation of size, shape, interfacial and proximity effects. Of these routes, nanoscale interfaces and proximity can be pursued by two different approaches, assembly of individual

nanowires/tubes and the development of hierarchical nanoconstructs, which integrate material interfaces or separate components into the design of its physical structure. Traditional nanowire heterostructures, such as axial superlattices and radial core/shell structures, utilize continuous interfaces, either perpendicular or parallel to its transport direction, to consistently impose some magnetic, electrical or optical property.^{4, 41, 48} However, discontinuous interface systems, such as nanoparticles decorated/embedded nanowires/tubes, have recently attracted attention for enhancement of thermoelectric, sensing, and optoelectronic characteristics. These features are a consequence of the difference in physical properties of the materials at the interfaces and confinement effects of the nanoparticles, which have the ability to cause biased scattering of phonons, modulate charge carrier mobility/concentration due to interface scattering, and surface plasmon enhanced photocurrent.⁴⁹⁻⁵²

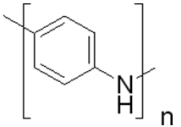
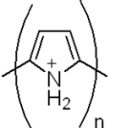
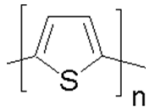
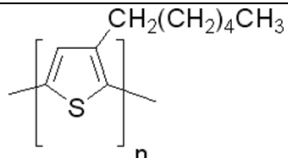
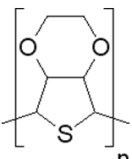
Although most demonstrations to date have explored indiscriminate distributions of decorated/embedded nanoparticles, rational control of nanoparticle size, aspect ratio, and placement can provide significant advantages over random systems, particularly for nanoparticle embedded nanotubes or nanopeapods. These features include precise control over opto/electronic properties and higher level functions such as plasmon waveguides via nanoparticle chains.⁵³ Nanopeapods also stand to gain significantly from synthesis schemes that allow more diverse palettes of materials to be explored and more interesting material combinations. However to date, nanopeapod synthesis approaches are confined to a small set of materials for both the pea (noble metal) and the pod (metal oxide) due to high temperature synthesis techniques.⁵⁴

1.5 Research Objectives

Based on the aforementioned discussion, the overall objective of this work was to synthesize unique one-dimensional nanostructures based on template directed electrodeposition and develop fabrication techniques to integrate and characterize individual nanostructures. The specific goals of this work were four fold.

1. Develop a simple and scalable method to create solid mechanical joints and electrical contact for conducting polymer nanowires to electrodes by selective maskless metal electrodeposition on electrodes.
2. Develop fabrication techniques for individual conducting polymer nanowire gas sensors. Characterize the electronic and sensing performance of these sensors based on monomer, dopant, and solvent.
3. Establish single nanowire processes for the design of polymer/ferromagnetic core/shell nanostructures and characterize the magneto-transport properties of said devices with respect to temperature, angle, and nanotube composition.
4. Investigate a generalized galvanic displacement reaction for synthesis of metal/semiconductor nanopeapods. Formulate specific conditions for the synthesis of Te/Au nanopeapods. Investigate nanopeapod synthesis with different nanowire diameters, segment lengths, and sacrificial metals.

Table 1.1: Comparison of chemical structures and electrical conductivities of selected conducting polymers

Conducting Polymer	Chemical Structure	σ (S/cm)
Polyaniline (PANI)		10^{-10} - 10^3
Polypyrrole (PPy)		10^{-5} - 10^3
Polythiophene		10^{-4} - 10^{-1}
Poly(3-hexylthiophene) (P3HT)		10^1 - 10^2
Poly(3,4-ethyldioxythiophene) (PEDOT)		10^{-2} - 10^3

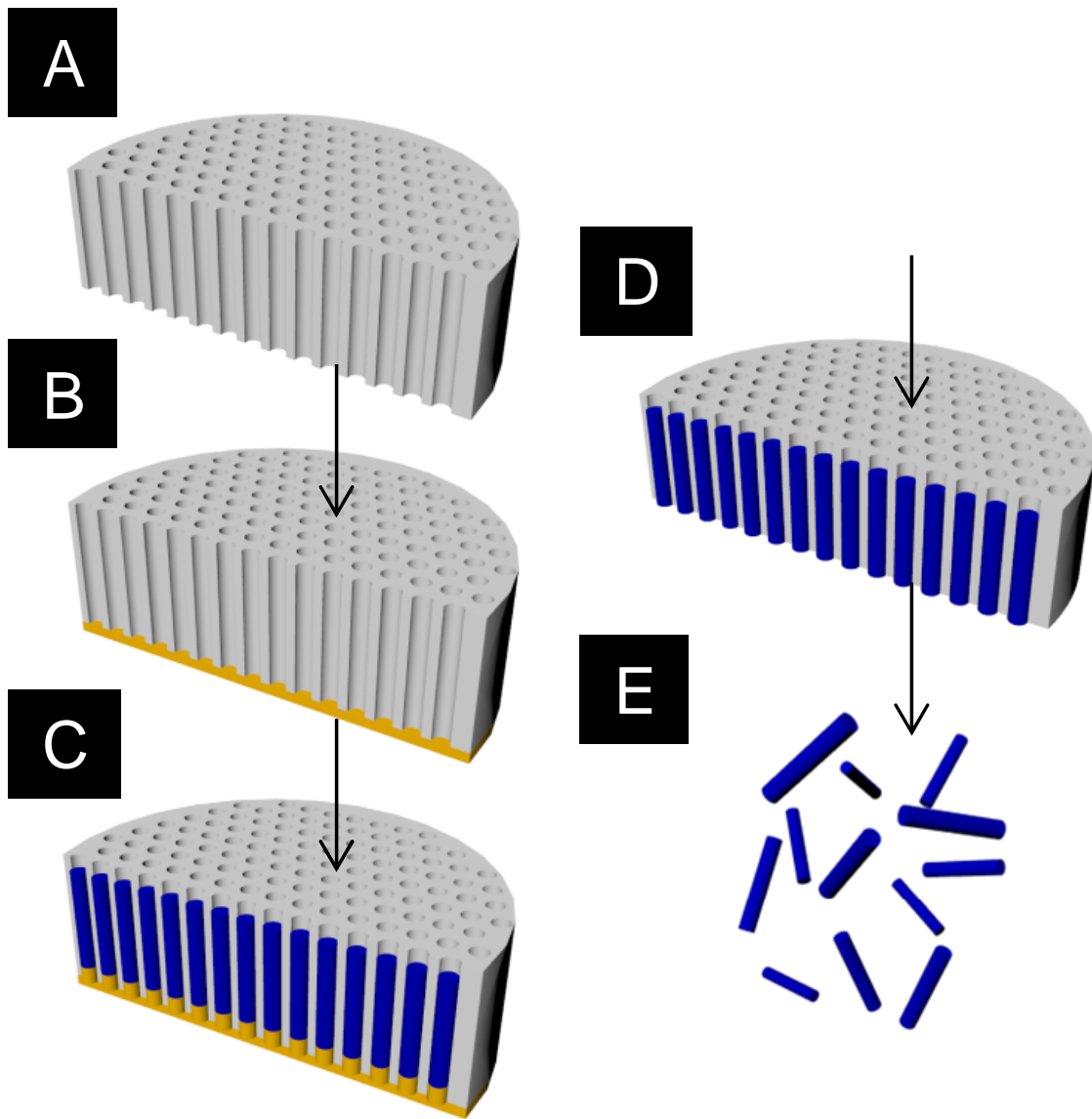


Figure 1.1: Schematic of template directed synthesis of conducting polymer nanowires, starting with a (A) nanoporous template (B) sputtering a gold seed layer (C) electrodeposition of the sacrificial layer and subsequent nanowire electropolymerization, (D) removal of the seed layer and sacrificial layer, and (E) dispersion of the nanowires.

Chapter 2: Individual Polypyrrole Nanowire Ammonia Sensor

Reproduced in part with permission from *Applied Physics Letters* 2008, 92, 07104.

Copyright 2008 American Institute of Physics.

Abstract

A simple and scalable method to create mechanical joints and electrical contacts of conducting polymer nanowires to electrodes by selective maskless metal electrodeposition on electrodes is reported. This is an attractive route for contacting conducting polymer nanowires as it bypasses harsh processing conditions of conventional methods used for inorganic materials. The basis of this approach is a potential window in which greater cathodic current exists for the microfabricated Au electrodes than the conducting polymer nanowire and that the cathodic current for the nanowire is primarily ionic. The applied potential and initial resistance of the nanowires was found to have a significant impact on the selectivity of maskless deposition. Different maskless electrodeposition baths, including Au, Ni, and Cu, and nanowire dopants, ClO_4^- and dodecyl sulfate, were also investigated to understand the polymer reduction during the maskless process. A single dodecyl sulfate doped polypyrrole nanowire with maskless electrodeposited nickel contacts was shown to have improved sensitivity toward ammonia gas.

2.1 Introduction

One-dimensional (1-D) conducting polymer nanostructures provide significant promise for miniaturized devices. The inherent properties of polymeric nanostructures are particularly suited for sensors because their mechanical flexibility, chemical sensitivity, room temperature operation and potential for high density arrays are ideal for compact portable platforms.¹⁰ While, various methods including lithography,⁵⁵ nanoscale solder,⁵⁶ focused ion beam (FIB),⁵⁷ and annealing,⁵⁸ have been investigated to contact inorganic nanostructures to electrodes, processing incompatibilities have excluded applying those methods to conducting polymer nanowires. For example, post-assembly contact of conducting polymer nanowires by lithography requires complex alignment procedures and exposure to harsh processing conditions, subjecting the nanowires to high intensity ultra-violet light, and organic solvents that may permanently degrade, stress, or dissolve organic nanowire surfaces.^{59, 60} The photoresist may also permeate the porous nature of some organic materials leaving difficult to remove residuals. Alternative serial patterning techniques such as FIB are costly with low-throughput and localized heating that may sever contact rather than promote it. Similarly, the high operating temperature for nanoscale solder may ultimately decompose these organics and does not provide the necessary palette of materials for ohmic contact with organics. Lastly, nanowires deposited on top of prefabricated electrodes are not exposed to extreme environments but are loosely bound with minimal contact area.

Here, selective maskless metal electrodeposition to electrodes is presented as a means to contact and embed the ends of polymer nanowires. This approach is amenable

to high throughput processing as electrodeposition is an easily scaled process compatible with the microelectronics industry.⁶¹ Several high work function materials, Cu, Ni, and Au, were investigated to achieve ohmic contact for p-type polymer semiconductors, such as the polypyrrole (PPy) nanowires studied here. The applied deposition potential, initial resistance of loosely bound interconnects, and bath compositions were found to be crucial parameters in controlling the deposition selectivity. Scanning electron microscopy (SEM) images and current-voltage (I-V) responses confirmed the nature of the selective electrodeposition of metal on the electrodes to completely embed the nanowire. The applied potential and dopant of polymer were also shown to impact reduction of the nanowire during cathodic electrodeposition of metals. Sensing of gaseous NH₃ using a single dodecyl-sulfate (DS) doped PPy nanowire was also demonstrated.

2.2 Experimental Details

The PPy nanowires were synthesized by template-directed electrodeposition, as pioneered by Martin^{62, 63}. This method uses a nanoporous membrane as a scaffold and a metallic seed layer on one side to serve as a cathode. These studies used commercially available anodized aluminum oxide membranes, Whatman Anodisc 13, with a nominal pore diameter of 200 nm. Anodic alumina is a rigid material that can withstand temperatures in excess of 600 °C and harsh chemical environments and can be produced with pores as small as 5 nm in diameter⁶². In addition, the high density, order, and aspect ratios of these membranes are ideal characteristics of nanowire templates. Gold seed layers were deposited by sputtering for six consecutive cycles using an Emitech K550

tabletop sputter coater at 20mA for 4 minutes. The nobility of Au was necessary to allow electropolymerization to ensue without anodic etching of the seed layer.

The electrolytes consisted of 0.1 M pyrrole + 1% (m/m) sodium dodecyl sulfate or 0.5M pyrrole + 0.2M LiClO₄ in aqueous media. All solutions were made with nanopure water from a Milli-Q Academic purification system. Dodecyl sulfate (DS) was selected as a dopant for its size and structure which has been demonstrated to have a relatively low mobility⁶⁴ compared to smaller spherical dopants (i.e. chloride and perchlorate) and greater response to small polar molecules.⁶⁵ A three electrode configuration was used in a single cell with a Pt counter electrode under ambient condition. The electrolytes were purged with N₂ (99.999 %) for 30 minutes prior to electrodeposition. DS doped PPy nanowires were galvanostatically electrodeposited at 1 mA cm⁻² and ClO₄⁻ doped PPy nanowires were potentiostatically electrodeposited at 0.9 V (vs. Ag/AgCl). Electropolymerization of the nanowires was controlled using an EG&G Princeton Applied Research VMP-2 Galvanostat/Potentiostat. Deposition time was adjusted to control the length of the nanowires as described in previous work.²⁷ After suspending the PPy nanowires in water or isopropyl alcohol, they were drop-cast on prefabricated 5 micron gap gold microelectrodes containing peripherally positioned contact pads, which were electrically interfaced with copper tape and silver paint.^{26, 52, 66}

The maskless contacts were potentiostatically electrodeposited in a three electrode configuration by submerging the microelectrodes with loosely bound nanowires (i.e. working electrode) in an electrolyte and applying a constant deposition potential against Ag/AgCl reference electrode. Counter electrodes were nickel for nickel plating or

platinum coated titanium for gold and copper plating. Nickel sulfamate baths were used to embed DS-PPy nanowires and nickel sulfamate baths, gold sulfite baths, and copper sulfate baths were used for contacting perchlorate doped PPy ($\text{ClO}_4\text{-PPy}$) nanowires. Nickel was electrodeposited from $0.91\text{M Ni}(\text{SO}_3\text{NH}_2)_2 + 0.2\text{M NiCl}_2 + 0.4\text{M H}_3\text{BO}_3$ by varying the deposition potential from -0.7 to -1.1V . Gold was electrodeposited from 40mM NaAuSO_3 electrolytes purchased from Technic Inc., by applying a deposition potential of -0.5 or -0.7V . Copper was electrodeposited from 0.5M CuSO_4 and 0.5M NaSO_4 with an applied potential of -0.025V .

2.3 Results and Discussion

Maskless electrodeposition of nickel on the DS-PPy nanowires was studied to determine the effects of applied deposition potential and initial resistance on selectivity of the deposit, reduction of the nanowires and contact improvement. Selectivity is a measurement of electrodeposited material to discriminate between the desired deposition on the electrodes and non-preferential deposition on the nanowire, ideally depicted in Figure 1. The electrodeposited nickel displayed tunable selectivity for the PPy nanowire with the applied potential. At -0.7 V , the nanowire was coated with nickel particles while higher cathodic potentials were used to embed the nanowire ends in Ni with no observable deposition on the bridging portion of the nanowire. Particles size and density was greatest at low deposition potentials (i.e. -0.7 V), with $7.45\text{ particles}/\mu\text{m}^2$ and an average diameter of 204 nm to being not visible with SEM at -1.1 V for a constant charge density of $3.53\text{ C}/\text{cm}^2$ (Figure 2). This trend was facilitated by very low

deposition rates on the electrodes at lower cathodic potentials (e.g. $E = -0.7$ V) and hence longer deposition times, which permitted more nucleation sites and subsequent particle growth for kinetically limited deposition on the conducting polymer without closing the electrode gap. The selective metal deposition on electrodes, particularly in the case of Ni, is also a consequence of the nanowire reduction, which acts as a barrier preventing deposition on the PPy nanowire. Particle deposition on the nanowire is detrimental to its electrical properties as charge tunneling may occur between the PPy and Ni nanoparticles resulting in unstable electrical behavior when the particles consist of various sizes.⁶⁷ On the other hand, metallic nanoparticles can enhance sensitivity to some gas analytes through Schottky junctions and spill over effects.^{68, 69}

More notably, the initial resistance had a profound impact on the efficacy of the apparent contact improvement R/R_0 (R_0 and R are the resistances before and after electrodeposited contact, respectively) as the process was counterbalanced by reduction of the polymer. The reduction is dependent on the applied potential and is a strong function of the polymer redox state,⁷⁰ increasing with increased resistance.⁷¹ Nanowires in the $M\Omega$ range experienced a decrease in resistance down to hundreds of $k\Omega$, while nanowires of initially three hundred $k\Omega$ or less increased in resistance up to three fold for an applied potential of -0.96 V. This procedure was also shown to contact nanowires short of bridging the electrode gap with post-electrodeposition resistances in the low $M\Omega$ or high $k\Omega$ range. This is a consequence of isotropic growth for the electrodeposited metal which closes the electrode gap enabling contact of partially bridging nanowires. This behavior can be interpreted as a complex response to increased interfacial area

between the nanowire and the electrodeposited contacts with simultaneous reduction of the electrode gap and declination of the nanowire conductivity. The reduction of these nanowires occurs by ingress of cations during the cathodic electrodeposition of metal contact because of the relative immobility for the larger DS dopant.^{59, 64, 71, 72}

In the case of ClO_4^- -PPy nanowires, the level of reduction increased dramatically, typically an order of magnitude. The increased reduction can be rationalized by the mechanism of dedoping; an egress of the smaller spherical perchlorate anions. This increased reduction and higher resistance also inhibited metal deposition on the nanowire as the Ni was selectively deposited on the electrode surface wrapping around the conducting polymer nanowire even at -0.96 V. The electrodeposited gold contacts were less selective than nickel with particle formation on the nanowire and normalized resistance (R/R_0) changes of 0.67 ± 0.46 and 7.14 ± 1.52 at -0.5 and -0.7 V, respectively. Lastly the copper showed no preferential deposition, with complete coating of the nanowire and electrodes, shorting the nanowire device. Thus the choice of electrolyte served as another approach to tune this technique with different potential windows for electrodeposition. The lower applied cathodic potential of -0.5 V with the gold electrolyte also resulted in minimal nanowire reduction, high selectivity, and contact improvement. In the case of Ni, the lower deposition potentials resulted in an order of magnitude drop in current density, requiring much greater times for the same quantity of Ni deposition on the electrodes. This extended time period, during which the cathodic deposition potential was continually applied to the nanowire, created a deeply reduced state in the polymer resulting in the trend shown in Figure 2E. Thus, our method is able

to create mechanical joints and electrical contacts of conducting polymer nanowires to electrodes, but may be limited to conducting polymer and large band gap semiconducting nanowires since metallic and low band gap semiconductor nanowires could promote non-preferential deposition on the nanowire.⁶¹

The sensing performance of a single DS-PPy nanowire of pre- and post-electrodeposited contacts was investigated by exposing the nanowire to ammonia gas. Ammonia is a widespread compound of interest commonly found in industrial refrigeration systems and the production of fertilizers and explosives. Ammonia is also a component in vehicle emissions resulting from rich air-fuel conditions and catalytic converter malfunction contributing to the formation of fine particulate matter (PM_{2.5}), which could be mitigated or better controlled with a sensor feedback system.⁷³ Lastly, elevated concentrations of ammonia in exhaled breath, 50-100 ppb, can be used as a noninvasive diagnosis of renal disorders or ulcers. Adsorbed ammonia donates an electron to the PPy nanowire, reducing the backbone and the conductivity until the electron is transferred back to the donating ionic counterpart.⁷⁴ The sensing behavior of the nanowire with electrodeposited contacts (Figure 3) shows a drastic increase in sensitivity as well as an order of magnitude decrease in noise, from 0.1 MΩ to 0.01MΩ. The noise reduction can arise from the increased contact area, solid mechanical joints that prevent disturbances of electrical contact, and the reduction of charge traps. In disordered materials such as polypyrrole the noise can be related to the traps which concomitantly contribute to the conductivity in an intermittent fashion due to their spectrum of relaxation times.⁷⁵ The electrodeposited contact procedure is believed to

electrochemically reduce many of these charge traps which arise from branching and disordered chain termination. The sensitivity increase may also be attributed to a decrease in contact resistance and operation in a bulk limited regime or possibly to Ni ion inclusions.⁷⁶ Additionally, the change in the redox state of PPy or work function of Ni as opposed to the Au lithographically patterned electrodes may contribute to enhanced sensitivity. The combined effect is a significant improvement of sensing performance (lower detection limit, greater signal-to-noise ratio).

2.4 Conclusions

In summary, a facile technique to create good electrical and mechanical contacts for single conducting polymer nanowires has been described. Electrodeposition has been shown to provide maximum contact area by embedding nanowire ends to mitigate contact resistance from line contacts of as-assembled nanowires. The nucleation of metal particles on the PPy nanowire has been shown to be tunable by adjusting the deposition potential. This feature was further demonstrated with different electrolyte compositions. In the case of conducting polymers, a complex interplay between contact resistances and redox state of the nanowires were presented, where contact improvement reduces the overall resistance but reduction of PPy nanowires increases resistance. Preliminary gas sensing results have indicated significant noise reduction and improved sensitivity to ammonia for a DS doped PPy nanowire.

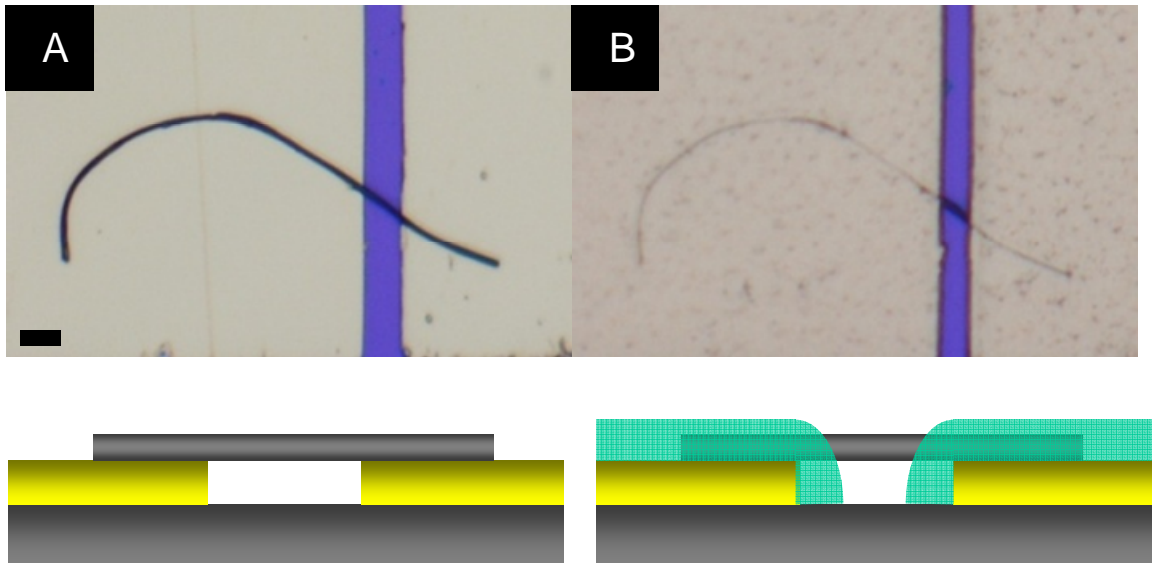


Figure 2.1: (Top): Optical images of a single PPy nanowire on gold electrodes before (left) and after (right) maskless electrodeposition of nickel: Scale bar represents $3\mu\text{m}$. (Bottom): (Left) Corresponding schematic of loosely bound nanowire crossing two gold microelectrodes. (Right) Selective maskless electrodeposition of metal (green) on electrodes to embed the nanowire for better electrical and mechanical contact.

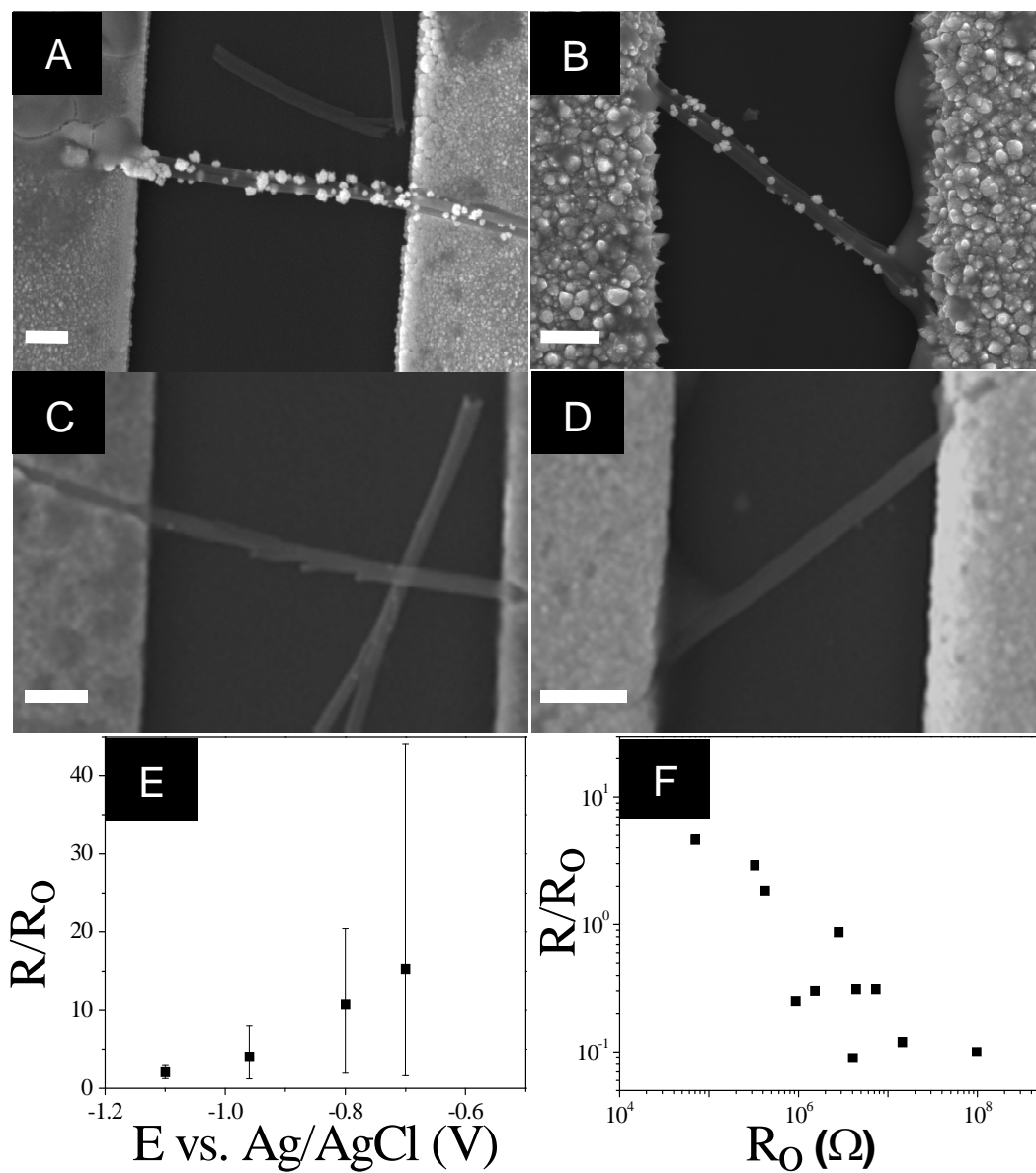


Figure 2.2: SEM micrographs of DS-PPy nanowires on electrodes after maskless nickel electrodeposition at (a) -0.7V, (b) -0.8V, (c) -0.96V, and (d) -1.1V at a constant charge density of $3.53\text{C}/\text{cm}^2$. (scale bars represents $1\mu\text{m}$). The R/R_0 ratio (e) as a function of applied deposition potentials and (f) initial resistance for contacts deposited at -0.96V.

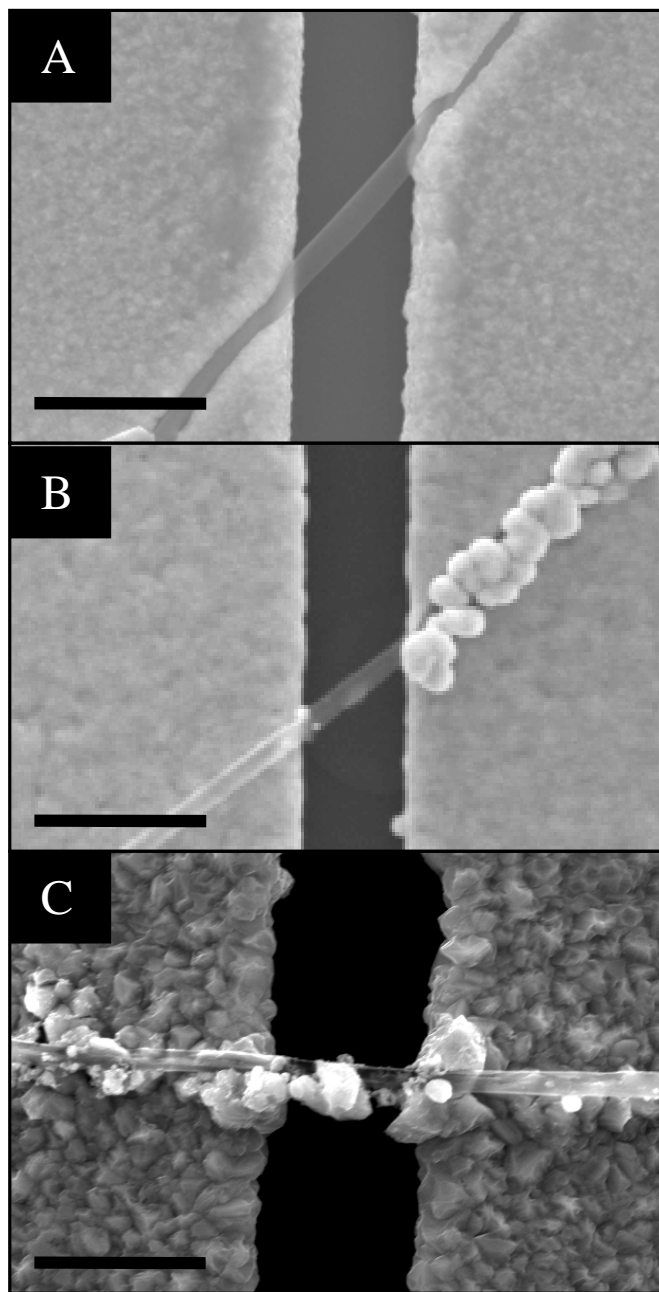


Figure 2.3: SEM micrographs of single polypyrrole nanowires after electrodeposition of (B) Ni, (C) Au, and (D) Cu at -0.96V , -0.5V , and -0.025V vs. Ag/AgCl, respectively. All scale bars represent $2\mu\text{m}$.

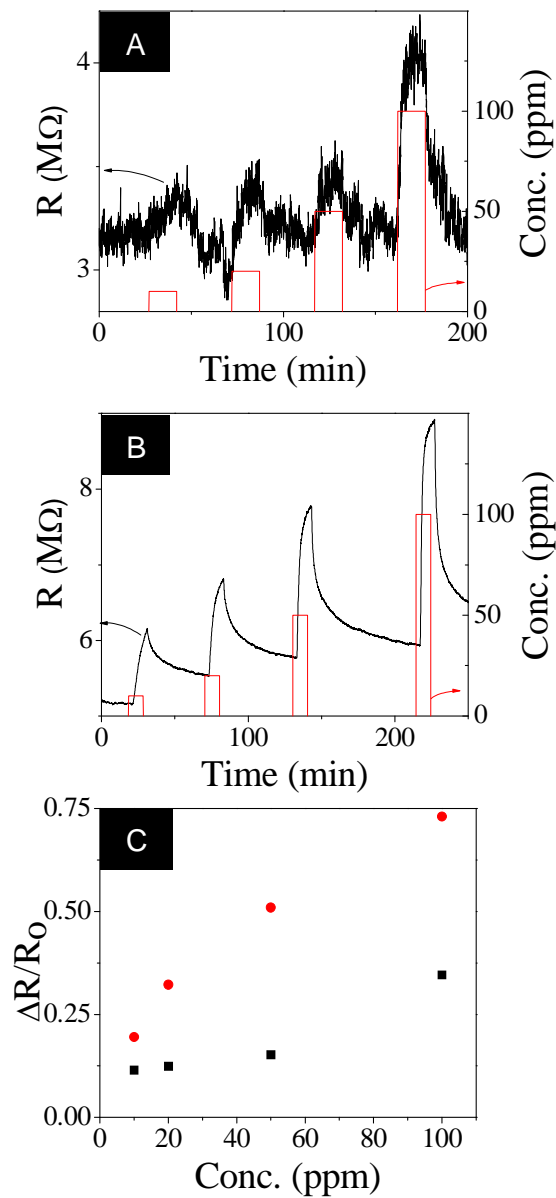


Figure 2.4: Sensor response of a loosely bound (a) and an embedded (b) single DS doped PPy nanowire as a function of different NH_3 concentrations. (c) The sensitivity of a loosely bound (■) and embedded nanowire (●).

Chapter 3: Tuning the Sensing Performance of Single PEDOT Nanowire Based Gas Sensors

Abstract

This chapter reports the synthesis and dopant dependent electrical and sensing characteristics of single poly(ethylenedioxythiophene) (PEDOT) nanowire devices. Dopant type and electrolyte solvent were selected to tune the electrical behavior by not only changing the conductivity but the conjugation length as well. These dopant dependent electrical studies of PEDOT nanowires were demonstrated by temperature dependent current-voltage measurements including temperature coefficient of resistance and reduced activation energy. Individual nanowire devices were also challenged with several volatile organic compounds, displaying substantially enhanced selectivity and sensitivity towards hydrophobic analytes. These features were attributed to both the extended conjugation lengths and deeply reduced level of the wires.

3.1 Introduction

One-dimensional (1D) conducting polymer (CP) nanostructures are actively studied materials for next generation solid state devices^{59, 72, 77-79} because of their unique combination of physical and mechanical properties arising from their conjugated backbone and inherent polymeric nature. Moreover, a host of synthesis techniques, including physical, chemical, and electrochemical, allow these materials to be fabricated

in just about any lab while also providing latitude for manufacturing purposes. Another critically important feature of CPs is that their properties can be tuned by dopant type and concentration.^{80, 81} During synthesis these ions have been found to directly affect the order of polymer chains, while post synthesis doping techniques, both chemically and electrochemically, have been used to tailor electrical behavior by cycling through their reduced and oxidized states with little or no substantial activity loss. These tunable electronic states have been shown by spectroscopy to be the results of changes in their absorption spectra that can be described as a modulation of the work function.⁷⁷

CP materials are particularly attractive for advanced sensing devices because of their room temperature operation, low power consumption and tunable conductivity. Their chemiresistive modality, or direct transduction mechanism, also lends utility to its miniaturization and portability with the least demanding requirements for supporting electronics. In this operating mode the increased surface area to volume ratio of 1D nanostructures has been demonstrated to improve sensitivity/response times due to greater/faster penetration of surface processes into the bulk of the nanowire.^{9, 10} In addition, nanowire constituents have been specifically identified as a means to reduce sample volume requirements and achieve higher density devices, leading to advanced sensing systems known as electronic noses that mimic olfactory functions in complex organism. In this context, an array of sensors is used to improved false negative/positive readout, selectivity, and sensitivity by creating unique recognition patterns or signatures for each analyte of interest. However, one criterion for creating these high performance devices is contrasting responses among individual sensing elements for each analyte,

which can be addressed by the veritable database of conducting polymer monomer/dopant combinations and blends.

However, the additional challenge at hand is the robust design of heterogeneous arrays of nanowires or fabrication of complimentary sensing elements adjacent to one another. This feat requires an in-situ bottom up approach, wherein individual elements are sequentially grown in place, or a post-synthesis assembly technique. While in-situ techniques usually require expensive, serial processes, such as electron-beam lithography or focused-ion beam, to pattern templates for nanowire growth, ex-situ growth can exploit high density hard templates with well defined pores to fabricate nanowires in massive parallelism. Although a variety of methods have been demonstrated for assembly of individual nanowires to prefabricated microelectrodes, additional steps are required for good electrical and mechanical joints to effectively probe true nanowire responses and eliminate unpredictable inter-nanowire and electrode-nanowire contact resistance.^{27, 29, 82} Unfortunately, the vast majority of single nanowire devices demonstrated are free standing assemblages with bottom line contacts on prefabricated electrodes, which is neither sufficient for electrical contact nor stable for long term monitoring.^{9, 10, 26, 29} Recently, we have demonstrated maskless electrodeposition as a versatile procedure for fabricating individual polypyrrole nanowire devices for detection of gaseous analytes and cancer antigens.^{83, 84}

In this work controllable integration of 1-D polymeric constructs with existing microelectronics was demonstrated by dielectrophoretic assembly coupled with a technique deemed maskless electrodeposition to improve contact and ensure solid

mechanic joints. This unique approach embeds the nanowire ends with the nanowire suspended across the two electrodes, permitting systematic investigation of solvent- and dopant-dependent electrical and gas sensing behavior. Single nanowire devices were electrically characterized by temperature dependent current-voltage (IV) measurements to elucidate charge transport mechanisms and relative order of the conducting polymer chains, which can be used to correlate structure to sensing properties for better design of sensing systems. The gas sensing performance was evaluated in a chemiresistive mode by analyzing changes in resistance upon exposure to humidity and various volatile organic compound (VOC) vapors. As a case study this chapter focuses on polyethylenedioxythiophene (PEDOT) nanowires with two different dopants, polystyrenesulfonate (PSS) and ClO_4^- , and reports the influence of solvent on device performance. PEDOT is a well studied member of the polythiophene family due its 3,4-ethylenedioxy substituent that has demonstrated good stability,⁸⁵⁻⁸⁷ relatively low oxidation potentials,⁸⁷⁻⁸⁹ and enhanced redox properties.⁸⁶

3.2 Experimental Details

Two different working electrodes were prepared for these experiments, Au thin films for CVs and nanoporous templates for nanowire electrodeposition. The Au thin films were prepared on Si wafers with a 100nm thick SiO_2 layer. The wafers were first cleaned with acetone, isopropyl alcohol, and water then dried with high purity N_2 (99.998%). A Temescal BJD-1800 electron-beam evaporator was used deposit a 20 nm Cr adhesion layer followed by a 180 nm Au thin film. These wafers were cut into 2.25

cm² chips and electrically contacted with double sided copper tape to serve as a leads. The copper tape and chip edges were masked with red mylar tape to produce a 1 cm² working area and reduce edge effects. PEDOT nanowires were synthesized using template directed electrodeposition with commercially available Whatman templates (200nm nominal pore size). The templates were first sputtered with approximately 500 nm of Au using an EMS K550X. For electrodeposition to proceed solely within the pores of the template the seed layer must be electrically contacted and all electrically conductive materials, with the exception of accessibility to the seed layer through the pores, must be masked with a dielectric. This was achieved with a sandwich structure of the template between silicone gaskets and Teflon plates held together by Teflon bolts. A small hole was drilled through one Teflon plate and gasket for electrolyte accessibility to the seed layer via the nanoporous template. The Teflon and silicone materials were selected for nonsolubility in aqueous and nonaqueous solvents.

Three different PEDOT baths were prepared, PEDOT/PSS (PSS) in H₂O/CH₃CN 1/1 v/v (PP1), PEDOT/ClO₄⁻ in H₂O/CH₃CN 1/1 v/v (PC1), and PEDOT/ClO₄⁻ in CH₃CN (PC2). The PEDOT baths were prepared by first adding the dopant salt to the corresponding solvent. Lithium perchlorate was added directly to acetonitrile and/or water and M_w 70,000 NaPSS was added first to water followed by addition of acetonitrile for a final concentrations of 0.1M LiClO₄ (PC1, PC2) and 0.05M NaPSS (PP1), respectively. The solutions were purge with 99.998% pure N₂ for 30 min to remove dissolved O₂, preventing nonpreferential oxidation of the monomer. The monomer was subsequently added to a concentration of 0.05M EDOT for both electrolytes.

All electrochemical experiments were carried out with an EG&G Princeton Applied Research VMP2 Potentiostat/Galvanostat. The cyclic voltammograms were conducted with a three electrode configuration with a Au thin film working electrode, Pt coated Ti strip counter electrode, and SCE reference at a scan rate of 10 mV/s from OCP-100mV to 2V (vs. SCE) and back again to the OCP, cycled 5 times. Electrodeposition of the PEDOT nanowires was preceded by 1 μm of Au electrodeposition, to prevent nanowire branching and serve as more uniform nanoelectrodes as opposed to the sputtered seed layer. A commercially available bath 25 ES RTU (Technic Inc.) was used to electrodeposit Au at -1 mA/cm^2 for 16 min with a two electrode setup, including the nanoporous working electrode and Pt counter electrode. PEDOT nanowire electrodeposition was conducted in a 100mL cell with the same three electrode setup described above substituting the nanoporous alumina template for the working electrode. Different potentials were investigated with the length of the nanowires controlled by time and charge.

Following electrodeposition the seed layer was polished with 240 grit SiC polishing paper. The template was then thoroughly rinsed with distilled water and placed in 1mL of 30% v/v H_3PO_4 for 8 hours to remove the template. The nanowires were washed by centrifugation at 9.3 g's for 2 min (Eppendorf Centrifuge 5415D), removal of the supernatant, addition of 1mL of distilled water, and resuspension of the nanowires by sonication (VWR Model 50D, power setting 3). The process is repeated three times and the final nanowire suspension is diluted 20 times v/v before proceeding to alignment.

Nanowire alignment was performed with micropatterned substrates fabricated in-house by standard lift off lithography. The Si wafers, with a thicknesses of 500-550 microns and a thermally deposited oxide layer 100 nm (Ultrasil Corporation), were first spin coated with an adhesion promoter (ShinEtsuMicroSi Microelectronic Material, Primer P20) at 1000 rpm for 2 second followed by 4000 rpm. for 30 seconds. A positive photoresist layer (Rohm and HAAS Electronic Material, S1813) was spin coated under the same conditions as the adhesion promoter and directly transferred to a hot plate at 110°C for 5 min. After soft baking, the PR was exposed, via a patterned mask, to an ultraviolet lamp at a wavelength of 365nm and intensity of 5mW/cm² for 7 second. The pattern was subsequently developed in an aqueous developer (Rohm and HAAS Electronic Material, 351) solution diluted at a ratio of 1 to 5 for 50 second, rinsing with nanopure water, and drying with 99.998% N₂. Wafers were then loaded into a Tamescal BJD-1800 e-beam evaporator to deposit 20 nm of Cr and 180 nm of Au in succession at a rate of 1.0 Å/s and 3.0 Å/s, respectively. Lift-off was executed by immersion in electronic grade acetone overnight. The prepared wafers were finally cut into 1 cm² chips with a ruler and diamond tip pen. Each chip consisted of sixteen electrode pairs with 50 µm edges separated by a 3µm gap.

Dielectrophoretic assembly was conducted on a Wentworth Labs MP-901 probe station. Nanowires were aligned one electrode pair at a time by first applying 1 V peak to peak at 5 MHz (Keithley 3390 Waveform Generator) to the electrode pair and dispensing 0.5 µl of the nanowire suspension. The nanowires were aligned for 10 seconds followed expelling the nanowire suspension with N₂, and inspecting the chip with a Hirox KH3000

VD for a count of bridging nanowires. Due to variation in the nanowire concentration the suspension was diluted by trial and error to yield approximately 0-5 nanowires per alignment trial. The excess nanowires were removed mechanically with the tip of a Au wire (25 μm diameter) attached to Quater R.&D. XYZ 300ML micropositioner.

Electrical behavior was probed by scanning the potential from -1V to 1V with a Kiethley 246 measurement unit and custom Labview program. Cold temperature measurements were performed by coupling this system to a Janis Research Co. CCS-350SH cryogenic system with a Lakeshore 331 temperature controller. The nanowire responses to various VOCs were tested with a custom built gas sensing system of Alicat MC-500SCCM-D mass flow controllers (MFC) operated by Labview. Dry air passed through one MFC to an analyte bubbler of acetone, methanol, ethanol, water, or methyl ethyl ketone (MEK), which combined with another line of dry air before introduction to the sensor. The sum of the two lines was held constant during sensing trials at 500 standard cubic centimeters per minute (scm) and the ratio of the two was used to control the exposure concentration. The nanowire micrographs were obtained by Phillips XL30-FEG scanning electron microscope (SEM). Transmission electron microscope images were carried out on Cu grids with C films using an FEI Phillips CM300.

3.3 Results and Discussion

3.3.1 Nanowire Synthesis and Device Fabrication

Three PEDOT electropolymerization baths were studied, two previously reported baths, PSS and ClO_4^- , and one intermediate bath to provide insight on the differences between the other two baths. For PP1, a well characterized material for electrochromic displays and hole injectors, a mixed solvent of 1:1 $\text{H}_2\text{O}/\text{CH}_3\text{CN}$ was used to accommodate the hydrophilicity of the PSS polyelectrolyte while CH_3CN increased the solubility of the EDOT monomer. A CH_3CN solution with a LiClO_4 electrolyte was employed for its ability to produce highly conductive films and for the contrasting nature of its small, mobile ClO_4^- dopant. Due to the insolubility of PSS in CH_3CN , the intermediate bath investigated was a 1:1 $\text{H}_2\text{O}/\text{CH}_3\text{CN}$ solute with a LiClO_4 electrolyte, which to the best of our knowledge has not been previously investigated. These PEDOT electrolytes were characterized by cyclic voltammetry with a Au thin film from open circuit potential (OCP) – 100mV to 1.8 V vs. a nonaqueous reference electrode (NAE) with and without the EDOT monomer (Figure 3.1). The scanning rate was 10mV/s and an upper limit of 1.8 V was set to prevent Au delamination from the Si substrate. The cyclic voltammograms (CVs) indicate only a slight increase in oxidative current with each wave insinuating minor overoxidation of the CP at higher potentials, consistent with PEDOT reports,⁹⁰ but indicate much higher current density for both PC1 and PC2 electrolytes relative to the PSS polyelectrolyte. Additionally, the low background current density in the monomer-free acetonitrile bath is typical for strong aprotic solvents, in

contrast to the strong background current densities at higher operating potentials produced by oxygen evolution in the water-acetonitrile mixtures.

PEDOT nanowires were synthesized by template directed electrodeposition into a nanoporous alumina host. The unique advantage of this approach is precise control over the nanowire dimensions by the template in the radial direction and by electrodeposition time/charge for the length. The process follows the schematic of Figure 1.1. First, Au seed layer is sputtered followed by electrodeposition of a sacrificial 1 μm Au segment within the pores to reduce branching, which due to its nobility allows electropolymerization to ensue without anodic etching. Following nanowire deposition, the seed layer is mechanically polished and the template is selectively removed in phosphoric acid. The nanowires are subsequently washed and finally suspended in water.

The growth curves were conducted for deposition in the nanoporous template as a function of potential corroborating solvent- and dopant-dependence polarization curves. Unlike most electrodeposited metals and inorganic semiconductors, conducting polymer can exhibit variation in porosity and structure within the template, factors that affect growth rate. In particular, PEDOT nanowires have been shown to form tubular structures or fronts due to the tip effect and fast reaction rates at higher potentials.⁹¹ The tip effect is a result of incomplete seed layer coverage, creating an annular base within each pore and an electric field distribution conducive to tube formation. This mechanism was eliminated by electrodeposition of a flat Au plug prior to electropolymerization. Consequently, for a fixed charge density, increased lengths at more positive potentials can be attributed to extended tube fronts from faster reaction rates (Figure 3.2). The

nearly stagnant potential dependent growth rates for PP1 nanowires suggest little tube formation or change in density at higher applied potentials, while the PEDOT/ ClO_4^- nanowire growth rates indicate a considerable change in the structure, corresponding to longer tube formation as described to Lee's work.⁹¹ These results are consistent with thin film potential dependent growth mechanism shifts from a two-dimensional layer by layer growth for compact amorphous thin films at low potential to a more crystalline, porous deposit with predominately three-dimensional growth at high potentials.^{92, 93} The error bars represent nonuniformity in length of the embedded PEDOT nanowire array and are most extensive for PC1 nanowires. Low electropolymerization potentials, 1V vs. SCE, were selected to eliminate variation introduced from tubular structures and nonuniform electrodeposition.

Furthermore, the water-acetonitrile mixtures were either less efficient or more dense in contrast to the acetonitrile bath, producing length to current density ratios of $\sim 4.5 \mu\text{m}/(\text{C}/\text{cm}^2)$ at nearly all potentials for both the PP1 and PC1 nanowires. The variation in porosity was qualitatively verified by TEM, as shown in Figure 3.3. The PP1 nanowires exhibited smooth surfaces and uniform density even at higher magnification. On the other hand, PC1 nanowires began to display sparse grain-like transparencies that indicate a less compact structure and possible evidence for crystalline domains. These features were intensified in PC2 nanowires, more prominent in number and dispersity with well defined borders, reminiscent of inorganic grains. Although differences in the porosity appear to contribute to the growth rate to current density ratio the high

nucleophilicity of water is also a likely factor, which produces a competitive reaction that is known to terminate chain growth in thiophene electropolymerization.

The first step in device fabrication is nanowire alignment to prefabricated electrodes by dielectrophoretic assembly. Using an aqueous suspension with a concentration of roughly 10^6 nanowire/ μL a volume of $0.5\mu\text{L}$ was manually dispensed over the electrode gap. The nanowires were allowed 10 seconds to align resulting in several nanowires bridging the electrode gap. The actual number of nanowires for each electrode pair varied slightly, 0-10, and required trial and error optimization by dilution to achieve greater precision of aligned nanowires. The intended single nanowire devices were attained through successive removal of excess nanowires by mechanical means. Although this is not a manufacturable step, the authors would like to indicate potential optimization for controlled assembly of single nanowires by electrode design and through the use of Au terminating nanowire segments and a serial capacitor described by Mallouk.²⁹

The as assembled nanowire devices displayed poor behavior in terms of electrical and sensing performance due to variation in the contact and were subsequently subjected to maskless electrodeposition, described previously⁸⁴. This procedure selectively electrodeposits material on the electrodes to embed the nanowire ends. The process is based on the existence of a potential window for greater cathodic current density on the metallic electrodes as compared to the conducting polymer nanowire and the redox activity of the nanowire, where the cathodic current for the nanowire is primarily ionic in nature with no observable electrodeposition, which for PEDOT nanowires was found to

be -0.5 V vs. SCE. This method has been demonstrated with fully aligned nanowires with large overlap between the nanowire ends and electrodes as well as to electrically contact partially bridging nanowires with one nanowire end suspended in the electrode gap. Due to the isotropic growth of the electrodeposited Au on the microelectrodes, the electrode gaps decreased ~23% from 3 μm to ~2.3 μm . (Figure 3.4 A-B)

3.3.2 Electrical and Sensing Properties

Individual nanowire devices were characterized visually and electrically. Optical images and SEM micrographs reveal the nanowire ends to be partially enveloped by the electrodeposited Au. They also indicate the nanowire to be suspended slightly above the substrate for maximum access to its entire surface. The I-V response is the simplest technique to gauge the electrical properties of a device. In the case of PEDOT and other conducting polymers, the I-V can indicate ohmic contact by a linear response or nonohmic contact with nonlinear response. While the response for PEDOT/PSS nanowires indicate symmetric, nearly linear responses at room temperature, PEDOT/ ClO_4^- nanowires experienced slight rectification. The room temperature conductivities of these wires were 1.30, 30.85, and 3.54 Scm^{-1} for the PP1, PC1, and PC2 nanowires, respectively.

Although both PC1 and PC2 displayed slightly higher conductivities than PP1 nanowires, their conductivities are still an order of magnitude short of reported conductivities for similar ClO_4^- doped nanowires.³⁰ The difference can be attributed to a deeply reduced state for the PC1 and PC2 nanowires, which were measured as high as 150 Scm^{-1} and 318 Scm^{-1} , respectively, prior to maskless electrodeposition. The higher

conductivities for PC1 and PC2 nanowires are anticipated as its small size allows it to be intercalated between chains in very high concentrations and has been demonstrated to exhibit a relative increase crystallinity. The doubling of the conductivity from PC1 to PC2 can be correlated back to its difference in solvent, where the large quantity of water in the PC1 bath terminates chain growth leading to lower conjugation length and hence conductivities.⁹⁴⁻⁹⁶ Additionally, the extent of reduction appears greater for PC2 and may be attributed to a more porous structure, a characteristic feature of longer conjugation lengths and greater crystallinity derived from acetonitrile based baths.⁹² The PSS dopant has very distinct behavior by comparison, providing a long polyanionic backbone for fragmented PEDOT polymerization while comprising and directing major components of its physical structure. Thus electrodeposited PEDOT/PSS usually attains lower conductivities due to its dense, amorphous structure and inert PSS matrix but is more stable with high resistance to electrochemical reduction and ionic mobility.^{88, 97} These features along with the high mobility of ClO_4^- suggest that both PC1 and PC2 experienced drastic reduction during maskless electrodeposition.

The temperature dependent IV responses were measured from 300 to 10 K in 10 K increments. The temperature coefficient of resistance (TCR), defined as dR/R_0dT , is a measure of the electron transport properties and is used to distinguish between metallic and semiconductor behavior. The negative TCR values are characteristic of semiconductor materials, with stronger semiconductor behavior displaying more negative TCR values, exhibited by the PEDOT/ ClO_4^- nanowire from the CH_3CN solution. A larger activation energy, described by $R/R_0 = \exp(E_A/2kT)$, also indicates stronger carrier

concentration temperature dependence and substantiates TCR data with values of 304, 120, and 42meV for PC2, PC1, and PP1 nanowires, respectively.⁹⁸ The magnitude of the activation energies supports a deeply reduced state for PC2 nanowires, probably as a consequence of the reducing current during maskless electrodeposition. However, the disorder for conducting polymers is better characterized by the log plot of the reduced activation energy (Figure 3.6), which supports greater order for PC1 with a slope of 1.27, followed closely by the PC2 nanowire with a slope of 1.21 and finally the W slope for PEDOT/PSS was 0.41. These results suggest greater disorder in PSS doped nanowire with a slight solvent effect on disorder, and a drastic reduction in the oxidation level of the nanowire from the single solvent ClO_4^- bath.

Nanowire devices from each bath described in the aforementioned experimental section were challenged with water vapor and several VOC's including, acetone, methanol, ethanol, water, and methyl ethyl ketone. The analyte concentrations for real time exposures are reported in percent of their saturation vapor pressures, which are 166.8, 77.5, 301.4, 118.2, and 31.2 parts per thousand for methanol, ethanol, acetone, MEK, and water, respectively. The exposure profiles for acetone, water, methanol, and ethanol are shown in Figure 3.7.

The profiles for the PP1 single nanowire device, Figure 3.7 (A,D,G,J), reveal response times, defined as the time required to reach 90% of ΔR_{max} , to each analyte and several concentrations with a mean of 2.9 min, but as long as 9min and short as 30sec for some analytes, with quicker responses at higher concentrations, which may be an indication of considerable lag time and limitation with the bubbler setup. Examination of

individual analytes reveals slower responses and incomplete recovery for VOC's relative to humidity. This behavior implies slower penetration into the nanowire bulk and higher desorption energies for the VOC's. Conversely, the opposite trend for water and its slight decrease in the baseline upon recovery suggest a polarity enhanced response including a weak, counteracting chain alignment mechanism, most likely due to hydration of the hydrophilic PSS backbone upon which smaller PEDOT chains are bound.¹⁵ The conformational change is probably minimized in PP1 due to the large size (M_w 70,000) and relative immobility of the PSS dopant. Further evidence for polarity preference is distinguishable in Figure 3.8B, where normalized responses to ppm concentrations display the following sensitivity order; water > ethanol > methanol > acetone. The linear sensitivities are also quantified in the histogram of Figure 3.9. The correlation coefficient values, r , for linear and power law sensitivity fittings suggest similar fittings for each plot with better correlation to the power law model for water but slightly lower r values for methanol, ethanol, and acetone. These responses are in agreement with a swelling sensing mechanism, whereby adsorbates increase the hopping distance for carriers, increasing the resistance for all analytes.

The intermediate PC1 bath produced the most undesirable characteristics of these single nanowire devices. At low concentration no measureable response was observed for either methanol or water, and as the concentrations increase irreversible responses and inconsistent directional changes in the resistance denoted the unreliability of PC1 nanowires. Exposure to acetone and ethanol provided more stable responses and decent sensitivities with positive $\Delta R/R_0$ values of 40.9 and 11.3, respectively, at 50% saturated

vapor. However, after the final exposure to acetone the baseline dropped by over 60% of its original value. Similar behavior was observed for MEK saturated vapor concentrations of 30% and greater with a drastic decrease in the baseline during exposure and recovery, evident from Figure 3.8D. This baseline dip may corroborate DC dependent measurements and literature reports for shorter conjugation lengths due to nucleophilic side reactions with water that terminate chain propagation. Despite the well documented insolubility of PEDOT in normal processing organic solvents, reduced oligomers have demonstrated solubility in aprotic organic solvents.⁹⁹⁻¹⁰¹ Therefore, high concentration of aprotic solvents such as acetone and MEK may conceivably saturate PEDOT oligomers and induce conformation alignment with the DC potential, increasing crystallinity and permanently reducing the resistance. However, the aforementioned traits are all undesirable for gas sensors and indicate no practical conductimetric sensor application for PC1 nanowires. Thus, despite the similar trend in analyte sensitivities and enhanced responses to water by comparison to PP1, the weaker correlation coefficients of PC1, 0.866, 0.972, 0.823, and 0.987 for water, methanol, ethanol, and water, respectively, indicate instability or poor sensor performance as a result of mixed sensing mechanisms for both water and ethanol.

On the other hand, the PC2 nanowire exhibited promising sensor qualities distinct from that of either PP1 or PC1. As shown in Figure 3.7 C, F, I, L, PC2 yields greater sensitivities to acetone, ethanol, and methanol, with slightly reduced sensitivity to water, with respect to PP1 and PC1. Moreover, the normalized response to acetone reaches values in excess of 3000%. While the baseline is relatively stable for acetone and

ethanol, drift due to incomplete recovery is evident for methanol and water, which is nearly opposite in behavior to PP1. The log-log plot of the normalized responses, Figure 3.8F, yields linear trends for all analytes in the range of 10-50% saturation. Lower saturations, regardless of the concentration in ppm, deviate from these fittings, probably due to smaller diffusion constants, significant lag of the bubbler, requiring much longer exposure times, and/or incomplete surface coverage with less aggregate analyte-analyte interactions which would shift adsorbate charge transfer dependency from electronegativity to ionization potential producing markedly different behavior and consequently dynamic ranges.^{102, 103}

In Figure 3.8E the nanowire sensitivity can be clearly distinguished for three separate groups, water, ethanol-methanol, and lastly acetone-MEK. This figure alone suggests some sort of polarity or hydrophobicity induced sensitivity, however when these responses are analyzed with respect to the corresponding ppm concentrations of the analytes, Figure 3.7F, the picture changes. Analytes with higher vapor pressures present decreasing sensitivity in the following order for MEK, acetone, and ethanol. Nonetheless, at lower concentrations (i.e. <20,000ppm) overlap between analytes is difficult to differentiate. Construction of a log-log plot that discards values for saturations <10% for reasons described above, displays a power law relationship, $\Delta R/R_0 = Ac^\beta$, with values of 0.81, 0.63, 1.41, 2.73, and 2.78 for water, methanol, ethanol, acetone, and MEK, respectively. Therefore, with the exception of methanol, PC2 displays a general increase in sensitivity, as defined by the slope of the normalized responses vs. the analyte concentration, with decreasing hydrophilicity or polarity of the

analyte. A linear chart of the sensitivities produced the same trend in analyte sensitivity as shown in Figure 3.9 with comparable correlation coefficients to log plot fittings, bearing slightly better fittings for water than methanol. The actual lower detection limits are subject to further investigation due to long bubbler retention times at low partial pressures.

The power law dependence suggests work function modulation of the CP nanowire as described by Janata and Josowicz. In this model the Mulliken electronegativity, $\chi = 0.5(E_a - I_p)$, of the analyte is described by the electron affinity, E_a , and ionization potential, I_p , accordingly. The difference in the work function of the polymer, ϕ , and the analyte electronegativity, χ , indicates the extent of the response.¹⁰⁴ Thus for $\phi = \chi$ little or no response would be produced, for $\phi < \chi$ the analyte behaves as an electron acceptor, and for $\phi > \chi$ as an electron donor. Therefore, in a deeply reduced PEDOT nanowire such as PC2 contacted by maskless electrodeposition the work function difference, $\Delta WF = \phi - \chi$, would be much greater^{95, 105} than that of the as synthesized PEDOT/ ClO_4^- and would result in a greater electron donicity of the analyte and increase in resistance. For different concentrations of an analyte the change in work function of the polymer, $\Delta\phi$, has been described by its Fermi level dependence on the partial pressure, $E_f \propto -\ln P_i^\delta$, where δ is the partial charge transfer.¹⁰⁴ Additionally, it is reasonable to assume the porosity of PC2 allows any charge transfer to directly translate into a change in the carrier concentration for bulk conductivity, $\sigma = \mu n$, where σ is the conductivity, μ is the mobility of the charge carrier, and n is the carrier concentration. Therefore, according to Fermi-Dirac statistics it is logical that, $E_f \propto \ln(n) \propto \ln(\sigma) \propto -\ln$

P_i^δ . The result is the observed power law dependence of the resistance, $\Delta R/R_0 = AP_i^\delta$, as described by the fractional charge transfer, $\delta = \xi(\phi - \chi)$, where ξ is a proportionality constant that can be determined from a plot of ΔWF vs. ϕ for a set analyte concentration. Although χ is difficult to determine due to difficulties in measuring the electron affinity, the ionization potentials are more reliable and much larger in magnitude permitting approximate values in lieu of χ .¹⁰² The I_p values follow the same trend as polarity with 12.62, 10.85, 10.43, 9.703, and 9.52eV for water, methanol, ethanol, acetone, and MEK, respectively, which correspond to χ of approximately 6.31, 5.43, 5.22, 4.85, and 4.75eV. Thus for similar ξ , as demonstrated by Blackwood et al,¹⁰² the partial charge transfer, δ , should increase with decreasing I_p , as was shown earlier for all analytes except methanol.

3.4 Conclusions

Electropolymerization of PEDOT nanowires was systematically investigated for different dopants, PSS and ClO_4^- , different solvents and operating potentials. Growth curves were used to establish different rates, uniformity, and structure. Single nanowires devices were fabricated by A.C. dielectrophoretic alignment and maskless electrodeposition. The electrical properties were measured to indirectly correlate sensing properties to oxidation level, work function, conjugation length, and dopant effect. PEDOT/PSS was found to be very resistant to electrochemical reduction due to the stability and immobility of the PSS polyelectrolyte. The sensing responses of PEDOT/PSS nanowires were attributed to swelling. While this trait bodes well for

reliability, it also occludes tunable sensing performance. Conversely, PC1 nanowires synthesized from a water/acetonitrile mixture with LiClO_4 , as opposed to PSS, produced very unstable nanowire sensor devices probably due to decreased conjugation lengths caused by nucleophilic side reactions of the solvent that terminate chain propagation. The high mobility of the perchlorate anion led to drastically reduced PC2 nanowires with greater order as determined by its increased reduced activation energy slope. These nanowires produce superior responses to more electronegative analytes, with some values in excess of 3000%, and demonstrated a power law dependence on the analyte concentration at high partial pressures, which was postulated to derive from its work function modulation.

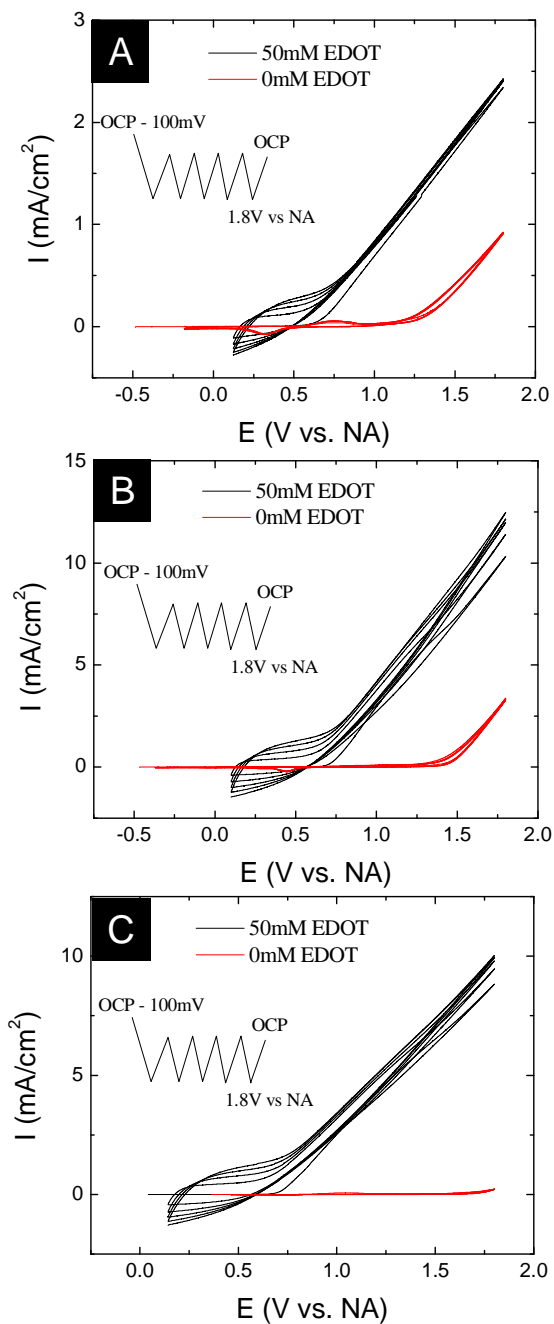


Figure 3.1: Cyclic voltammograms of each PEDOT bath (A) PP1, (B) PC1, and (C) PC2 with and without the EDOT monomer.

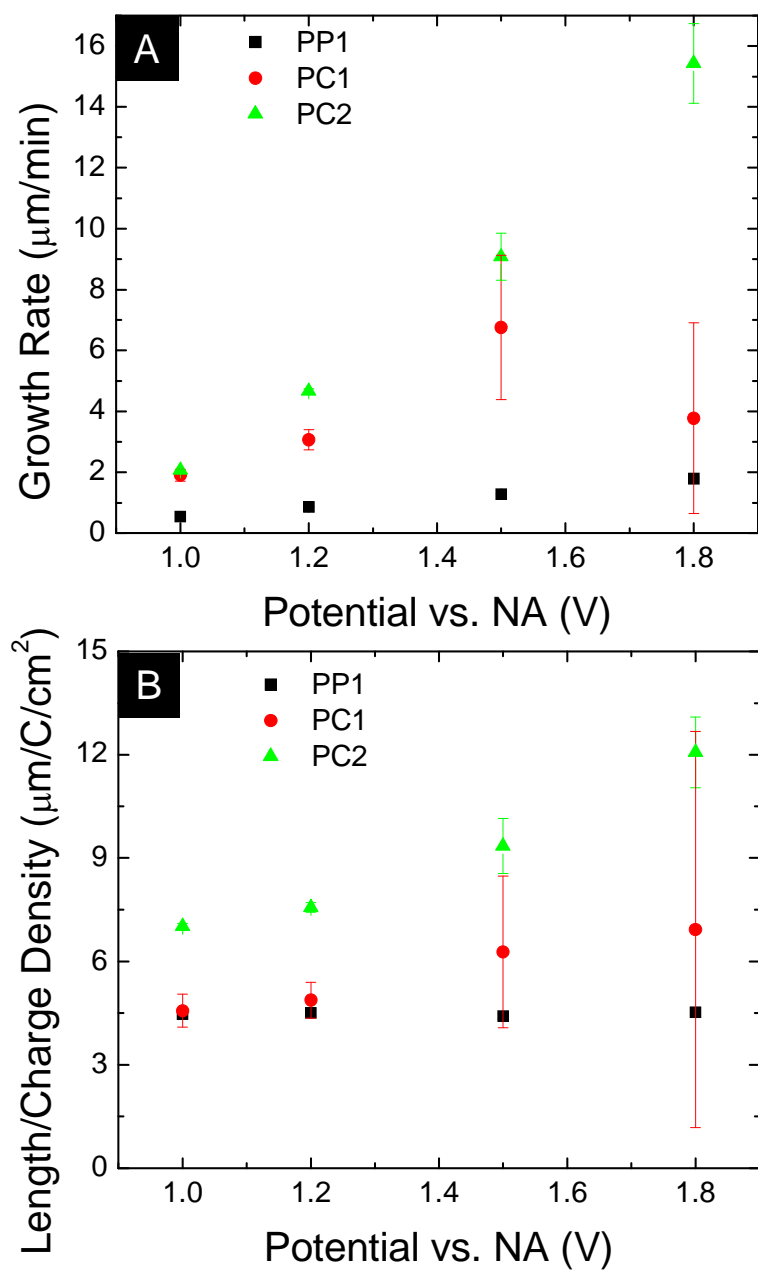


Figure 3.2: (A) Plot of the growth rate as a function of applied potential vs. a nonaqueous reference electrode for each PEDOT bath. (B) The nanowire length (μm) per unit charge density is plotted as a function of potential vs. a nonaqueous reference electrode for each bath. In both graphs the error bars represent standard deviations based on seven samples.

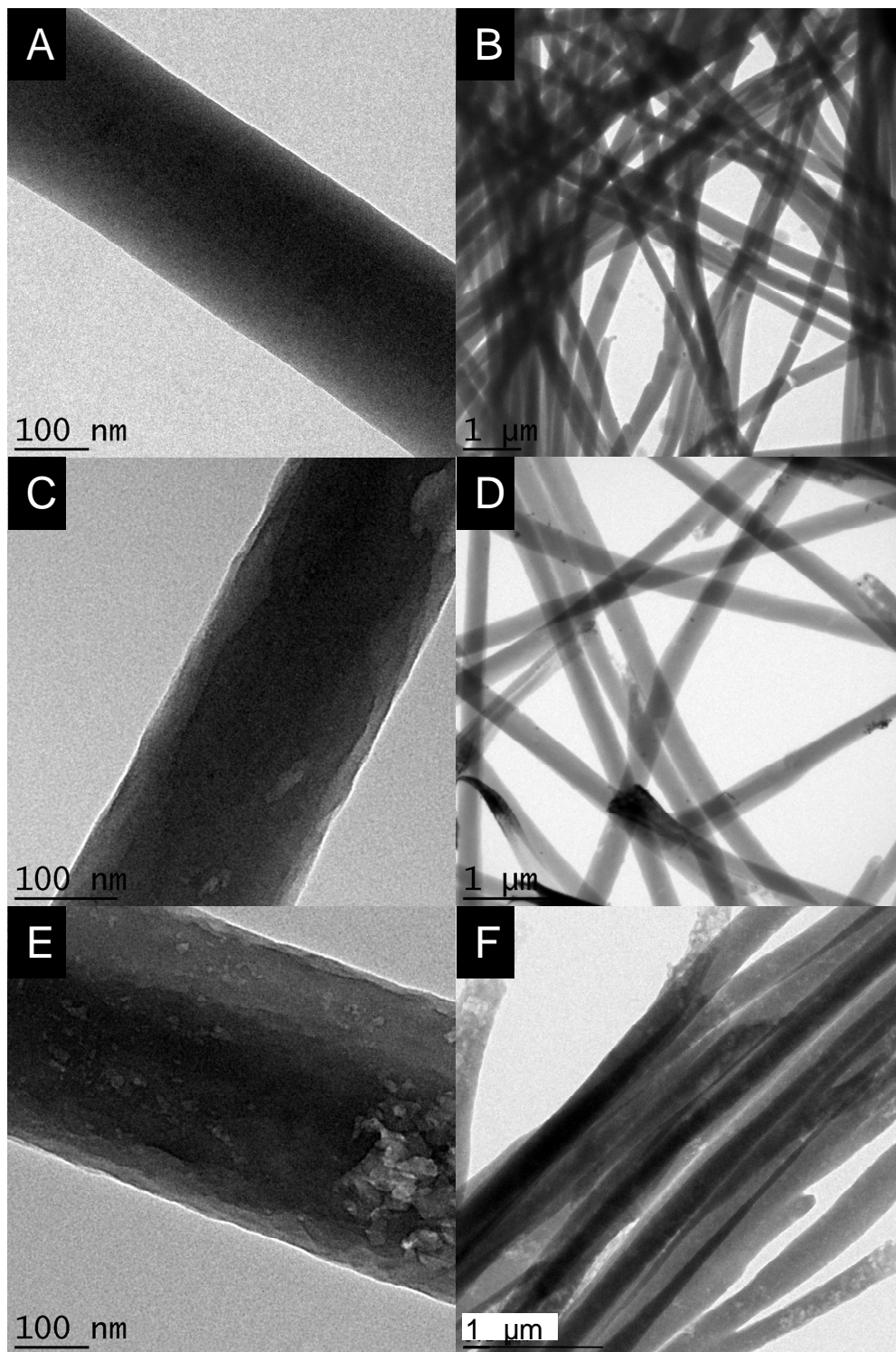


Figure 3.3: TEM images of (A, B) PP1, (C, D) PC1, and (E, F) PC2 nanowires

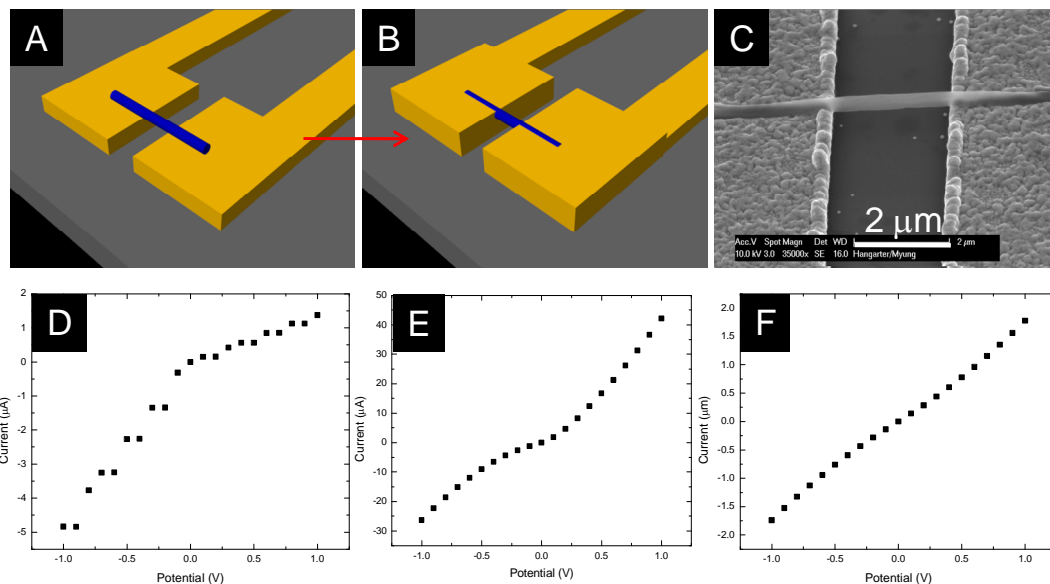


Figure 3.4: (A-B) Schematic of maskless electrodeposition, starting with a single aligned nanowire with selective electrodeposition of Au on the electrodes with no deposition on the PEDOT nanowire. (C) The resulting single nanowire structure was imaged with SEM. The current-voltage response for (A) PC2, (B) PC1, and (C) PP1 are shown before and after maskless electrodeposition.

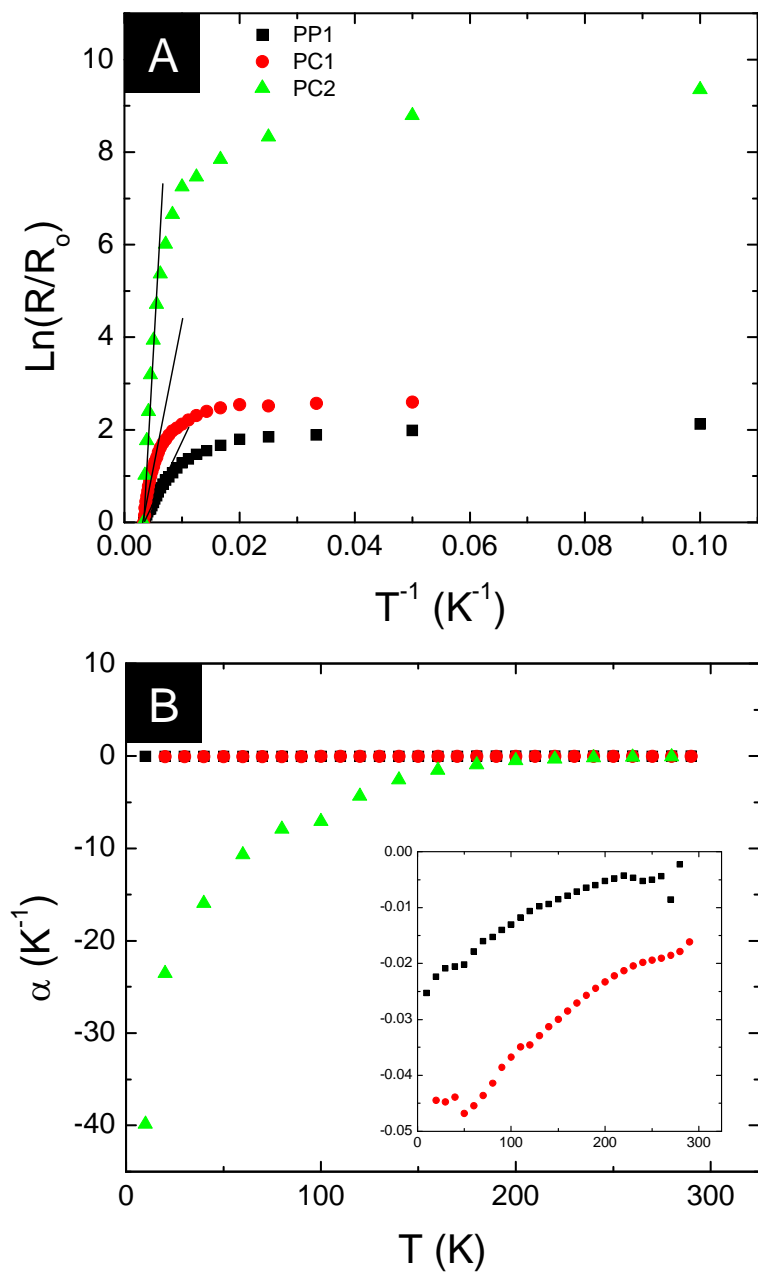


Figure 3.5: (A) Normalized Arrhenius plot of single PEDOT nanowires for each of the three baths. The slopes of the lines indicate activation energies of 42, 120, and 304meV for PEDOT/PSS, PEDOT/ ClO_4^- (mixed bath) and PEDOT/ ClO_4^- (MeCN) nanowires, respectively (B) Temperature coefficient of resistance for the same nanowires as function of temperature. The inset magnifies low TCR values.

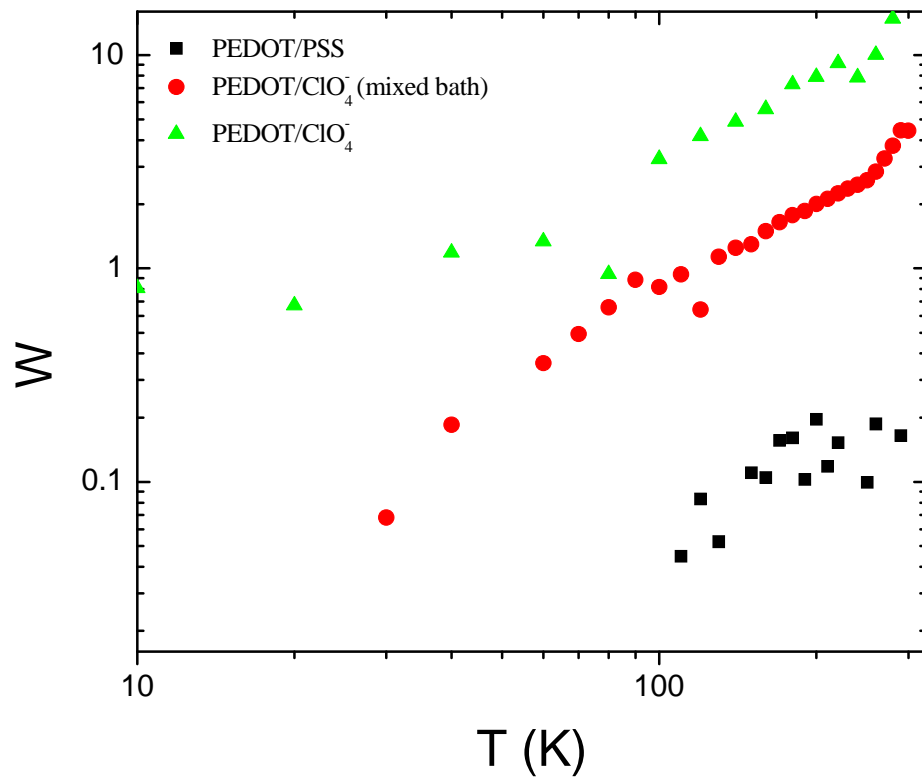


Figure 3.6: Reduced activation energy for single nanowires from the three different electropolymerization baths.

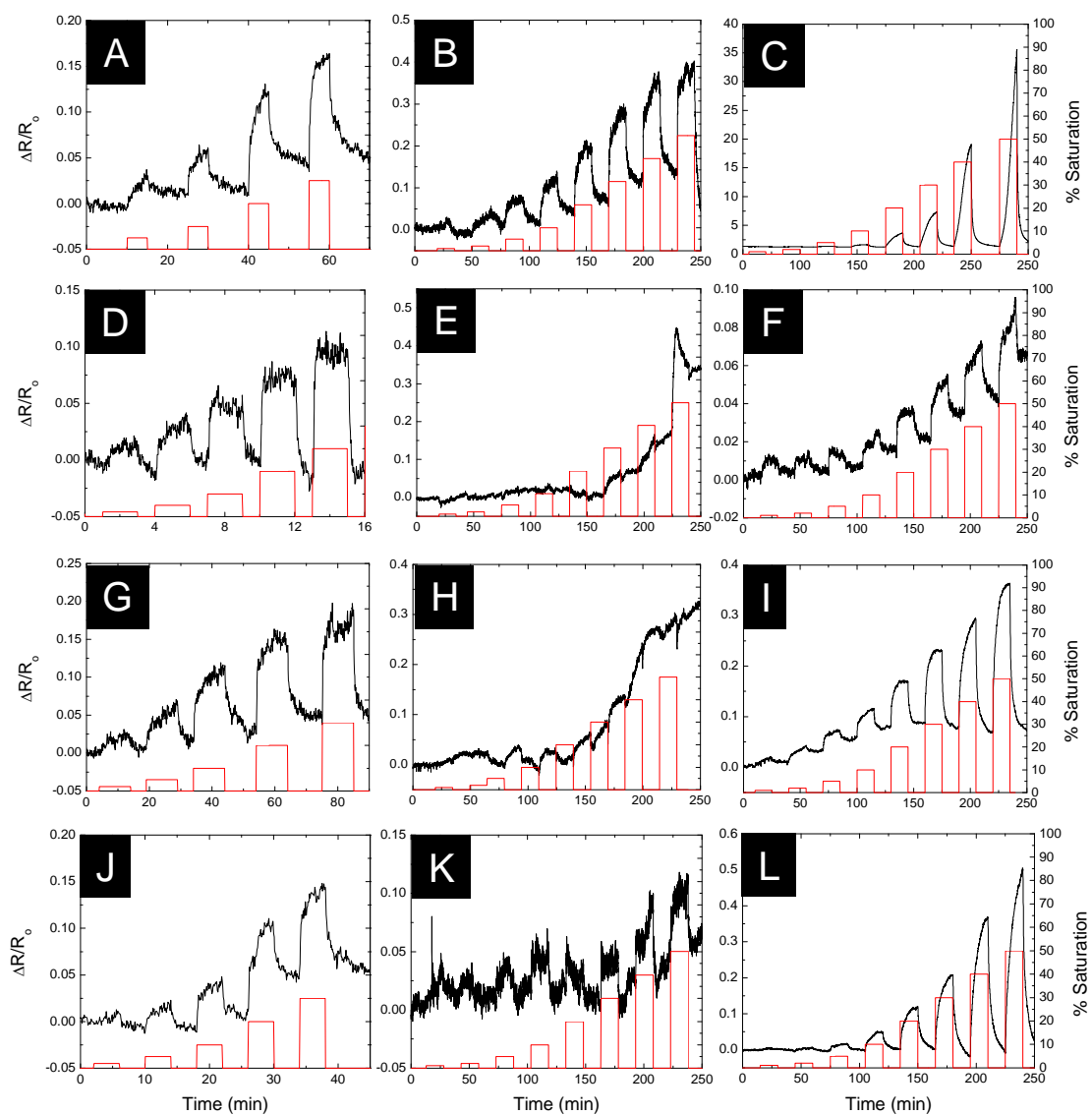


Figure 3.7: Normalized sensing profiles for single (A, D, G, J) PP1 (B, E, H, K) PC1 and (C, F, I, L) PC2 nanowires in response to (A-C) acetone, (D-F) water, (G-I) methanol, and (J-L) ethanol. The analyte exposures are reported in percent of their saturation concentrations with their scale shown only to the right of (C, F, I, L).

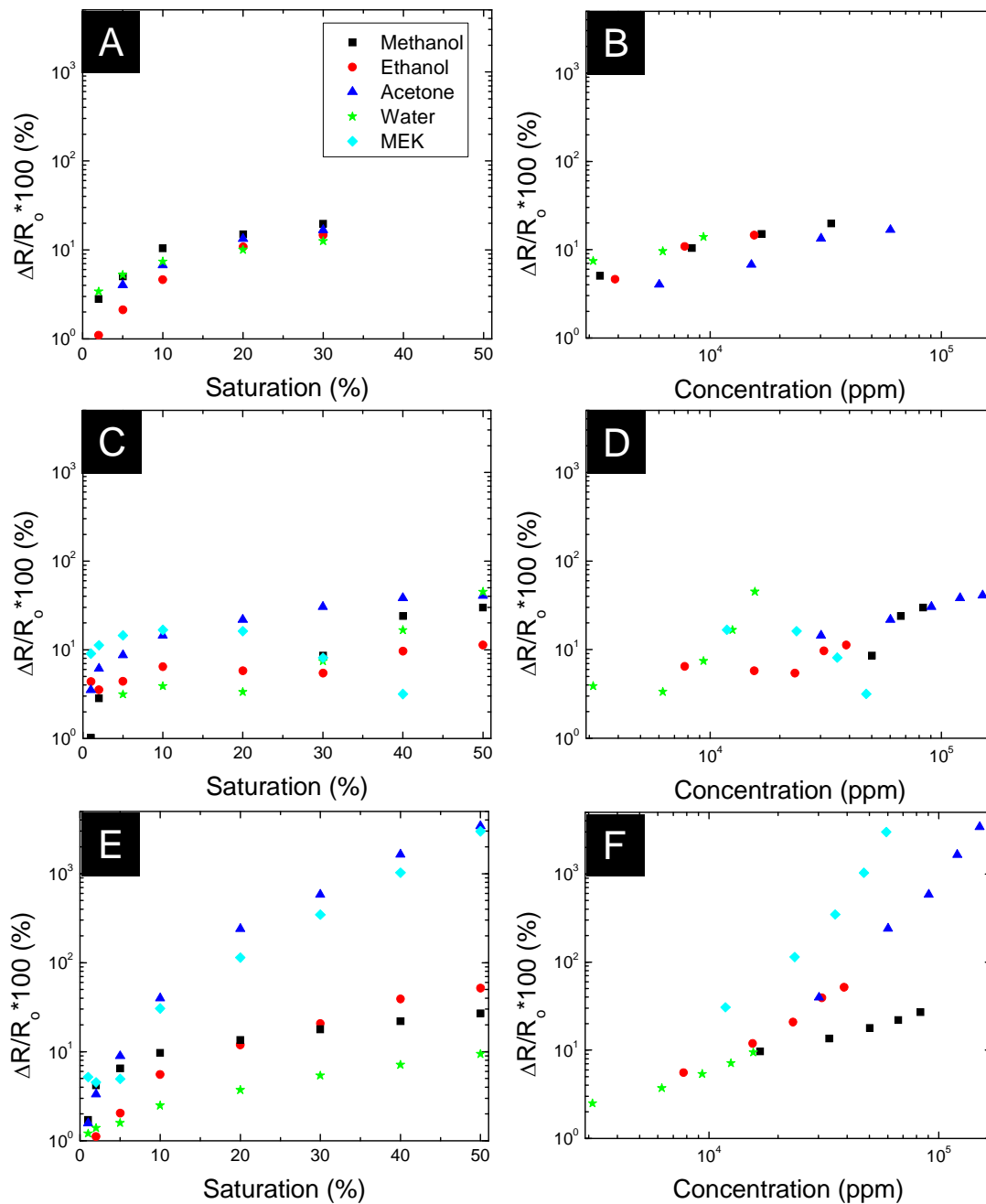


Figure 3.8: Normalized responses for single (A, B) PP1, (C, D) PC1 and (E, F) PC2 nanowires to several VOCs and humidity at room temperature and a flow rate of 500 sccm. The $\Delta R/R_0$ scale is kept the same for visual comparison and the key for all plots is shown in (A).

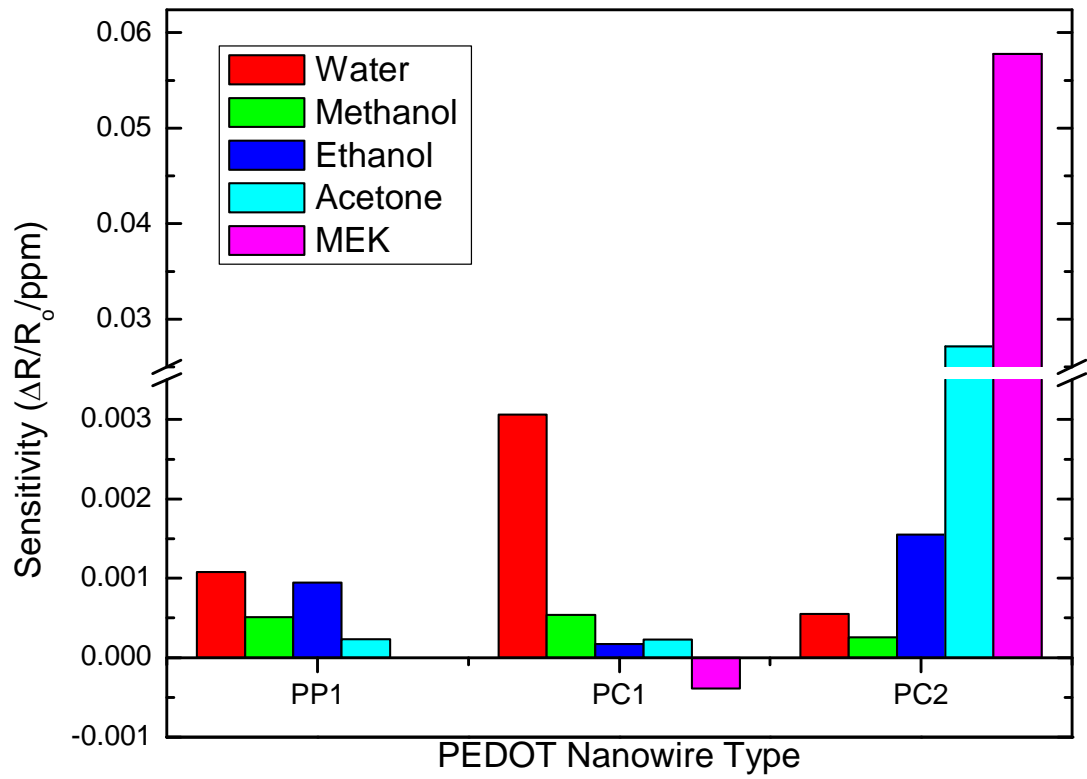


Figure 3.9: Histogram of nanowire sensitivity to each analyte. The break was inserted to illustrate the relative sensitivity of most nanowire-analyte interactions in comparison to that of PC2 to both acetone and MEK.

Chapter 4: Anomalous Magnetoresistance of Ferromagnetic Nanotubes

Abstract

Single ferromagnetic nanotubes were fabricated utilizing a single PEDOT nanowire device as a positive template for nanotube formation. The core/shell PEDOT/Ni structures were characterized electrically by temperature coefficient of resistance (TCR), which correlated well with Ni nanowire TCR values indicating the electrical conduction is dominated by the Ni nanotube. The magnetoresistance (MR) behavior of these Ni nanotube devices was studied as a function of angle, temperature and composition. The angle dependent MR responses revealed atypical behavior at low fields, deviating from expected anisotropic magnetoresistance (AMR) of Ni nanowires with negative MR values for both longitudinal and transverse measurements. Temperature dependent measurements displayed high field behavior consistent with AMR and negative transverse MR values down to 10K, the magnitude of which increased with decreasing temperature. Studies of a Ni₃₀Fe₇₀ displayed the opposite behavior with positive MR values for both longitudinal and transverse directions. The angle, temperature, and composition dependent anomalous MR responses were shown to correlate well with magnetostriction behavior suggesting magnetostriction induced magnetoresistance.

4.1 Introduction

Ferromagnetic materials have formed the basis of phenomena such as anisotropic magnetoresistance (AMR), giant magnetoresistance (GMR), and spin torque diode effect for industrially important technologies such as magnetic sensors, hard drives, read/write heads, and magnetic random access memory (MRAM).¹⁰⁶ At the basis of many of these devices is magnetoresistance (MR), or the variation of electrical resistance in response to an applied magnetic field or magnetic state of the material. The assortment of MRs include AMR, GMR, organic magnetoresistance (OMR), colossal magnetoresistance (CMR), ballistic magnetoresistance (BMR), and tunneling magnetoresistance (TMR). One of the first successful exploitations of these properties was the use of permalloy in read/write head for hard drives. The AMR, a bulk property MR trait, of $\text{Ni}_{80}\text{Fe}_{20}$ was thought to be ideal for its large response to small fields (~5%), low magnetostriction, high permeability, and high corrosion resistance. However as hard drive bit density increased, the scalability of AMR quickly became an issue, with increased noise and lower sensitivity for smaller devices. Later the advent of GMR, an electron spin based quantum mechanical MR effect, paved the way for much larger responses with the use ferromagnetic/nonmagnetic lamellar structures in the nm regime.^{41, 107, 108} Furthermore, because GMR is an interfacial property, it is highly scalable and remains one of the most rapidly commercialized technologies of the 20th century.

Today, the phenomenon that originally emerged as GMR has developed into an entire field of spin-based electronics or spintronics, the study of spin manipulation in solid state devices. Like electron charge, the ability to control spin injection, transport

and detection will have a profound impact on logic, communications, and memory devices with the potential for non-volatile memory and reprogrammable logic.¹⁰⁹ Moreover, these devices are radiation-hard with comparable switching speeds and potentially lower power requirements than traditional charge-based electronics¹¹⁰.

Spin valves are the fundamental structures of spintronics, consisting of a current-perpendicular-to-plane (CPP) trilayer of ferromagnetic/nonmagnetic/ferromagnetic (FM/NM/FM) material. These devices rely on a quantum mechanical phenomenon designated giant magnetoresistance (GMR), which is an interfacial response to differences in spin polarization manifested as a substantial change in resistance. The importance of which was demonstrated by the 2007 Nobel Prize in Physics to the Frenchman Albert Fert and the German Peter Grünberg for their independent discovery of GMR in 1988. The first ferromagnetic layer injects spin into the NM layer, which decouples the two FM layers, and is detected by the second FM layer. When the magnetic orientation of both FM layers is parallel the device exhibits low resistance and when the two layers are antiparallel, a high resistance is observed due to the difference in availability of spin states.

Since GMR opened up a whole new field dedicated to the study of electronic spin, research efforts have been unequivocally partial to superlattices and sandwich nanostructures, with only a handful of reports on geometric induced spin control. These studies typically investigated lateral ring structures that demonstrated promise for nonvolatile memory due to their two stable counter/clockwise magnetization orientations.^{45, 46} Novel geometries such as nanotubes and other complex structures are

important as they may provide a means to wall thickness tunable spin transport or to enhance less sensitive spin dependent phenomena by coupling them with more responsive MR technologies. Although unique ferromagnetic one-dimensional nanostructures, including nanotubes, could be synthesized using template directed methods, contact is a continuing challenge due to the native oxide layers that form so quickly on these high surface area iron-group nanostructures. Additionally, their inherent fragility exacerbates attempts to characterize individual nanotubes.

In this chapter, a novel in-situ approach to synthesizing individual ferromagnetic nanotubes is reported that reduces internal oxidation and provides excellent electrical contact. This approach utilizes individually aligned PEDOT nanowires and a variant of maskless electrodeposition to fabricate nonmagnetic/ferromagnetic core/shell lateral nanostructures and study their magneto-transport properties. The resulting nanostructure has been characterized by temperature coefficient of resistance (TCR) to verify charge transport occurs predominately through the ferromagnetic shell. Temperature, angle and composition effects on the MR were investigated by fabrication of ferromagnetic Ni and Ni₃₀Fe₇₀ nanotubes. The MR profiles of several nanotubes with different wall thicknesses were studied for Ni. Finally, the magneto-transport characteristics of Ni/PEDOT coaxial nanowires in response to progressive chemical etching was performed to help elucidate the origin of the unusual nanotube MR behavior. Comprehensive analysis of these results provide strong evidence for magnetostriction induced magnetoresistance of these ferromagnetic nanotubes.

4.2 Experimental Details

Polyethylenedioxythiophene (PEDOT) nanowires were synthesized using template directed electrodeposition, described in previous chapters with anodic alumina oxide Whatman Anodisc 13. Gold seed layers were sputtered onto one side of the templates with an EMS KX550 tabletop sputter coater. The PEDOT nanowires were electropolymerized from an aqueous bath with 50mM of the monomer, ethylenedioxythiophene, and 100mM of the dopants, LiClO₄ and sodium dodecyl sulfate. The dopants, ClO₄⁻ and dodecyl sulfate (DS), were selected for their high conductivity and resistance to electrochemical reduction, respectively. The nanowires were potentiostatically deposited in a three electrode configuration with a Pt counter electrode and standard calomel reference electrode (SCE). Embedded nanowires were removed by polishing the seed layer and etching the template in 30% (v/v) H₃PO₄.

Single nanowire devices were fabricated by nanowire alignment to prefabricated microelectrodes with 3μm gaps followed by nonselective electroplating of a ferromagnetic material. Different electrode shapes and materials have also been investigated to discount their possible influence in these measurements. AC dielectrophoretic alignment conditions were optimized for alignment of electrodeposited PEDOT nanowires to both Au and Ni electrodes. Nanowires were suspended in water for alignment to Au electrodes with a peak to peak potential of 1V and a frequency of 5MHz. Ni electrodes required PEDOT nanowire to be suspended in isopropyl alcohol to prevent electrode dissolution and a peak to peak potential of 0.5V and 5MHz. Microelectrodes with aligned nanowires were contacted with Ag paint and Cu tape to ensure electrical

contact. Nanowire assemblages were subsequently electroplated with either Ni or Ni₃₀Fe₇₀. The Ni bath consisted of 1.5 M Ni(SO₃NH₂)₂ + 0.2 M NiCl₂ + 0.4 M H₃BO₃. By implementing a high potential, -1.1 V (vs. SCE) for short time periods (<60 sec), PEDOT nanowires were effectively coated using a standard Ni counter electrode. The Ni₃₀Fe₇₀ nanotubes employed an electrolyte of 0.2M NiCl₂ + 60mM FeCl₂ + 50mM L-ascorbic acid + 7.5mM saccharin + 0.7M NaCl + 0.4M H₃BO₃, and an applied current density of -5mA/cm² against a Pt counter electrode for 4 minutes in a two electrode configuration. The L-ascorbic acid was added to prevent Fe⁺² oxidation, saccharin was added as a stress reliever, and H₃BO₃ was added as a buffer.

The magneto-transport properties of individual nanotubes were measured using a physical property measurement system by Quantum Design at temperatures from 10 to 300 K. TCR data was extracted from temperature dependent MR measurements. The applied external magnetic field was scanned in the range ±100kOe in both the longitudinal and the transverse directions and 15° increments relative to the PEDOT nanowire axis. The voltage across the PEDOT/Ni and PEDOT/Ni₃₀Fe₇₀ coaxial nanowires was measured with a fixed applied current of 100μA. MR measurements of progressively etched nanotubes were performed with a Digital Systems Measurement vibrating sample magnetometer model 1660, a 236 Kiethley measurement unit, and custom Labview program at room temperature in the ambient. Nanotube micrographs were obtained with a Phillips XL30-FEG scanning electron microscope (SEM).

4.3 Results and Discussion

Scanning electron microscopy (SEM) images confirm the PEDOT nanowires were bridging the electrodes without contact with the underlying Si substrate, allowing for a complete ferromagnetic tube spanning from one electrode to the other (Figure 4.1). In Figure 4.1 (A-C) are Ni nanotubes and (D) is a Ni₃₀Fe₇₀ nanotube. Variations in the contact of the nanowire and the proximity of the nanowire to the substrate lead to slight tube attenuation and distortion of the ideal circular cross-section in some samples, respectively, but in general the nanotube structure is fairly consistent from sample to sample. Additionally these wires reveal fairly solid contacts that interface a considerable portion of the nanotube cross section. These images also reveal the outer diameter of the nanotubes to be roughly 500nm, 600nm, 800nm and 550nm for Figure 4.1 (A), (B), (C), and (D), respectively. These diameters along with their measured resistances, 25Ω, 15Ω, and 6Ω, suggest an increasing nanotube wall thickness from sample (A) to (C), assuming a constant PEDOT nanowire width.

Low temperature measurements were conducted to verify the governing charge transport mechanism in these core/shell structures. The TCR values, described in section 3.3.2., are positive indicating charge transport predominately through the ferromagnetic nanotubes correlating strongly with those of Ni nanowires (Figure 4.2). The TCR values of the nanotube with decreasing size also fit the trend of decreasing TCR value for decreasing nanowire size. These results are expected as the resistivity of the PEDOT is several orders of magnitude greater than Ni. While the conductivity of the nanotube may

contribute to the charge transport of the structure, it is anticipated to be miniscule by comparison to the metallic nanotube.

Figure 4.3 shows the MR profiles of the Ni nanotube in Figure 4.1(A) measured at 10K, 100K, 200K, and 300K, with the corresponding MR ratios, defined as $(\Delta R/R)_{\text{long}} = [R_{\text{long}}(H) - R_{\text{long}}(H_{\text{sat}})]/R_{\text{long}}(H_{\text{sat}})$ and $(\Delta R/R)_{\text{tran}} = [R_{\text{tran}}(H) - R_{\text{tran}}(H_{\text{sat}})]/R_{\text{tran}}(H_{\text{sat}})$, shown in Figure 4.4. At all temperatures, longitudinal MRs (MR_{long}) show anisotropic magnetoresistance (AMR) behavior with a maximum MR ratio of 1.7 % at 200 K, which is identical to previously reported Ni nanowire properties.¹¹¹ For the transverse direction each Ni nanotube displays negative MR (MR_{tran}) values for all temperatures. This is in stark contrast to typical AMR measurements for both thin films and nanowires, which display a positive MR in the transverse direction, also depicted in Figure 4.4. Despite the increase in the high temperature MR_{tran} with decreasing size of nanowire and monotonic decrease with respect to temperature, Ni nanotubes display a very weak increase in high temperature MR_{tran} with decreasing resistance and a general increase in MR_{tran} with decreasing temperature. Similarly, Ni nanotubes also display near opposite behavior of their nanowire counterparts with an increase in MR_{long} with decreasing size as opposed to the reciprocal trend displayed for Ni nanowires. However, the most resistive nanotube did display similarity with the MR_{long} properties of the 200nm nanowire with an analogous trend and nearby values, peaking around 200K with increased suppression for decreasing temperatures. Conversely, the larger, more conductive nanotubes, 15 Ω and 6 Ω , displayed MR_{long} enhancement at low temperatures.

These effects might be attributed to domain wall formation of the Ni tubular geometry, which has an onion magnetization in the transverse direction at high fields and at very low fields approaches longitudinal magnetization due to the aspect ratio (3.1-6.3) induced magnetization.¹¹² This behavior would likely increase resistance at stronger fields due to domain wall formation perpendicular to the cylindrical axis but is not likely since such behavior is not apparent for nanowire samples. Alternatively, these effects may be attributed magnetostriction induced responses, where the soft polymer core permits expansion and contraction similar to a hollow ferromagnetic tube. The positive transverse saturation magnetostriction (MS), $\sim 20 \times 10^{-6} \Delta l/l$, for Ni indicates the nanotube length increased with increasing field strength, and accordingly the cross section will decrease as Ni has a negligible volume magnetostriction, $-0.06 \times 10^{-6} \Delta v/v$.¹¹³ The decreased cross section would cause an increase in resistance with stronger fields and therefore supports the observed negative MR_{tran} in the Ni nanotubes. The room temperature field dependent magnetostriction for Ni also appears to saturate after ~ 2000 Oe, similar to the nanotube MR profiles. Additionally, saturation magnetostriction increases in magnitude, nearly threefold, with decreasing temperature, as demonstrated by doubling of MR_{tran} in some nanotube samples.¹¹³ Finally, experimental results for magnetostriction hysteresis, as shown in Figure 4.5 inset, agree with the reported hysteresis and low field minimum for polycrystalline Ni.¹¹⁴

Further validation of magnetostriction induced magnetoresistance was verified by studying $Ni_{30}Fe_{70}$ nanotubes. Unexpectedly, the MR for $Ni_{30}Fe_{70}$ in all directions shows a positive response or decrease in resistance and maximum MR in the transverse

direction (Figure 4.6b). This is in agreement with the large volume magnetostriction constant for $\text{Ni}_{30}\text{Fe}_{70}$, $> 35 * 10^{-6} \Delta v/v$, which is over two orders of magnitude greater than the volume magnetostriction for Ni. This leads to an overall decrease in resistance regardless of the orientation due to the increase in diameter of the nanotube. The stronger response in the transverse direction can be attributed to the accumulated magnetostriction and AMR effects, which are in the same direction for transverse measurements and opposing one another for longitudinal MRs. The higher MS saturation field also explains the more obtuse MR profiles.

Finally, real time profiles of the device resistance during chemical etching enabled progressive analysis of the MR response as the nanotube cross-section was diminished, the results of which are depicted in Figure 4.6. The MR data reveals a transition from the anomalous tube response to behavior characteristic of a nanowire of decreasing diameter. In addition, the transverse MR increased and the longitudinal MR decreased as the nanotube was etched further, similar to the trend observed for smaller Ni nanowires by Rheem et al.¹¹¹ This appears to be due to pit formation during chemical etching, reducing cross-sectional changes due to magnetostriction.

4.4 Conclusions

Ferromagnetic nanotubes were fabricated by non-selective electrodeposition on individually assembled PEDOT nanowire devices. The TCR values of PEDOT/Ni core/shell structures match well with literature values for Ni nanowires, indicating charge

transport was dominated by the Ni nanotube. The MR responses of the Ni nanotubes demonstrated atypical behavior, with a transverse response opposite in direction from reported AMR values for Ni nanowires and thin films. The anomalous trends were described well by MS values and trends. Although relatively weak by GMR standards, these results provide a means to tailor the angle dependent MR responses from individual nanostructures, which may be enhanced by choice of material or coupling with collateral technologies. Further validation of MS induced MR was demonstrated by Ni₃₀Fe₇₀ nanotubes, whose large volume MS produced a decrease in resistance for both the transverse and longitudinal directions. Finally, progressive etching profiles revealed a diminished MS effect.

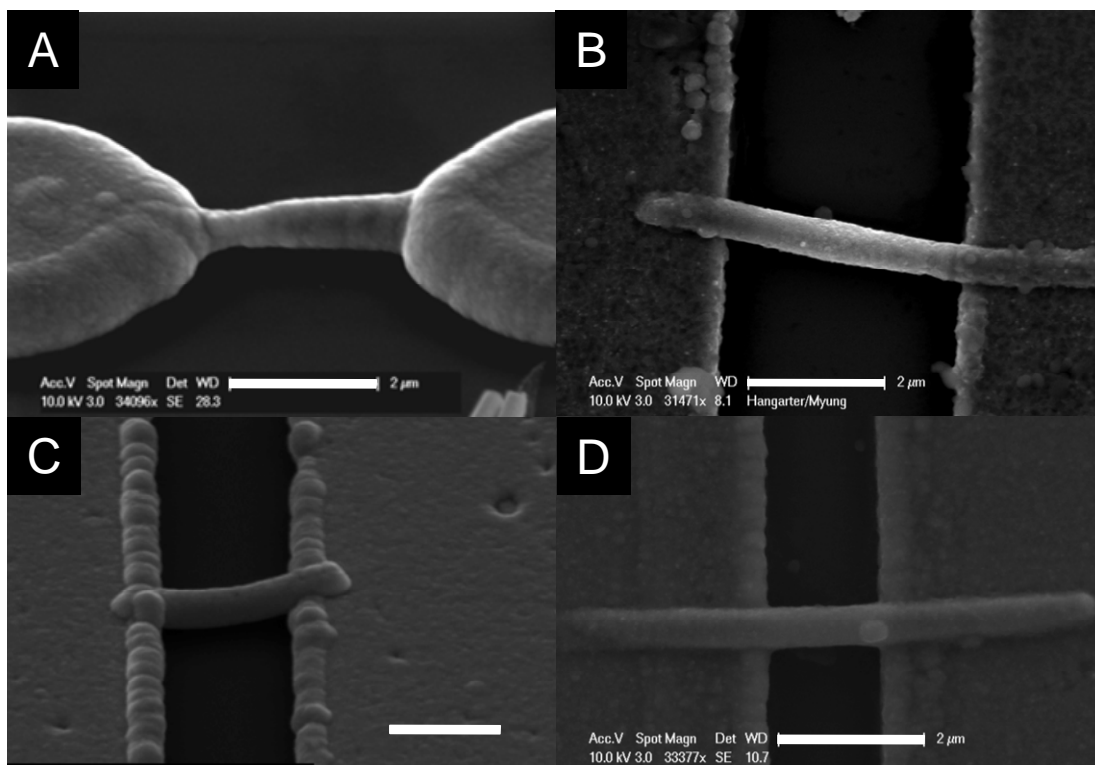


Figure 4.1: SEM images of Ni nanotubes with room temperature resistances of (A) 25Ω , (B) 15Ω , and (C) 7Ω . (D) A $\text{Ni}_{30}\text{Fe}_{70}$ nanowire with a room temperature resistance of 29Ω . All scale bars represent $2\mu\text{m}$.

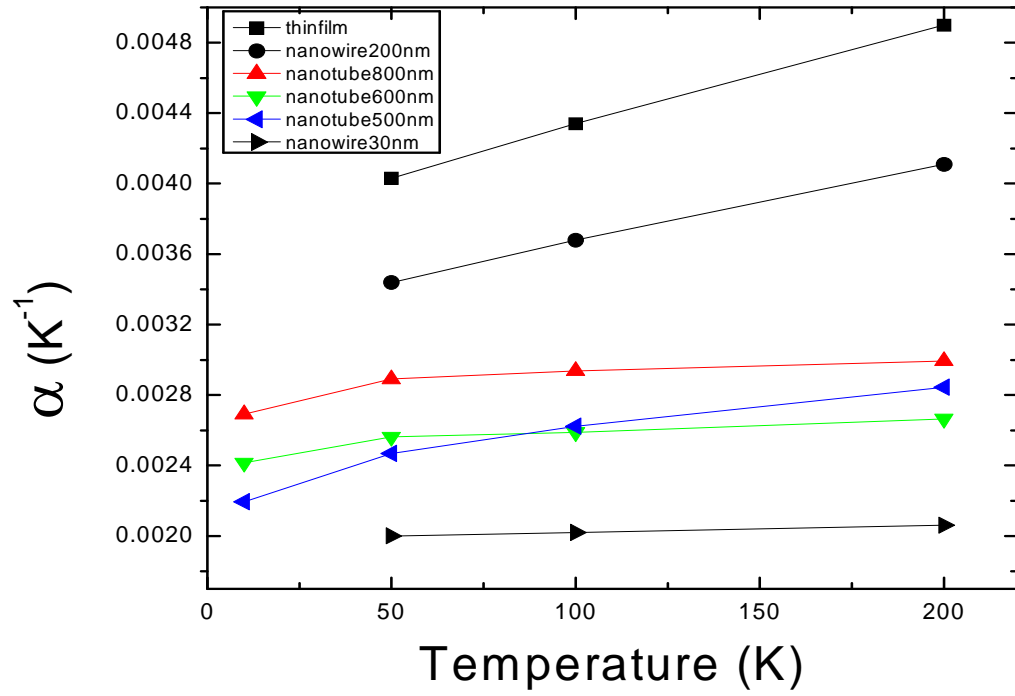


Figure 4.2: Temperature coefficient of resistance for Ni nanotubes

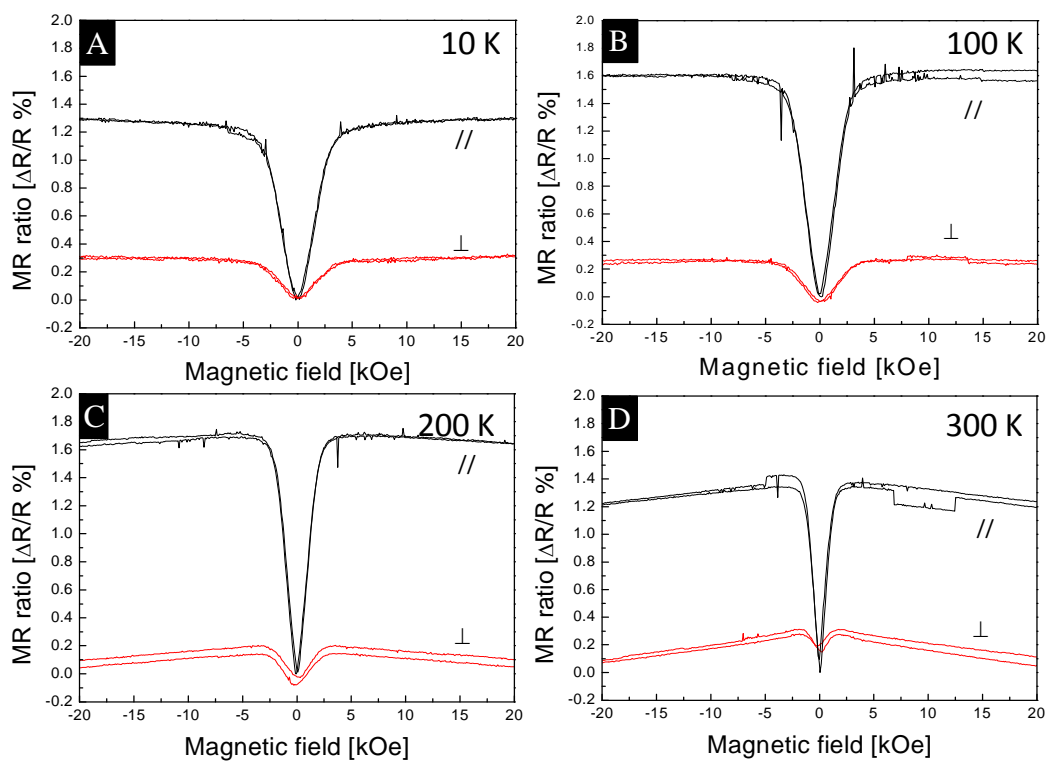


Figure 4.3: Magnetoresistance characteristics of PEDOT/Ni core/shell nanostructure Measured at (a) 10, (b) 100, (c) 200 and (d) 300 K. (//; longitudinal and \perp : transverse direction)

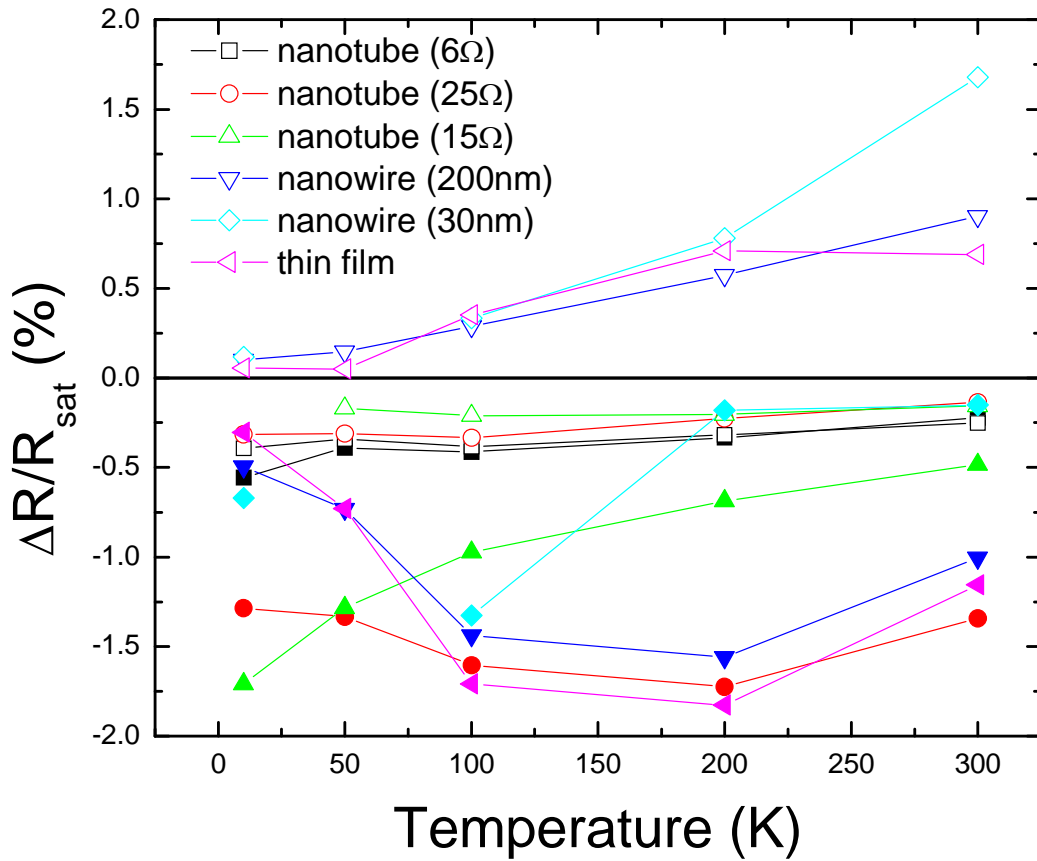


Figure 4.4: Temperature dependent MR properties for Ni thin films, nanowires, and nanotubes. Filled and open shapes correspond to transverse and longitudinal MR measurements, respectively.

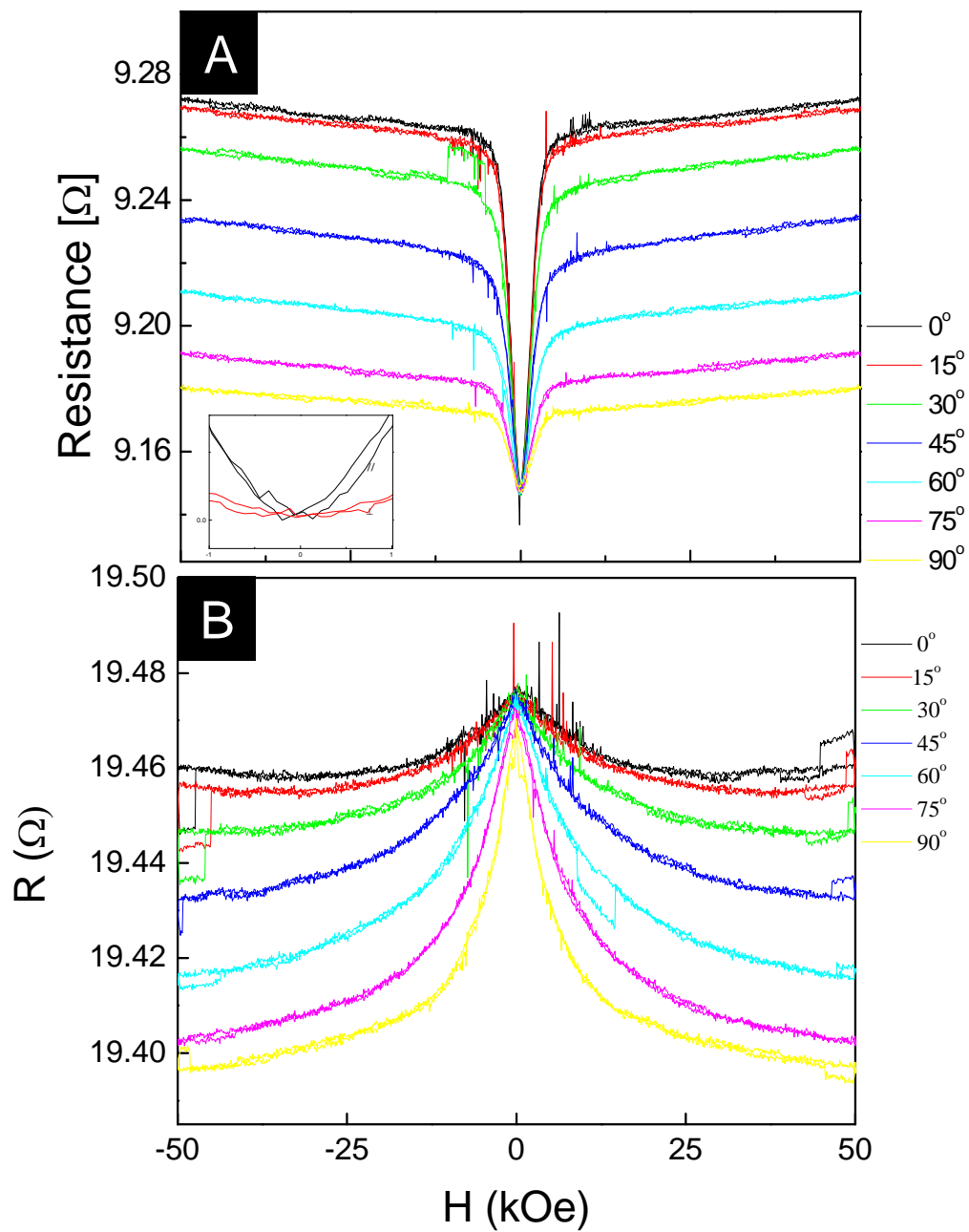


Figure 4.5: Angle dependent magnetoresistance of (A) Ni and (B) $\text{Ni}_{30}\text{Fe}_{70}$ nanotubes at 10K. The inset illustrates the MR hysteresis and minimums at low fields.

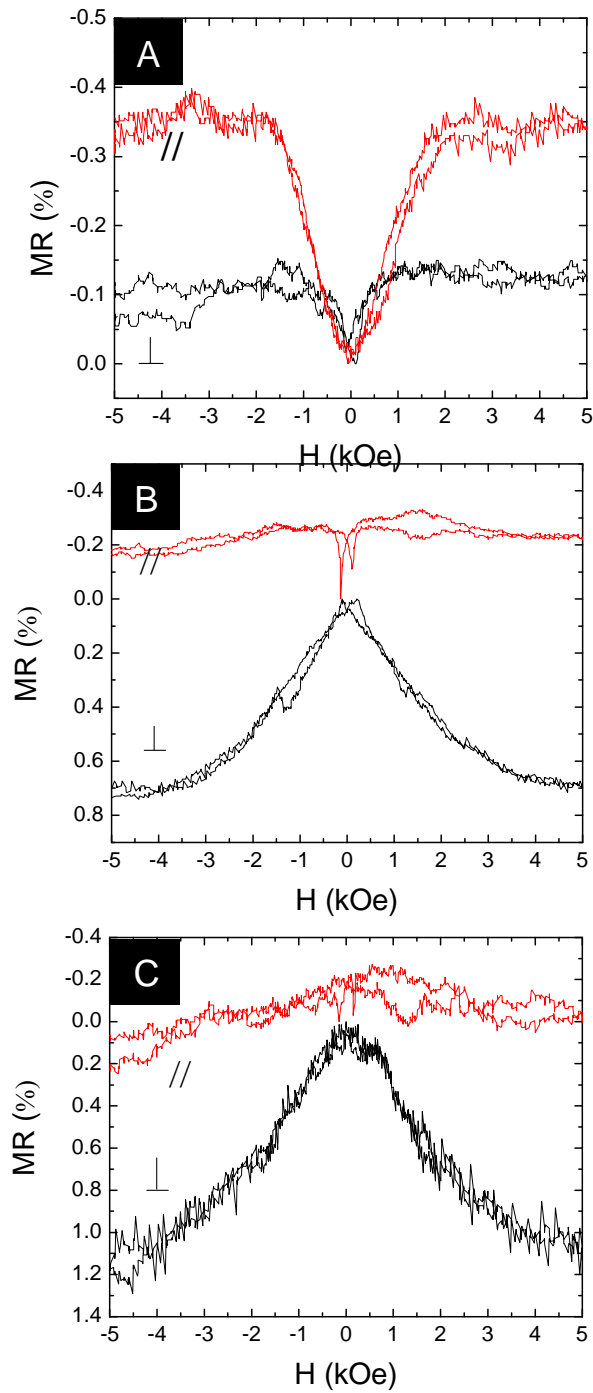


Figure 4.6: Magnetoresistance for an (A) as-synthesized Ni nanotube (14Ω) and after etching to (B) 31Ω and (C) 87Ω . MR curves are red and black for longitudinal and transverse direction, respectively.

Chapter 5: Synthesis of Nanopeapods by Galvanic Displacement of Segmented Nanowires

Abstract

A facile technique to fabricate one-dimensional semiconductor nanostructures with precisely positioned embedded metal nanoparticles, termed nanopeapods, was investigated. These engineered nanostructures have demonstrated enhanced photosensitivity in previous reports and have projected application as plasmon waveguides. The novelty of this report is the use of electrodeposited multi-segmented nanowires with galvanic displacement reaction to create such nanopeapods. This approach utilizes template directed electrodeposition to fabricate nanowires with alternating layers of sacrificial/noble metal, enabling a new level of control over particle spacing, aspect ratio, and composition. Moreover, by exploiting the redox potential dependent reaction of galvanic displacement, nanopeapod materials can be extended (semiconductor/metal, p-type/n-type, metal/metal, ferromagnetic/nonmagnetic, etc.) beyond the fundamental metal/metal-oxide nanopeapods synthesized by high temperature techniques. As proof of concept, Co/Au and Ni/Au multisegmented nanowires were used to create Te/Au nanopeapods by galvanic displacement, producing Te nanotubes and nanowires with embedded Au particles, respectively. Different nanowire diameters and segment lengths were investigated to demonstrate nanoscale precision.

5.1 Introduction

Nanoengineered materials utilize diminutive features to enhance interface/surface properties and overcome limitation of conventional materials. In recent years, progress in this field has been directed towards the fabrication of complex layered nanostructures such as core/shell configurations and advanced assembly techniques for functional arrangements of nanoparticles. Both of these routes, while promising, are in the nascent stages of development largely due to the high level of accuracy and localization required when modulating composition or aligning nanomaterials. One unique structure that has recently emerged with demonstrated enhancement of optoelectronic properties⁵⁰ and promise as precisely fabricated linear assemblages of nanoparticles for plasmon waveguides⁵³ are nanoparticle embedded nanotubes or nanopeapods.

To date, nanopeapods have been fabricated by a limited number of techniques typically requiring either a microwave reactor or a nanoporous template. The former is a specific, complex method with stringent conditions and a solid husk with little evidence for dimensional control over the sheathing material or material variation.⁵⁰ Of the template techniques there are three different approaches that have demonstrated feasibility in terms of material selection and dimensional control.^{54, 115, 116} The first method utilizes a template to fabricate multisegmented nanowires, which are subsequently coated by a nanometer thin porous silica shell using sol gel chemistry. The nanowire consists of alternating layers of noble/base metals (i.e. Au/Ni, Ag/Ni) allowing the more base metal to be chemically etched after the silica coating. The nanoparticle chain materials and dimensions for this process can be finely tuned since they are

determined by electrodeposition of the metal segments and template pore size. The second approach employs a nanoporous alumina template or a nanowire as a template for atomic layer deposition (ALD).¹¹⁶ This process requires ALD of two metal oxide (or polymer) materials, an outer shell and inner sacrificial layer. In the case of the metal oxide template, metal nanowires are then electrodeposited into the double coated nanopores. After etching the template and sacrificial layer the intermediate structure, composed of a metal oxide nanotube partially filled with a metal nanowire, emerges. To delineate the metal nanowire into particles or rods the authors take advantage of Rayleigh instabilities during an annealing process. The procedure is more general with greater material variety of the shell (metal oxides or polymer). The last technique also relies on electrodeposition to generate base/noble metal multilayered nanowires within an alumina template, but solid state reaction differentiates their approach from others. The solid state reaction creates a new tube material by diffusion of the base metal into the alumina template, where Kirkendall effects create the void spaces between the noble nanoparticles.

However, all of the previously described methodologies suffer from one common limitation; the inability to fabricate nanoparticle and shell structures from new interesting materials such as metal/semiconductor, p-type/n-type semiconductor, metal/metal, metal oxide/metal oxide, or ferromagnetic/nonmagnetic. Such a feat introduces a host of fundamentally important studies with applicability to thermoelectric materials, spintronics, nanosensors, and plasmonics. Additionally, modulated nanowire/nanotube structures of the same composition offer an efficient route to study confinement effects

within nanotubes. In this work galvanic displacement of electrodeposited multisegmented nanowires is reported as a simple and scalable method to achieve such nanopeapod structures. This procedure utilizes template directed electrodeposition to fabricate multilayer nanowires, providing the spacing precision of electrodeposition. Since no heat treatment is required for this process embedded particles can range from very thin discs to nanorods. Additionally, more exotic nanopeapod materials are feasible (oxidizable metals, semiconductors, etc.) for galvanic displacement reaction, which depends on half reaction potentials of the nanowire segments and material to be deposited. As proof of concept, Te nanotubes with embedded Au nanoparticles and Te nanowires with embedded Au nanoparticles were fabricated by galvanic displacement reactions.

5.2 Experimental Details

The procedure for fabricating nanopeapods follows that previously described for synthesizing Bi_2Te_3 nanotubes, but utilizes a segmented sacrificial wire with an alternating sequence containing a base element for displacement and a more noble element that remains after the displacement reaction.¹¹⁷ The segmented nanowires were synthesized by template directed electrodeposition, a method pioneered by Martin and Moskovitz, which uses a nanoporous template to confine electrodeposited material radially and the deposition condition to control the axial length of the nanowire. To start, alumina (Whatman Anodisk 13) templates and polycarbonate membranes (Nucleopore 30 and 50 nm) are sputtered with Au on one side using an EMS KX550 sputter coater. The

sputtered Au acts as a seed layer for electrodeposition to proceed upon. In this study alternating layers of Co/Au and Ni/Au were electrodeposited using a dual bath method at different diameters and lengths. After electrodeposition the nanowires were harvested using 1M NaOH at room temperature to etch alumina templates and 1-methyl-2-pyrrolidinone at 50° C to dissolve polycarbonate membranes for eight hours each. The nanowires were washed three times by centrifuging or settling, extracting the solvent and the addition of nanopure water (Millipore A). Portions of nanowire batches were successively transferred to isopropyl alcohol (IPA) by a similar sequence of washings.

All nanowire electrodepositions were carried out in 100mL electrochemical cells with a three electrode configuration using a saturated calomel electrode (SCE) as a reference electrode. The Co electrolyte consisted of 1.0M CoCl₂ + 1.0M CaCl₂ at a pH of 4.0. Co electrodeposition was performed galvanostatically, -10mA/cm², and potentiostatically, -0.96V (vs. SCE), at room temperature with no agitation. The Au segments were electrodeposited from a sulfite-based commercial Technic bath, 25 RTU-ES, containing 40mM of Au at a potential of -0.5V (vs. SCE) or a current density of -1 mA/cm² and a temperature of 50° C with agitation from a 1" stir bar at 300 revolutions per minute.

Synthesis of Ni/Au nanowires followed the same protocol as that of Co/Au nanowire synthesis. The Co electrolyte was simply substituted with a Ni electrodeposition bath. The composition of the bath was 1.5M Ni(NO₂SO₃)₂ + 0.4M H₃BO₃ + 0.2M NiCl₂ at pH 4.0. H₃BO₃ was added as a buffer and NiCl₂ was used to enhance anode dissolution. Ni was electrodeposited galvanostatically at -10mA/cm² in a

two electrode configuration with a Ni counter electrode for alumina templates and potentiostatically in a three electrode configuration at -0.96 vs. SCE for polycarbonate templates.

Galvanic displacement reactions were performed on both substrate bound nanowires and suspended nanowires. The substrate bound nanowires employed Co/Au and Ni/Au multisegmented nanowires suspended in IPA, as the solvent evaporated quickly and provided good nanowire dispersion. The nanowires were cast on Si substrates (0.25 cm^2) and allowed to dry. The substrate bound nanowires were then submerged in 10 μL of the nitric acid Te solution, 1M HNO_3 + 10mM TeO_2 , for 30 minutes. Following the displacement reaction, the solution was carefully wicked with a Kimwipe and washed with a sequence of 10 μL droplet of nanopure water on the substrate and wicking, three times each. Nanowires suspended in nanopure water were used for galvanic displacement in solution. 10 μL of the nanowire suspension was drawn and then dispensed in 1 ml of the Te solution. The nanowires were immediately shaken to prevent agglomeration and to set aside for 30 minutes before washing three times with nanopure water. SEM micrographs were taken with a Phillips XL30 FEG SEM and LEO Supra 55 SEM. TEM micrographs were taken on C coated Cu grids with a FEI Phillips CM300 TEM.

5.3 Results and Discussion

Galvanic displacement reaction has been previously utilized to create a wide variety of metal nanoshells or nanostructures with hollow interiors.^{118, 119} This process was later adopted to yield multi-walled metal nanoshells with shells of different metal composition.^{120, 121} Recently, our group has also extended galvanic displacement reactions to generate semiconductor and compound semiconductor nanotubes from ferromagnetic nanowires.¹¹⁷ However, to date galvanic displacement has not been implemented with segmented bimetallic nanowires or to create metal/semiconductor nanostructures, wherein one metal component is displaced by a semiconductor material and the other is retained. Thus, methodical incorporation of semiconductor nanomaterials with prearranged bimetallic nanowires is a critical step, drastically augmenting the utility of galvanic displacement of nanostructures.

The driving force for galvanic displacement reactions is the difference in redox potentials, a fundamental electrochemical process described in every freshman chemistry course. The mechanism for creating hollow nanostructure by galvanic displacement reactions has been described previously by Xia's group.¹¹⁸ The generalized scheme starts with particle nucleation and growth of the more noble material on the surface of the sacrificial metal nanostructure, forming a thin, porous sheath. As the shell fills in, diffusion across the casing allows for continued oxidation/dissolution of the sacrificial metal. The end result is a hollow nanostructure with an interior roughly resembling the exterior of the sacrificial metal.

The procedure, as applied to the Co/Au multilayered nanowire system, is shown in figure 1. In these experiments Te coats the Au segments as it encapsulated the volume of the pre-existing Co segment. This feature is a result of the difference in electrode potentials of each metal in the bimetallic nanowire. As a consequence, Co/Au bilayers also behave as conjoined electrodes of an electrochemical cell, with Au as a cathode for Te deposition and Co as the dissolving anode. SEM images of the Co/Au nanowires and the Au particle embedded Te nanotube are shown in figure 2(A-B). The segments of the Co/Au nanowire are shown to be $\sim 2\mu\text{m}$ and $\sim 1\mu\text{m}$, respectively. A distinct change in morphology after displacement indicates the entire structure has been coated. The rough surface of the Te tube with the globular appearance at high magnification in Figure 5.2C may be a consequence of surface roughness from the Co oxide layer or even the initial porosity that is enables continued dissolution of the Co across the Te shell. However, similar morphological coatings on the Au segments suggest it may also be a result of the growth mechanism, which is likely due to low nucleation and surface mobility, typical factors causing botryoidal deposits. This suggests increasing the temperature may provide a means to improve crystallinity.¹²² The transparency of the Te allows the Au segments to be visually located with SEM and reveals a fairly consistent outer diameter for the Te nanotube, especially for coatings over the Au segments. The displacement of Co by Te after the galvanic displacement reaction was verified by energy dispersive X-ray spectroscopy (EDX). The EDX spectrum in Figure 5.2D clearly indicates the absence of Co and the appearance of Te.

The TEM images in Figure 5.3 reveal the solid wire and tube cross section. The Co/Au nanowires can be clearly differentiated in Figure 5.3B, with the Co segments approximately $2\mu\text{m}$ in length and the Au segments, darker in color, are $\sim 1\mu\text{m}$ in length. The thick, fragmented oxide layer on Co gives the appearance of a hairy nanowire. The enlarged image the Te tube segment, after displacement, reveals the granular structure, with small grains. The structure of the Te coating was verified by selected area diffraction pattern (Figure 3C inset), revealing a polycrystalline structure in agreement with similar results.¹²³ Although polycrystalline in nature, previous demonstrations of refluxing at elevated temperatures may improve the crystallinity, in accord with the observed microstructure.¹¹⁸ Additionally, the wall thickness ranges from 10nm to about 27 nm with an inner diameter of roughly 225-250nm. The variation in tube diameter can be attributed to poor Co/Au interfaces, likely due to oxidation between depositions as a result of rinsing with water, or uneven Co surfaces due to template imperfections. Interfacial quality can be ameliorated by selection of an acid Au bath or a single bath with pulsed electrodeposition.

Smaller Au/Te nanopeapod structures were also fabricated from polycarbonate templates. Although the nominal pore size of these templates was 30nm the Au segments are shown to have a diameter of $\sim 65\text{nm}$. The wall thickness of the Te tube in Figure 5.4A is measured to be $\sim 12.5\text{nm}$ with an outer diameter of 75nm, indicating a slight contractions from the original Co segment diameter. This contraction is likely a consequence of the larger aspect ratio of the sacrificial Co segment, which is double that of the alumina template Co segment, permitting slight tube collapse prior to filling in.

The decrease in wall thickness from the larger diameter Te/Au nanopeapod is in accord with the reduced volume of the sacrificial Co. Additionally, the Te tube has a much more pronounced botryoidal microstructure, which also appears on the Au segment.

In contrast to Co/Au, Ni/Au multisegmented nanowires produced distinctly different nanopeapods. The mechanistic nanopeapod formation described in Figure 5.1 does not apply to nanopeapods formed from Ni/Au nanowires. The structure of these nanopeapods is a Te nanowire with embedded Au segments. The mechanism for nanowire, as opposed to tube, formation between Au segments is likely due to the more positive electrode potential of Ni, with respect to Co, slowing down the displacement kinetics and reducing electron transfer between the bimetallic Ni/Au electrode junctions. This shift in potential may also provide kinetic favorability for etching or displacement along grain boundaries, which would allow progressive contraction of the Te deposit as the Ni is displaced.

Representative SEM images of the Ni/Au multisegmented nanowires are shown in Figure 5.5. Numerous variations of the Ni and Au segment lengths were investigated for both alumina and polycarbonate templates. EDX analysis of Ni/Au nanowires before galvanic displacement in Figure 5.5(A) indicate strong peaks for both elements. After galvanic displacement, Figure 5.5(B), the Ni peak is drastically reduced and Te appears. Additional Ni/Au nanowires with different diameter and segment lengths are shown in Figure 5.5 (B-D). TEM images with EDX line scans and selected area electron diffraction patterns of 200nm Ni/Au nanowires are shown in Figure 5.6. The EDX line scan clearly shows the delineation of the segments. In Figure 5.6 (B) a compromised

interface, presumably resulting from Au electrodeposition on Ni, is shown. This weaker junction alternates, as shown by the inset, with every other interface, consistent with pH induced oxidation or etching of Ni during Au electrodeposition. The SAED patterns of a single nanowire and selected area show the polycrystalline structure of the Au/Ni segments, consistent with previous reports of Ni and Au nanowires electrodeposited from a sulfamate and sulfite bath, respectively. The corresponding d-spacing values and orientations for Figure 5.6 (F) are shown in Table 5.1. The Au segments have plane spacings of (100), (200) and (422) with unit cell edge lengths, calculated for Au as a face centered cubic structure, of 3.810, 4.092, and 4.025Å, respectively. These values are reasonably close to the JCPDS value of 4.0786Å. The Ni plane spacings appearing from the SAED patterns are (111), (200), (220), (311), and (440), with a= 3.527, 3.564, 3.623, 3.588, and 3.568Å, which also lie close to the literature value a=3.5238Å.

TEM results for galvanic displacement reaction of Ni/Au nanowires grown from 50nm polycarbonate templates are shown to be approximately 115nm in diameter (Figure 5.7). The Ni appears to be etched to near completion being replaced with granular Te segments. Lattice fringes from high magnification TEM images of the Te/Au interface reveal the Te granules to be as large as 6nm. SAED patterns suggest a mixed polycrystalline/amorphous structure and small grain sizes for the Te segment with d-spacings for Figure 5.7 (L) shown in Figure 5.7 (I) and given by Table 5.2 with their respective a values. The large deviation in a, given in Å in all tables, from the literature value of 4.4579Å suggests considerable defects or impurities and is confirms the suspected partial amorphous structure. The gold segments display a predominately

polycrystalline structure with larger grains relative to Te, as depicted by Figure 5.7 (H-I). Contrary to larger Ni/Au multisegmented nanowires, these samples displayed minimal Te deposition on the Au segments. However, the Te top-coat may have contributed to the stronger deviations in a values from those reported for as synthesized Ni/Au nanowires (Table 5.3). Darkfield images of these nanowires also highlight the granular structure of the Te segments and lack of tubular structure (Figure 5.8). The EDX area scans of one such Te segment depicts that Te is uniformly mapped over all segments along with Ni. The high concentration of Ni, $\text{Ni}_{0.441}\text{Te}_{0.559}$ by EDX, is an important factor contributing to the plane spacing deviations and suggest the formation of intermetallic NiTe, which is thermodynamically more favorable to Ni and Te (Figure 5.8 (D-F)).¹²⁴ The corresponding NiTe planes and a values for Figure 5.8 (I) are shown in Table 5.4. Some d-spacing values produce better lattice edge length fittings to NiTe ($a=3.9293\text{\AA}$) than Te.

The TEM images for nanowires fabricated from 30nm polycarbonate membranes show the actual nanowire diameter to be $\sim 75\text{nm}$. The Te/Au interface of a Ni/Au nanowire subjected to galvanic displacement reaction is shown in Figure 5.9. These wires appear very similar to those fabricated from 50nm polycarbonate membranes. The high magnification TEM images show a granular structure for the Te but with comparably smaller and less lattice fringes, which agrees with the nearly amorphous SAED pattern. The Te coating on the Au is also more pronounced on these wires with thickness from 2-6nm. Although the SAED pattern is nearly amorphous, two points are distinguishable and have been assigned planes of (200) with very good lattice edge length fittings to both Te and NiTe (Table 5.5 and 5.6), however the intensity values for the

NiTe plane spacing is much stronger than the Te. This supports the possibility of NiTe intermetallic formation, but is difficult to confirm by SAED pattern alone. The SAED pattern for the Au segments on these nanowires is similar to that of the previous nanowire, with good fitting lattice edge values except for a couple spots that can be attributed to the Te coating (Table 5.7).

5.4 Conclusions

A new approach was investigated for the synthesis of nanopeapods, with one material discontinuously embedded within the core of a different material. This technique utilized template directed electrodeposition to fabricate a multisegmented nanowire of Co/Au, where Co serves as the sacrificial metal for galvanic displacement and Au becomes encapsulated by the Te coating. The Te coating over the Au was attributed to the difference in electrode potentials of the Co and Au, allowing Au to mediate charge transfer from Co to HTeO_2^+ . The displacement reaction was demonstrated with both alumina and polycarbonate template fabricated nanowires. SEM images revealed a botryoidal microstructure, which was also shown by TEM and attributed to low nucleation and surface mobility. The wall thickness of the nanopeapods was dependent on the quantity of sacrificial Co, decreasing from ~20nm to 12.5nm as the initial diameter of the sacrificial Co segments decreased from 225nm to 65nm. The smaller diameter nanopeapods exhibited slight contraction of their tube segments, probably resulting from the increased aspect ratio. Utilizing Ni sacrificial segments in a Ni/Au bilayer nanowire configuration produced Te nanowires with embedded Au

segments. The different structure was attributed to the difference in electrode potentials of Co and Ni. Furthermore, EDX and SAED patterns supported intermetallic NiTe formation as opposed to elemental Te. Finally, this approach is believed to be a more general route to nanopeapod synthesis as numerous template directed electrodeposition materials can be incorporated, including conducting polymers, magnetic materials, metal oxides, and compound semiconductors.

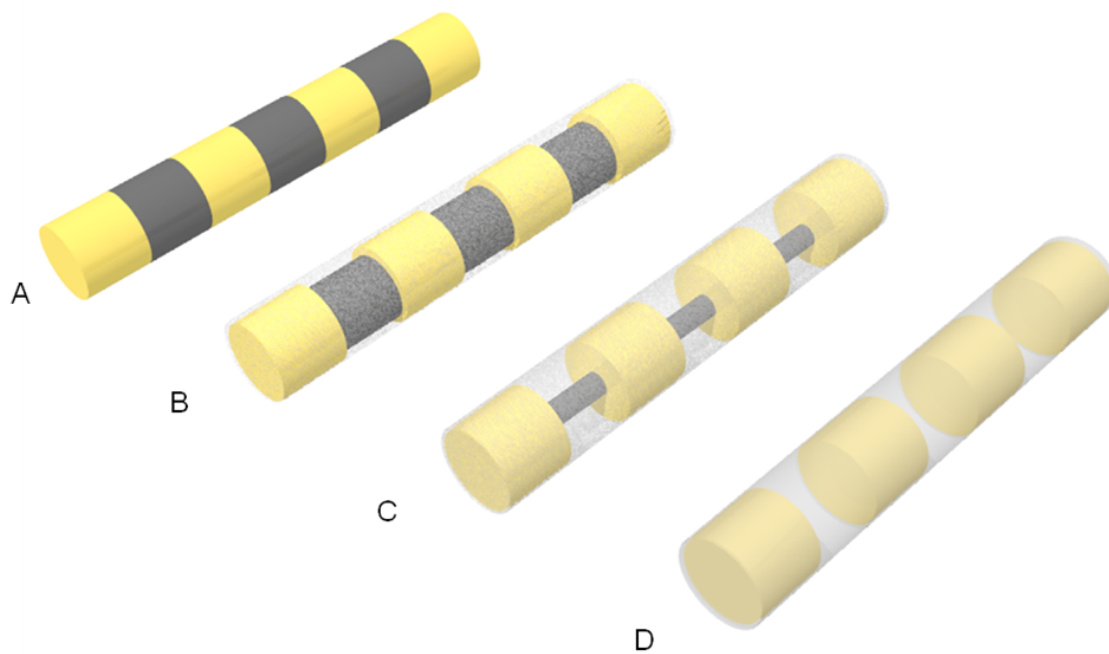


Figure 5.1: Schematic of galvanic displacement reaction progression for Co/Au multisegmented nanowires. (A) The as synthesized Co/Au nanowire is (B) sheathed in a thin porous Te coating (C) that permits continued dissolution of the Co segments as the Te coating continues to grow, (D) until the Te tube with embedded Au particles is all that remains.

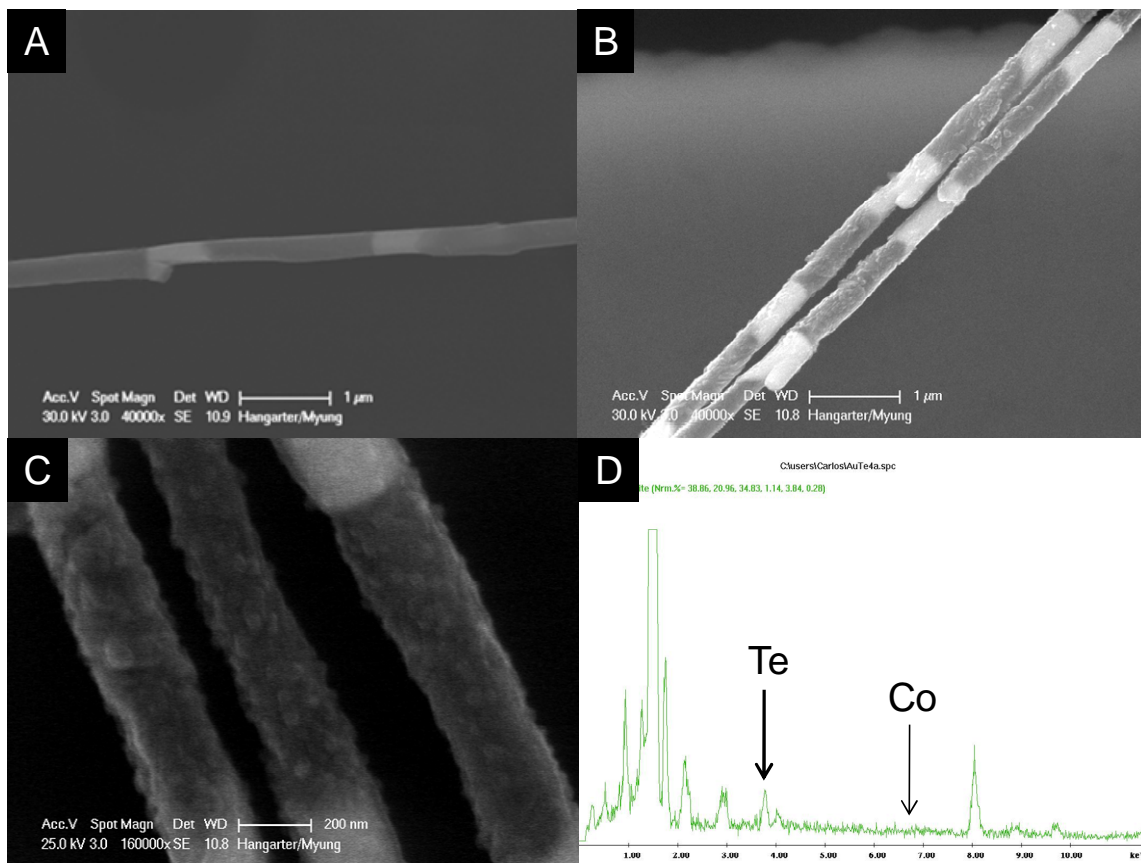


Figure 5.2: SEM images of (A) electrodeposited Co/Au multisegmented nanowires and (B, C) the corresponding Au/Te nanopeapod structure synthesized by galvanic displacement. (D) The EDX spectrum of image (C) indicates the presence of Te and no detectable concentration of Co. Additional peaks pertain to the Au segments, 2.12 keV, and substrate materials, Cu 8.04 keV and Al 1.48 keV.

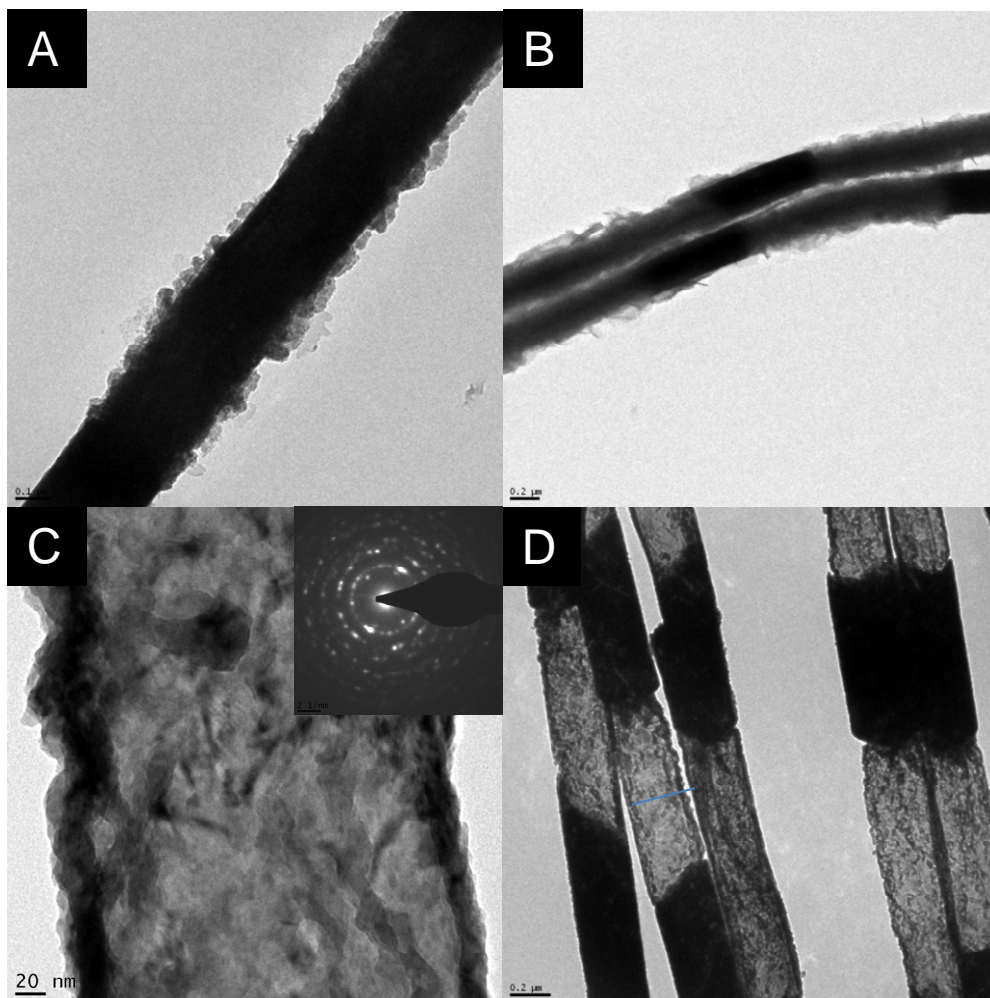


Figure 5.3: TEM images of (A-B) Co/Au multisegmented nanowires and (C-D) Te/Au nanopeapods. EDX and SAED patterns for Co/Au nanowires (E-F) before and after (G-H) galvanic displacement are also shown. Scale bars are 20nm and 200nm for (C) and (A, B, D), respectively

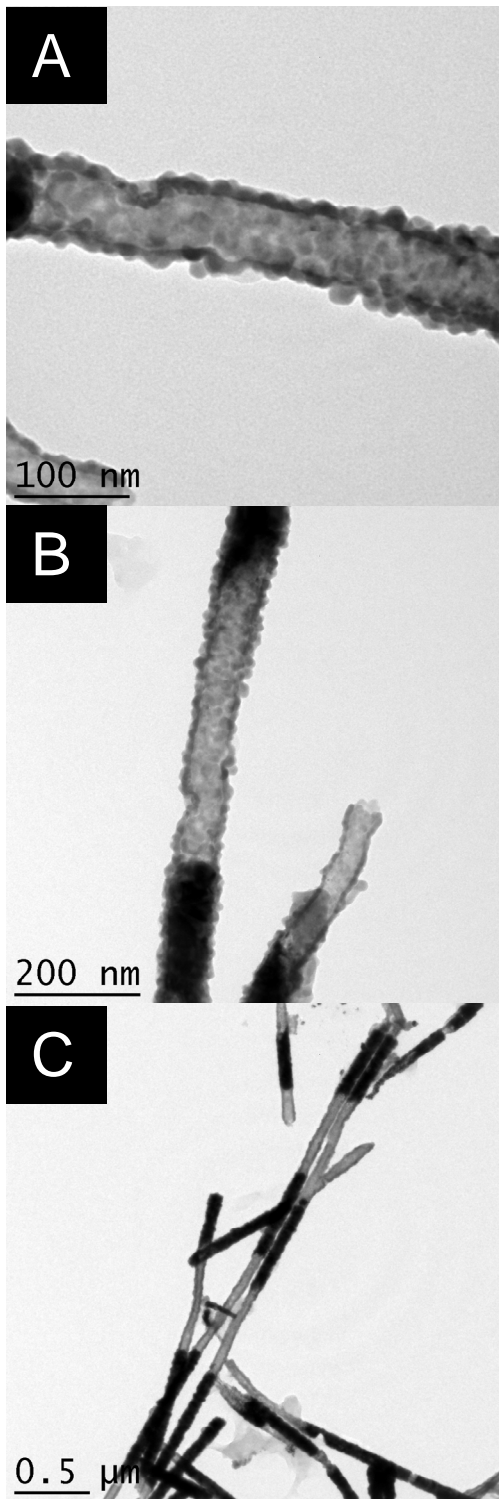


Figure 5.4: TEM images of Au/Te nanopeapods produced from a 30nm polycarbonate template. Scale bars are clearly indicated.

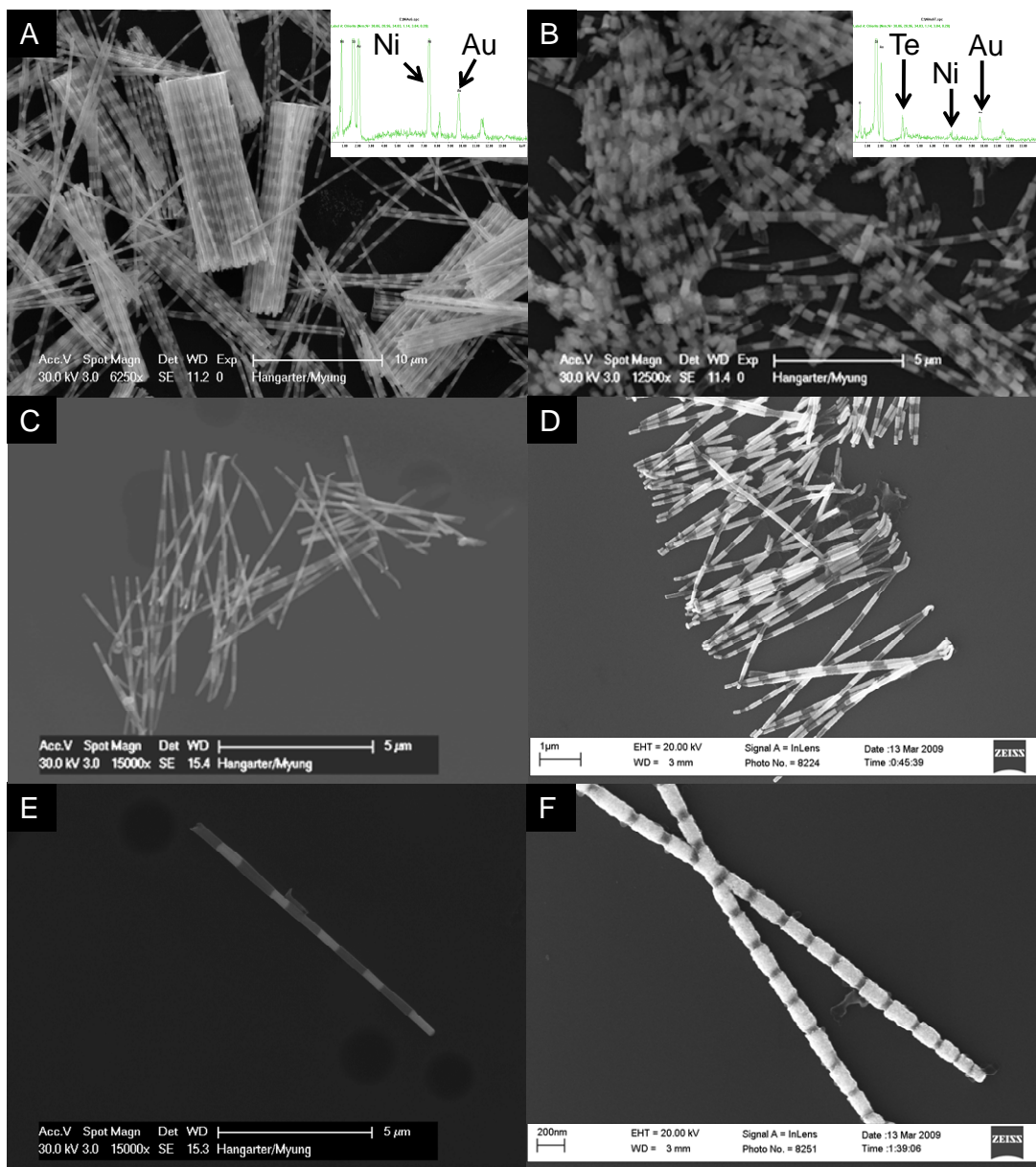


Figure 5.5: SEM images of Ni/Au nanowires fabricated from (A) 200nm alumina templates and (C) 30nm polycarbonate membranes. The coated structures after galvanic displacement are shown in (B) and (D) for alumina and polycarbonate, respectively. The insets of (A-B) are EDX patterns for their corresponding images. (E-F) SEM images of (E) 200nm Ni/Au and (F) 50nm galvanically displaced Ni/Au nanowires with different segment lengths. Scale bars (A) 10, (B-C, E) 5, (D) 1, and (F) 0.2 μ m.

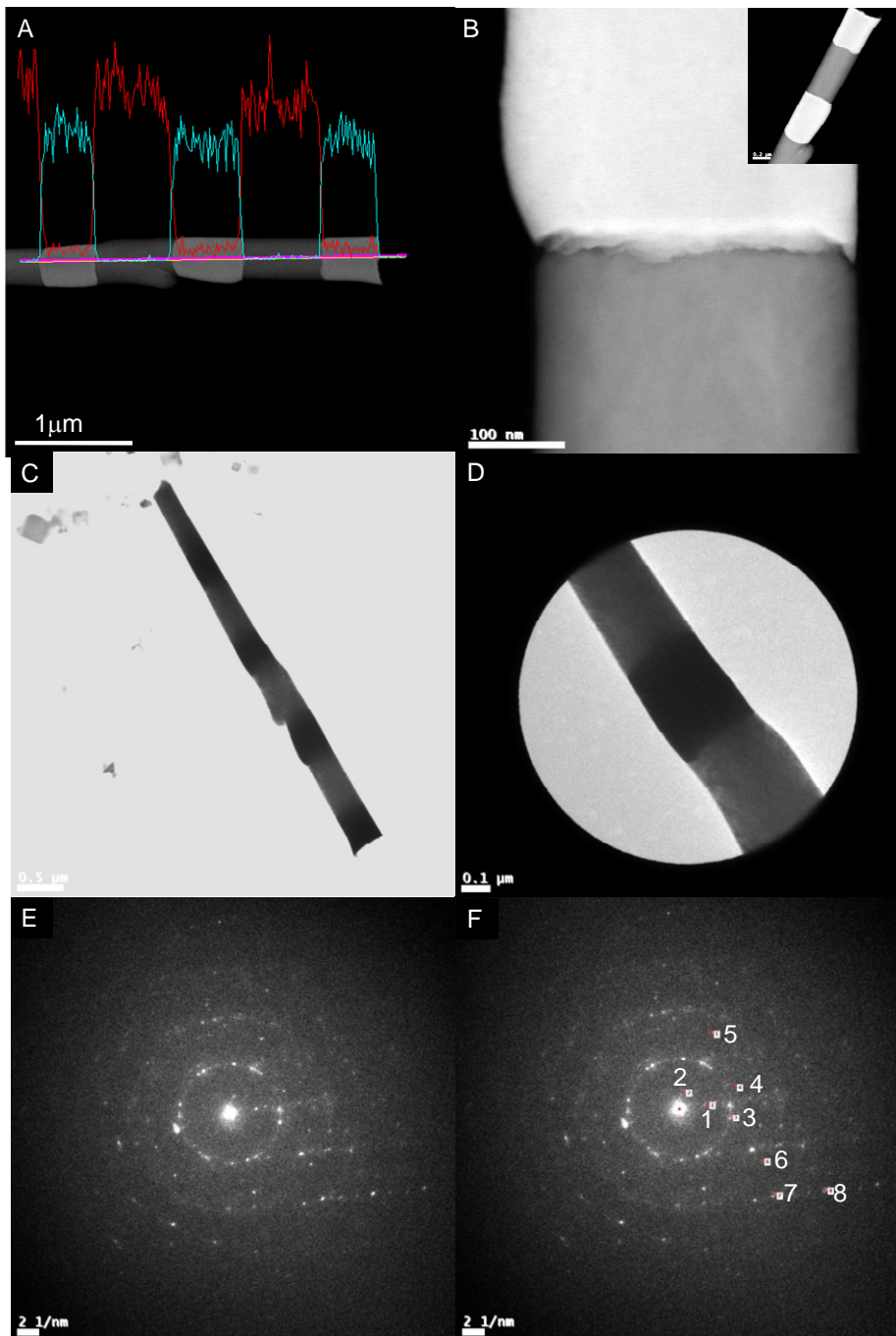


Figure 5.6: (A-B) Darkfield and (C-D) brightfield TEM images of Ni/Au nanowires. (A) The EDX line scan confirms segment contrast for (red) Ni and (blue) Au. (D) The brightfield TEM images corresponds to the (E-F) SAED patterns below. Scale bars (A) 1, (C) 0.5, and (B, D) 0.1 μm .

Table 5.1: D-spacing values for the numbered spots from Figure A1.2 (F) and corresponding element, plane, and unit cell edge length (a).

Spot	d-spacing (nm)	Element	Plane	a
1	0.3818	Au	100	3.818
2	0.6116	Ni	111	3.527
3	0.2046	Au	200	4.092
4	0.1782	Ni	200	3.564
5	0.1281	Ni	220	3.623
6	0.1082	Ni	311	3.588
7	0.08216	Au	422	4.025
8	0.06308	Ni	440	3.568

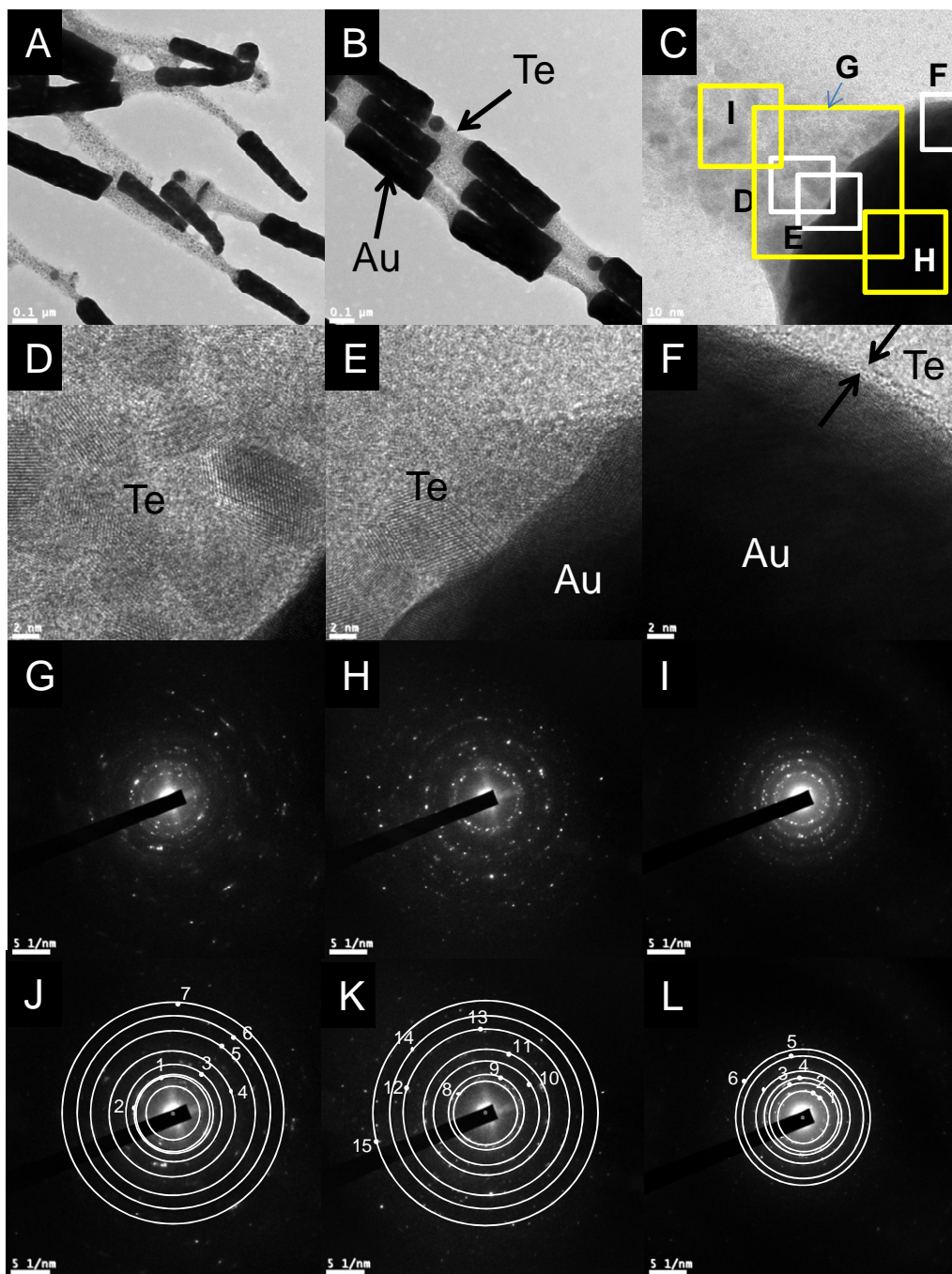


Figure 5.7: (A-F) Brightfield TEM images of Ni/Au multisegmented nanowires synthesized from a 50nm polycarbonate template after galvanic displacement. The boxes in (C) correspond to the images in (D-F) and SAED patterns in (G-I). The SAED patterns (J), (K), and (L) are the exact same SAED patterns as (G), (H), and (I), respectively, with numbered spots and corresponding white rings for d-spacing values in Table 5.2 and 5.3. The scale bars are (A-B) 100, (C) 10, and (D-F) 2nm.

Table 5.2: D-spacing, plane and unit cell edge length for Te from Figure 5.8 (I, L).

Spot	d-spacing (nm)	Plane	a
1	0.2795	101	3.659883
2	0.2792	101	3.654834
3	0.2148	111	4.609348
4	0.1947	003	0
5	0.1605	202	4.409229
6	0.1211	114	4.203072
7	0.1138	105	4.693809

Table 5.3: D-spacing, plane and unit cell edge length for Au from Figure 5.8 (H, K).

Spot	d-spacing (nm)	Plane	a
8	0.2657	111	4.600
9	0.1926	200	3.852
10	0.1348	220	3.812
11	0.1191	222	4.126
12	0.09891	331	4.311
13	0.09266	420	4.146
14	0.08230	422	4.032
15	0.07045	440	3.988

Table 5.4: D-spacing, plane and unit cell edge length for NiTe from Figure 5.8 (I, L).

Spot	d-spacing (nm)	Plane	a
1	0.2795	101	3.780839
2	0.2792	101	3.775273
3	0.2148	102	4.139732
4	0.1947	110	3.894
5	0.1605	201	3.884438
6	0.1211	203	3.800304
7	0.1138	300	3.942148

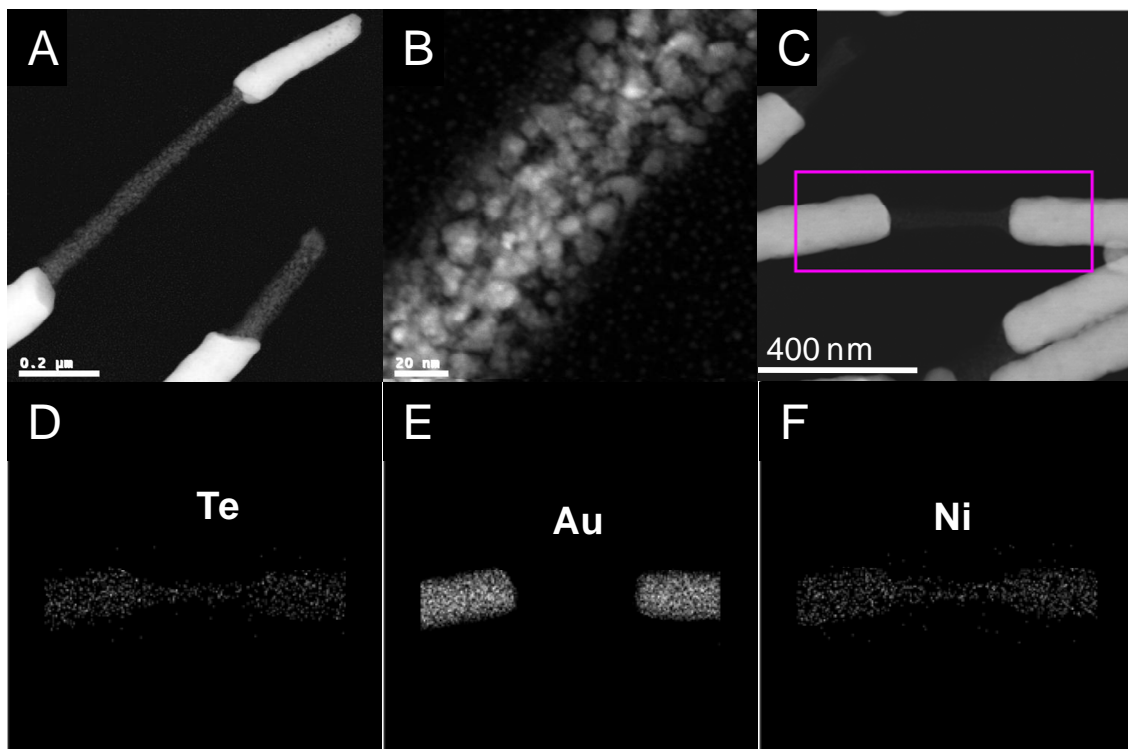


Figure 5.8: (A-C) Darkfield TEM images of Ni/Au nanowires fabricated with 50nm polycarbonate templates and subjected to galvanic displacement reaction with Te. The box in (C) indicates the area of the EDX mapping for (D) Te, (E) Au, and (F) Ni. Scale bars are (A) 200, (B) 20, and (C) 400nm.

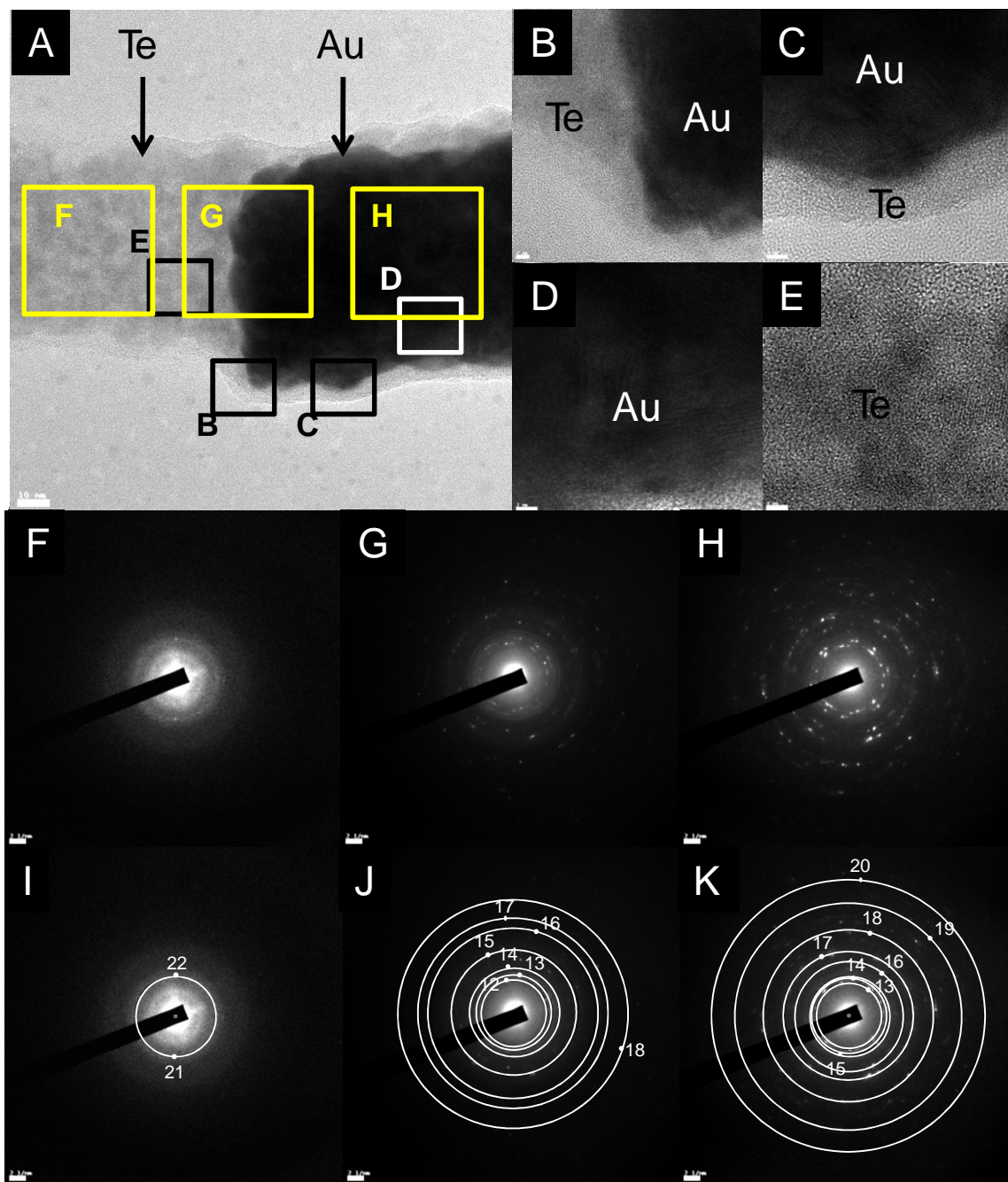


Figure 5.9: (A-E) Brightfield TEM images of Ni/Au multisegmented nanowires from 30nm polycarbonate template after galvanic displacement. The boxes in (A) correspond to the images in (B-E) and SAED patterns in (F-K). The SAED patterns (I), (J), and (K) are the exact same SAED patterns as (F), (G), and (H) respectively, with numbered spots and corresponding white rings for d-spacing values from Tables 5.4 and 5.5. The scale bars are (A) 10 and (B-E) 2nm.

Table 5.5: D-spacing, plane and unit cell edge length for Te from Figure 5.10 (I).

Spot	d-spacing (nm)	Plane	a
21	0.1940	200	4.4802
22	0.1943	200	4.4871

Table 5.6: D-spacing, plane and unit cell edge length for NiTe from Figure 5.10 (I).

Spot	d-spacing (nm)	Plane	a
21	0.1940	110	3.88
22	0.1943	110	3.886

Table 5.7: D-spacing, plane and unit cell edge length for Au from Figure 5.10 (K).

Spot	d-spacing (nm)	Plane	a
13	0.2304	111	3.990
14	0.2099	200	4.198
15	0.1932	200	3.864
16	0.1422	220	4.022
17	0.1252	311	4.152
18	0.09215	420	4.121
19	0.06839	440	3.868
20	0.05749	444	3.983

Chapter 6: Summary and Conclusion

One-dimensional nanostructures have been highlighted for their ability to enhance device performance and integrate new functionality. These functionalities can be incorporated by higher level nanostructures, such as nanopeapods, core/shell, and multilayer nanowires, which adopt new properties from their separate components or through interfacial properties. However, accessing these properties typically requires novel synthesis schemes and/or fabrication techniques that address assembly, electrical contact, and manufacturability. Additionally, thorough examination of the structure and physical properties of these nanoconstructs is essential to distinguish true properties from procedural manifestations such as contact resistance or induced defects. Hence, single nanowire devices that eliminate nanowire-nanowire interactions such as electrical contact or magnetic perturbations are essential. These underlying themes were applied to the development and investigation of individual conducting polymer nanowire devices for gas sensing and hybrid magnetic structures as well as nanopeapod devices.

Single PPy and PEDOT nanowire devices were demonstrated as transducers for gaseous molecules of ammonia and several VOCs. The basis of this work was the development of a contact method described in Chapter 2 as maskless electrodeposition. This technique addresses instabilities of line contacts between conducting polymer nanowires and prefabricated microelectrodes. Although networks or loosely bound individual conducting polymer nanowires have been previously demonstrated, they are not robust by design. Conversely, maskless electrodeposition was shown to selectively electrodeposit metals on prefabricated microelectrodes, thereby engulfing the nanowire

ends for solid mechanical joints with improved electrical contact due to the drastic increase in interfacial area between the nanowire and electrode. The result of which was enhanced sensor performance. Moreover by utilizing A.C. dielectrophoretic assembly the manufacturability of single conducting polymer devices was drastically improved. Heterogeneous conducting polymer nanowire arrays based on individual nanowire elements are now feasible, in which these devices are limited more by lithographic design than any other factor. The improved manufacturability of these devices was utilized to tune the sensing properties of PEDOT nanowires. These studies allowed the electrical properties to be correlated with the sensing performance and provided insight on the underlying cause for substantial sensitivity enhancement to more hydrophobic VOCs.

Maskless electrodeposition was further modified to fabricate single core/shell nanostructures. For these devices a non-selective electrodeposit was employed for site specific deposition of a positive PEDOT nanowire template bridging two electrodes. The in-situ component of this approach was key to establishing good electrical contact. The magnetoresistance response of these devices deviated drastically from the anticipated AMR response. Temperature, angle and material dependent properties indicated magnetostriction as the likely source for their behavior. These devices exhibited an enhanced sensitivity to magnetostriction, which was attributed to their thin tubular wall. The soft polymer core, which behaved similar to a hollow core, permitted the reversible elongation and contraction of the ferromagnetic nanotubes. While the response was not giant in magnitude it is conceivable that magnetostriction induced MR could be

significantly enhance by engineered magnetostrictive materials and coupling with other MR technologies.

Finally, in an effort to develop novel hierarchical nanostructures, galvanic displacement was investigated for the synthesis of nanopeapods, in which a nanotube material contains discrete nanoparticles embedded in its core. Moreover the fact that these particles are embedded in tandem designates these structures as potential candidates for plasmon waveguides. The process utilized template directed electrodeposition of multisegmented nanowires and galvanic displacement of the sacrificial segments to synthesize these structures. This procedure was demonstrated to fabricate ~200nm and ~75nm diameter Au/Te nanopeapods from Co/Au nanowires. A completely new nanopeapod structure, Te nanowires with embedded Au segments, were fabricated from Ni/Au nanowires. These experiments provide a basis for structural engineering through electrode potential of the electrodeposited nanowire and galvanically deposited material.

Although strides in synthesis and fabrication of nanostructures, described herein, have improved manufacturability and enabled characterization and performance tunability of select devices, high throughput production of nanodevices will remain the largest hurdle for nanoscience in the years to come. Contrary to individual demonstrations, nanomanufacturing must achieve a yield, precision, and scalability rivaling lithography. While manipulation and assembly of suspended structures has attracted renowned attention, the magnitude of this task will require relentless development in the years to come.

Appendix 1: Pulsed Electrodeposition of Ni₈₀Fe₂₀/Cu Multilayer Nanowires

A1.1 Experimental Details

The templates used for these nanowires were commercially available Whatman Anodisk 13 templates with a nominal pore diameter of 200nm, and in-house anodized aluminum 30 nm templates. The anodized 30nm templates were made from a 1 inch² piece of aluminum, which was fastened in a hand-made template. The working area of the aluminum was then cleaned two times with 1 M NaOH to smooth the working area and remove the native oxide layer. Afterwards, the template was dipped in a 1.8M H₂SO₄ solution and a 15V potential was applied for 15 minutes. After the 15 minutes, a 20V potential was applied for two hours. Once the anodizing was complete, the template was rinsed, cut out, and the copper was removed. When the 200nm and 30nm templates were obtained, an Emitech K550 sputtering machine was used to coat the templates six times at 20mA for 4min cycles with gold to create a conductive seed layer for electrodeposition.

For the depositions, an SCE and a platinum counter electrode were used in a three electrode configuration. For Au/ NiFe/Au nanowires the Au gold was deposited first and last at 50 °C at -0.5V vs. SCE with agitation from a 1” stir bar at 300rpm. In these experiments, a bath with a composition of 1M NiSO₄ + 0.5M H₃BO₃ + X M of FeSO₄ where X = 0, 0.05, 0.1, 0.2, 0.3, and 0.5 was used. Electrodepositions were performed with agitation from a 1” stir bar at 300rpm and ambient temperature and pressure. The pH

of the bath was adjusted to 3 with concentrated sulfuric acid. Boric acid was added to buffer the bath and the electrolyte was purged with N_2 to reduce Fe^{2+} oxidation. The NiFe electrodepositions were conducted at $-1.2V$ and $-1.4V$ to see the variations in compositions due to potential. The length of the nanowires was controlled by charge, using the electrode area and porosity to calculate the theoretical amount of charge needed to deposit $1\mu m$ based on 100% efficiency. Electrodeposition of $Ni_{80}Fe_{20}/Cu$ multilayers was performed by the addition of 1, 5, and 10mM $[Cu^{+2}]$ to the appropriate NiFe electrolyte. The $Ni_{80}Fe_{20}/Cu$ multilayers were electrodeposited from the same bath by modulating the potential to the experimentally determined potentials for each material. The layer thickness was controlled by charge. All electrodeposition experiments were carried out with an EG&G Princeton Applied Research VMP-2 Galvanostat/Potentiostat.

The composition dependent magnetic properties of the Au/NiFe/Au nanowires were analyzed in the template with a Digital Measurements Systems Model 1600 vibrating sample magnetometer. The compositions of the NiFe nanowires were determined by dissolving the nanowires in 50% (v/v) HNO_3 and analyzing with a Perkins Elmer atomic absorption spectrometer (AAS). Images and measurements were taken with a Phillips XL30 FEG scanning electron microscope (SEM) and FEI Phillips CM300 transmission electron microscope (TEM). Some nanowire compositions were analyzed with EDAX.

A1.2 Results

Segmented Au/NiFe/Au nanowires with lengths of $2/1/2\mu\text{m}$ were grown in both 200 and 30nm alumina templates as shown in Figure A2.1. The first Au segment served to inhibit branching between NiFe, thereby preventing deposition variation due to substrate incongruities and yielding more useful magnetic measurements. The second segment was added to reduce oxidation of the NiFe nanowire end. The low purity, <99.9%, of the unannealed Al samples and single step approach used for anodization produced large, numerous defects in the template as shown in Figure A2.1(B). These defects along with the much smaller pore diameter in the 30nm templates produced considerable dispersity among nanowire length and composition.

The 200nm nanowires were selected for further investigation due to their controllable deposition and compatibility with single nanowire device fabrication. The Fe content in the electrodeposited nanowires was characterized as a function of the electrolyte $[\text{Fe}^{+2}]/[\text{Ni}^{+2}]$ ratio, displaying a monotonic increase for -1.2V and slight fluctuation for -1.4V. A composition of $\text{Ni}_{82}\text{Fe}_{18}$ was obtained with 0.1M FeSO_4 (Figure A2.2), which is nearly the same as stoichiometric $\text{Ni}_{80}\text{Fe}_{20}$ for all practical purposes and nanowires synthesized from this bath will be referred to hereafter as $\text{Ni}_{80}\text{Fe}_{20}$. The NiFe nanowires were also characterized in terms of their magnetization saturation (M_S), coercivity (H_C), and squareness (M_R/M_S), the results of which are depicted in Figure A2.2. The M_S follows the expected trend, increasing with increasing Fe content as M_S is an intrinsic property dependent only on composition. The skewed M_S trend for deposition at -1.4V vs. SCE is probably due to the eradicate changes in Fe content by

comparison to the monotonically increasing Fe content for -1.2V vs. SCE with respect to $[\text{Fe}^{+2}]$. The coercivity and squareness, extrinsic properties dependent on stress, shape anisotropy, microstructure, etc., may fluctuate more for -1.4V due to templates differences, which can vary from 200 to 300 nanometers changing the shape anisotropy considerably for such small sample volumes.

Further development of the permalloy bath for multilayer electrodeposition required the addition of a nonmagnetic metal salt, in this case CuSO_4 . By pulsing the potential, the less noble element, Cu, will deposit, while the higher potential will deposit the Cu along with the $\text{Ni}_{80}\text{Fe}_{20}$. As a result the Cu was added in much smaller concentrations to the bath and resulting NiFeCu composition was analyzed by AAS (Figure 2A.3). The line scan voltammograms and polarization curves (Figure A2.4) were subsequently conducted with the different $[\text{Cu}^{+2}]$ to determine relative deposition rates and potential windows for Cu electrodeposition. The polarization curves indicate that a potential of -0.48V vs. SCE produced a positive current for a 1mM Cu, indicating a potential minimum for Cu deposition as less negative potentials would cause dissolution of the electrodeposit. This value is larger than thin film multilayer potentials suggesting a decreased diffusivity for Cu^{+2} with the template. A potential of 0.6V vs. SCE was therefore used for Cu electrodeposition.

Utilizing a pulsed electrodeposition potential of -1.2V and -0.6V vs. SCE with a charge density of 0.1204 and 0.03896 C/cm^2 , respectively, the $\text{Ni}_{80}\text{Fe}_{20}/\text{Cu}$ multilayers were deposited from baths of 1, 5, and 10mM Cu^{+2} . The chronopotentiogram is shown in Figure A2.5. The SEM images of these nanowires with 10 bilayers each are shown in

Figure A2.6. The Cu layers were selectively etched for clarity with 0.04M $K_2CR_2O_7$ + 0.36M H_2SO_4 + 0.012M HCl. As a result the Cu layers appear darker than $Ni_{80}Fe_{20}$. Much finer multilayered structures were also prepared by reducing the charge to density 0.01204 and 0.003896 C/cm^2 . These results are shown by SEM with selective etching and TEM (Figure A2.7). The growth rates extracted from TEM micrographs are 7nm/sec and 0.23nm/sec for $Ni_{80}Fe_{20}$ and Cu, respectively. Both the TEM and SEM images illustrate a wavy layer formation. This may be a consequence of irregular etching during the potential drop from $Ni_{80}Fe_{20}$ to Cu electrodeposition and may possibly be mitigated by breaks between layer depositions. A troubled interface between the $Ni_{80}Fe_{20}/Cu$ multilayers and the Au segment is also noticeable from SEM and TEM images. The compromised interface is a result of the high pH of the Au solution (7.0) similar to that of Appendix 1, but is exacerbated by the presence and low corrosion resistance of Fe.

Although $Ni_{80}Fe_{20}/Cu$ multilayer nanowires could not be fabricated with Au ends for contact, single nanowires were assembled by A.C. dielectrophoretic alignment and contacted by annealing at 300°C for 1hr. The fabricated device is shown in Figure A2.8 with its corresponding magneto-transport response. The nanowire displays very evident lamellar features by SEM alone, probably due to Kirkendall diffusion of Cu into the $Ni_{80}Fe_{20}$ layer. Although the MR response is only 0.5% it follows the trend expected for $Ni_{80}Fe_{20}/Cu$ nanowires. The signal may have been reduced by contact resistance and inter-layer diffusion.

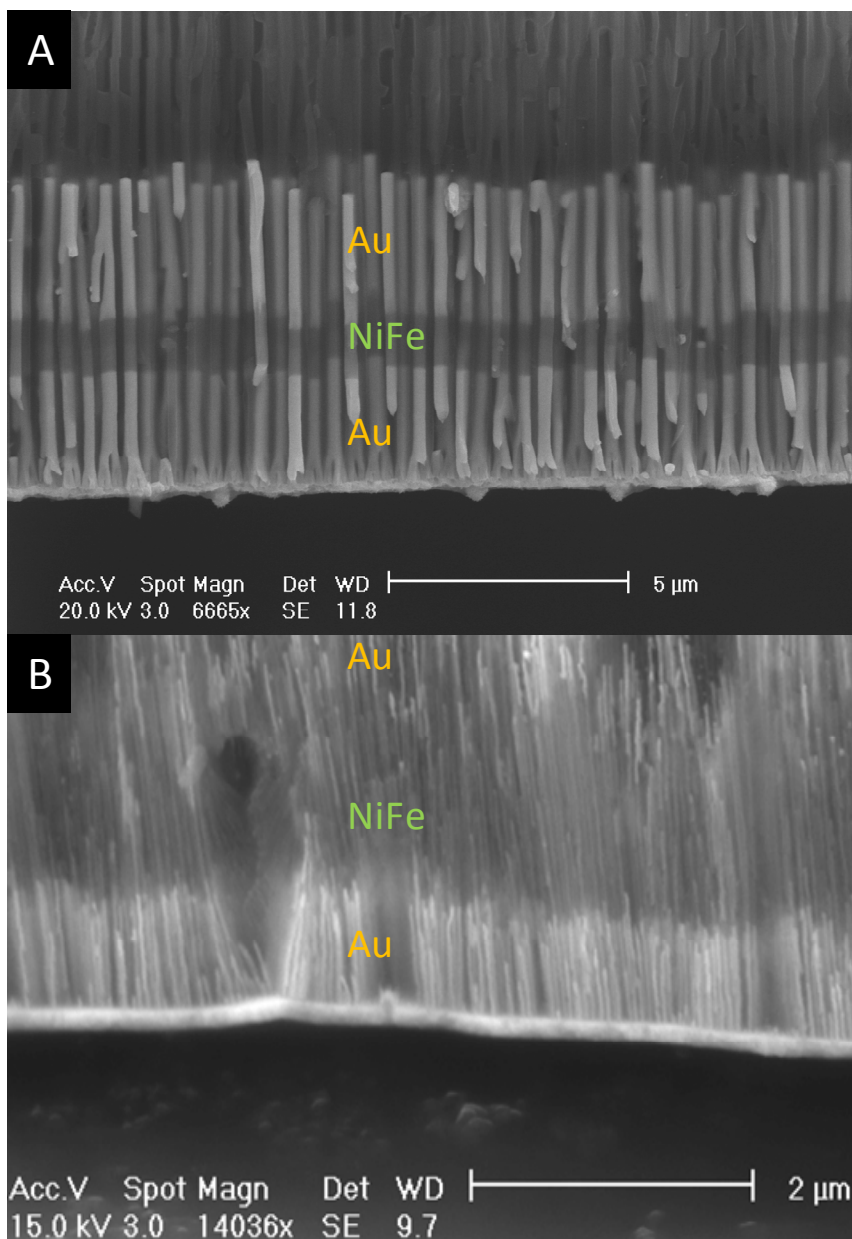


Figure A1.1: SEM images of (A) 200nm and (B) 30nm Au/NiFe/Au nanowires embedded in an alumina template.

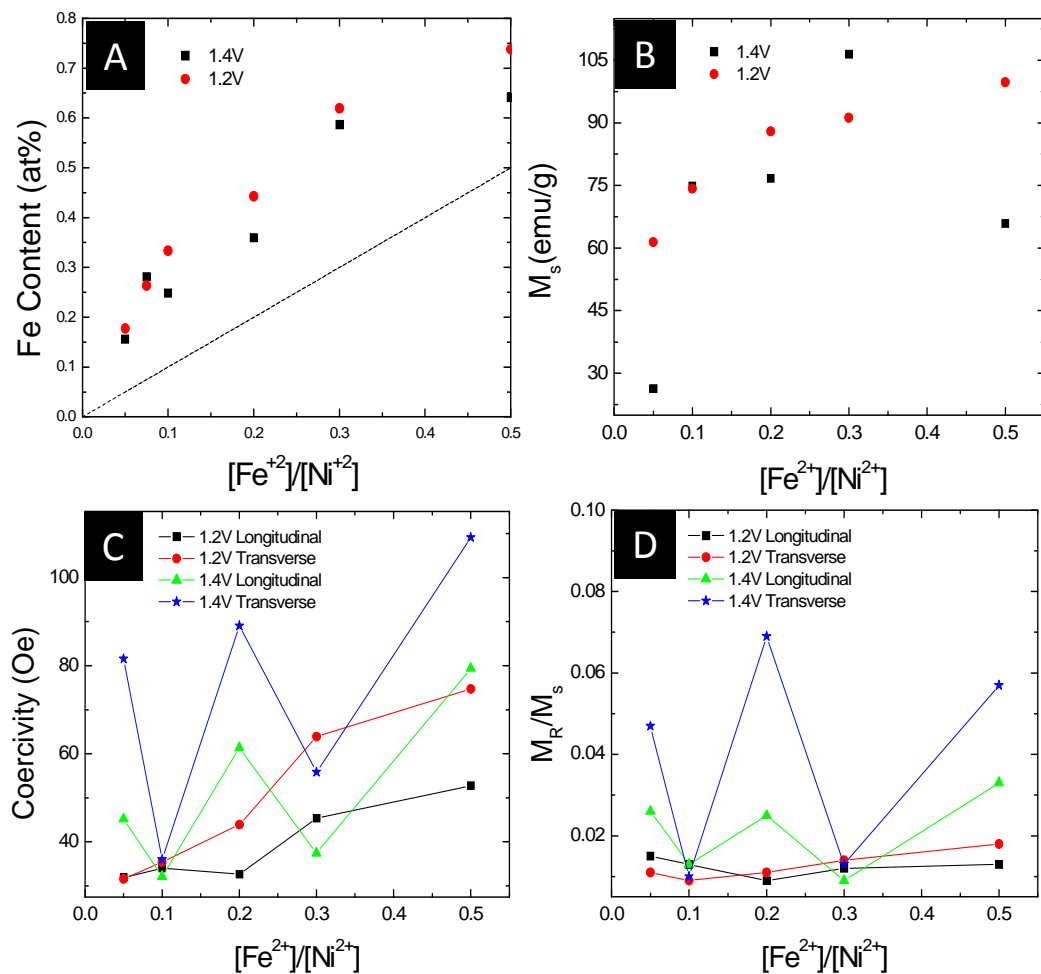


Figure A1.2: (A) Fe content, (B) magnetization saturation, (C) coercivity, and (D) squareness (M_S/M_R) as a function of the $[\text{Fe}^{2+}]/[\text{Ni}^{2+}]$ ratio in the electrodeposition bath for $1\mu\text{m}$ NiFe nanowires electrodeposited at 1.4 and 1.2 V.

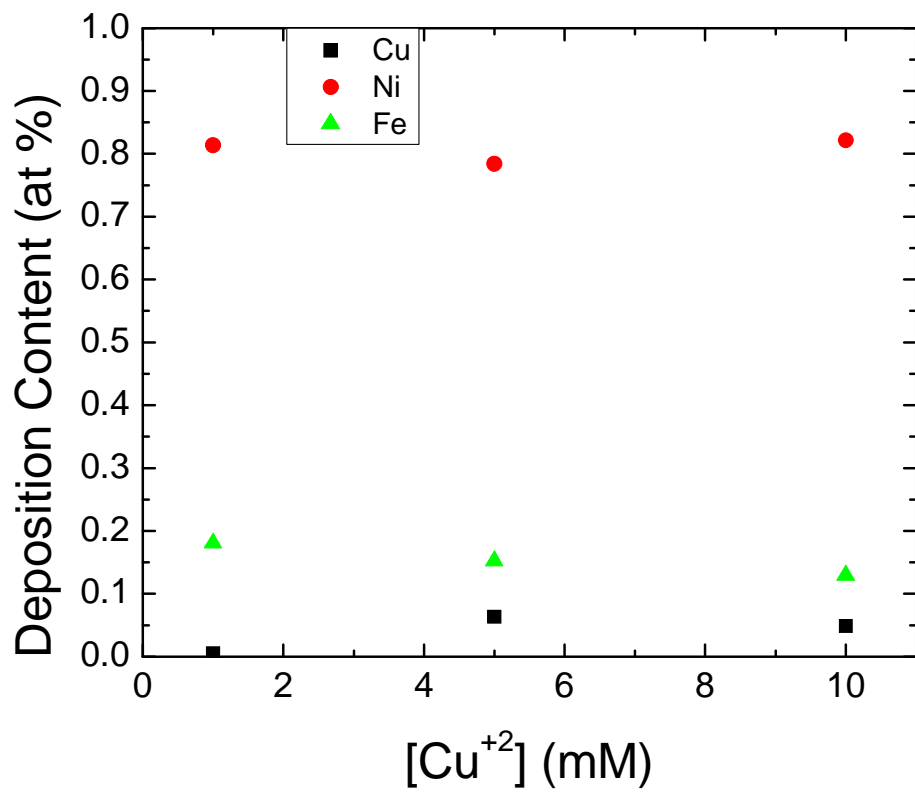


Figure A1.3: The deposition content as a function of the [Cu²⁺] for NiFe/Cu multilayer baths.

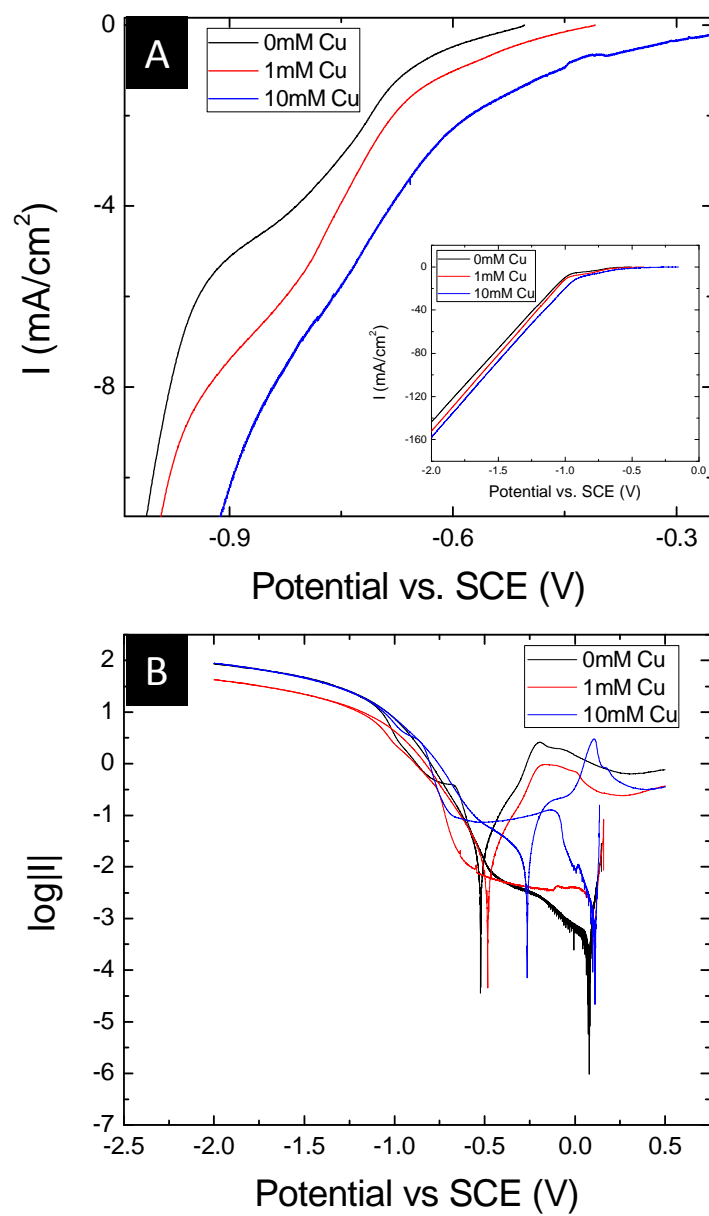


Figure A1.4: (A) Linear sweep voltammogram and for the permalloy bath with 0, 1, and 10mM Cu⁺². The inset contains the full potential range of the voltammogram. (B) The polarization curve (semi-log plot) of the current density as function of the potential is used to determine the range of Cu electrodeposition.

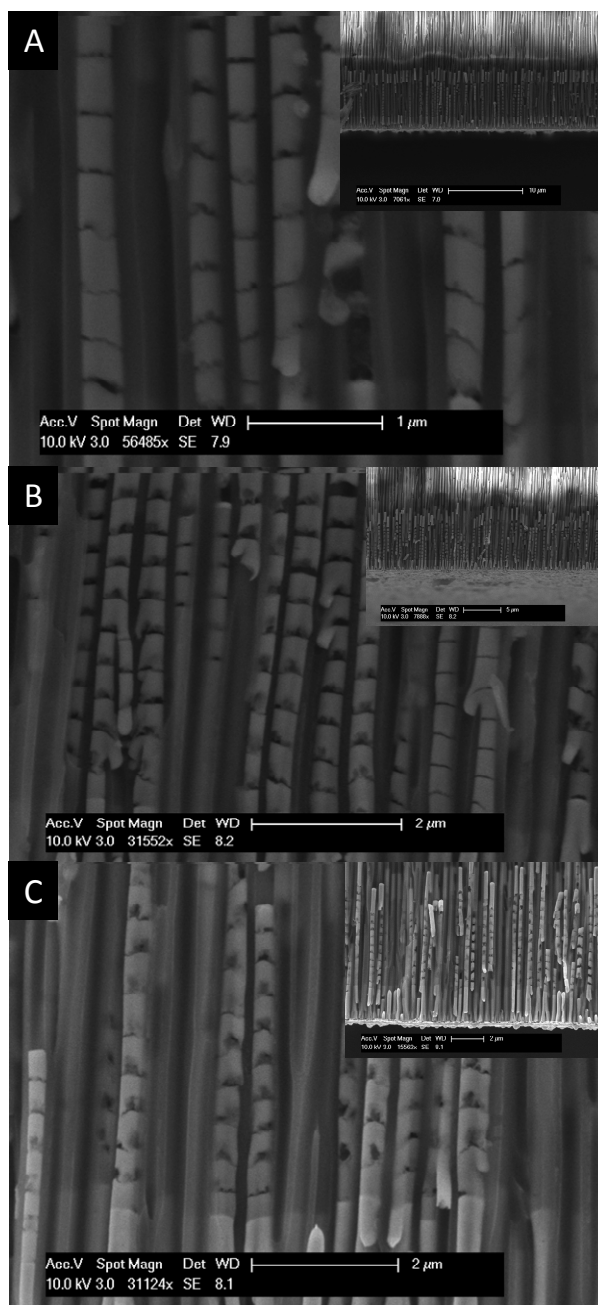


Figure A1.5: SEM images of $\text{Ni}_{80}\text{Fe}_{20}/\text{Cu}$ multilayer nanowires electrodeposited with a charge density of 0.1204 and 0.03896 C/cm^2 , respectively, from baths with (A) 1, (B) 5, and (C) 10mM $[\text{Cu}^{+2}]$. The Cu was selectively etched to permit layers to be distinguished. The insets contain lower magnification of template cross-section for the same sample. The scale bars are (A) 1 and (B-C) 2 μm .

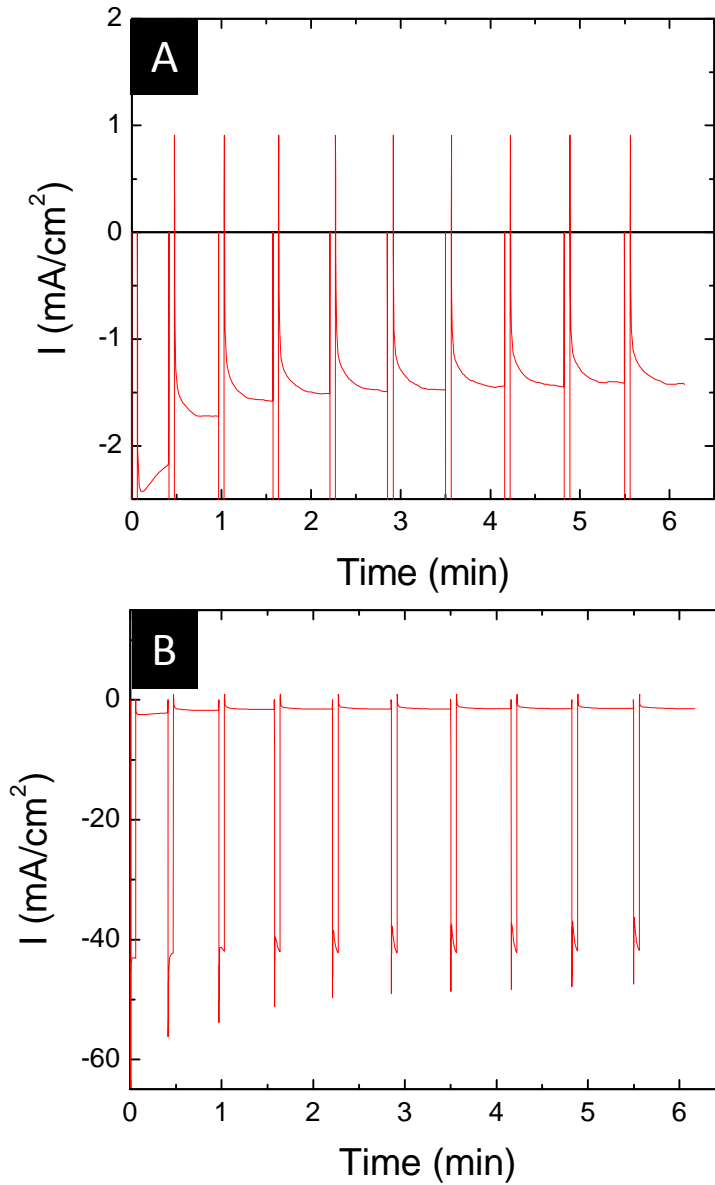


Figure A1.6: The chronopotentiogram for Ni₈₀Fe₂₀/Cu multilayer electrodeposition shown at (A) small and (B) large current density scales for Cu and Ni₈₀Fe₂₀, respectively.

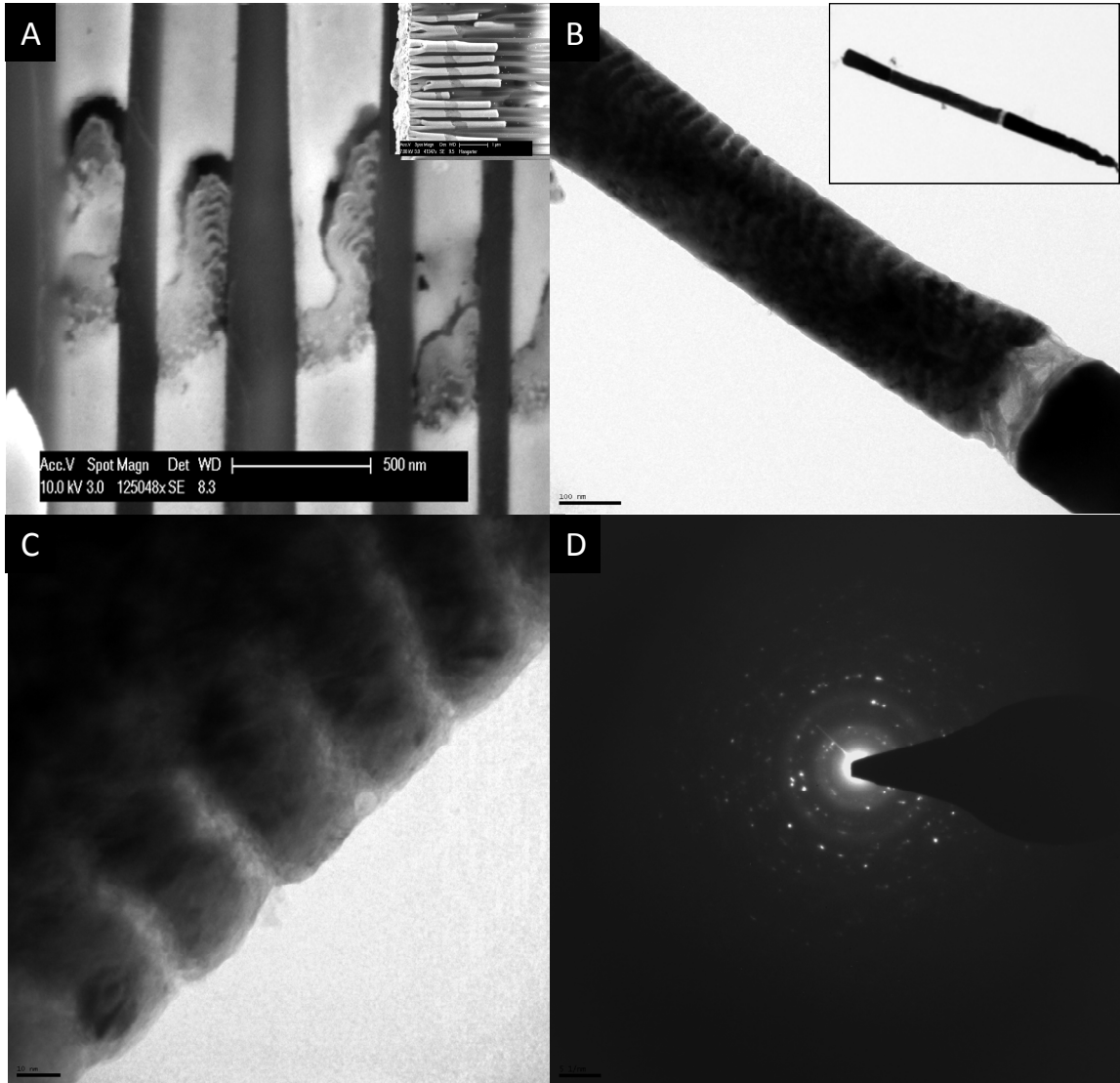


Figure A1.7: (A) SEM and (B-C) TEM images of $\text{Ni}_{80}\text{Fe}_{20}/\text{Cu}$ multilayer nanowires electrodeposited with a charge density of 0.01204 and 0.003896 C/cm^2 , respectively. The Cu was selectively etched in (A) to permit layers to be distinguished. The insets contain lower magnification of the same (A) template cross-section and (B) single nanowire sample. The scale bars are (A) 500 , (B) 100 , and (C) 10nm . (D) The SAED pattern corresponds to wire in (C).

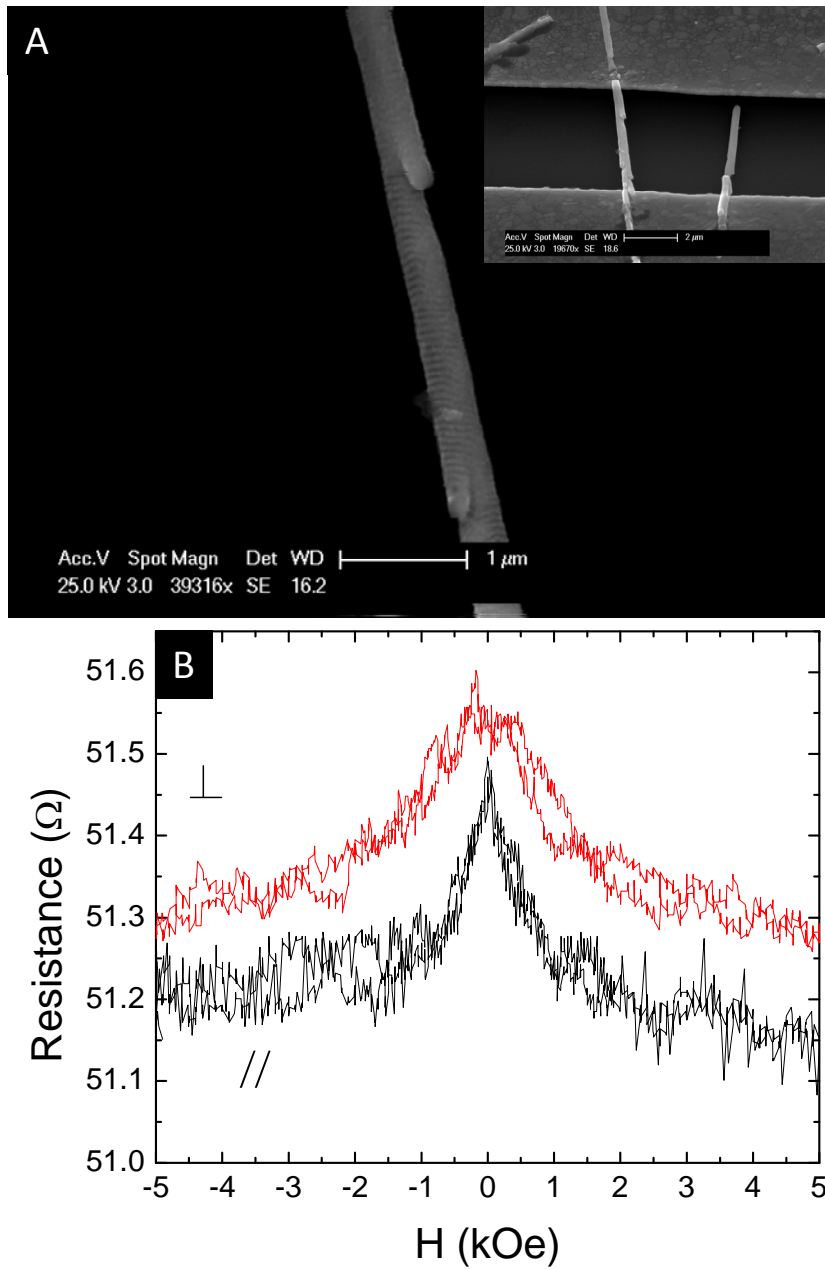


Figure A1.8: (A) SEM image of a single $\text{Ni}_{80}\text{Fe}_{20}/\text{Cu}$ multilayer nanowire device. The inset is a lower magnification image of the device. (B) The magnetoresistance profile of the device.

References

1. W. E. Buhro and V. L. Colvin, *Nature Materials*, 2003, **2**, 138-139.
2. H. Yu, J. B. Li, R. A. Loomis, L. W. Wang and W. E. Buhro, *Nature Materials*, 2003, **2**, 517-520.
3. L. J. Lauhon, M. S. Gudixsen and C. M. Lieber, *Philosophical Transactions of the Royal Society of London Series a-Mathematical Physical and Engineering Sciences*, 2004, **362**, 1247-1260.
4. F. Qian, Y. Li, S. Gradecak, D. L. Wang, C. J. Barrelet and C. M. Lieber, *Nano Letters*, 2004, **4**, 1975-1979.
5. Y. Wu, J. Xiang, C. Yang, W. Lu and C. M. Lieber, *Nature*, 2004, **430**, 704-704.
6. M. D. Stiles, *Physical Review B*, 1993, **48**, 7238-7259.
7. Y. F. Lin and W. B. Jian, *Nano Letters*, 2008, **8**, 3146-3150.
8. A. G. MacDiarmid, *Angewandte Chemie-International Edition*, 2001, **40**, 2581-2590.
9. B. Dong, N. Lu, M. Zelsmann, N. Kehagias, H. Fuchs, C. M. S. Torres and L. F. Chi, *Advanced Functional Materials*, 2006, **16**, 1937-1942.
10. H. Q. Liu, J. Kameoka, D. A. Czaplewski and H. G. Craighead, *Nano Letters*, 2004, **4**, 671-675.
11. I. Heller, A. M. Janssens, J. Mannik, E. D. Minot, S. G. Lemay and C. Dekker, *Nano Letters*, 2008, **8**, 591-595.
12. P. R. Nair and M. A. Alam, *Applied Physics Letters*, 2006, **88**, -.
13. S. Krishnamoorthy, R. Pugin, J. Brugger, H. Heinzelmann, A. C. Hoogerwerf and C. Hinderling, *Langmuir*, 2006, **22**, 3450-3452.
14. B. Li, S. Santhanam, L. Schultz, M. Jeffries-EL, M. C. Iovu, G. Sauve, J. Cooper, R. Zhang, J. C. Revelli, A. G. Kusne, J. L. Snyder, T. Kowalewski, L. E. Weiss, R. D. McCullough, G. K. Fedder and D. N. Lambeth, *Sensors and Actuators B-Chemical*, 2007, **123**, 651-660.
15. V. Svetlicic, A. J. Schmidt and L. L. Miller, *Chemistry of Materials*, 1998, **10**, 3305-+.

16. C. K. Tan and D. J. Blackwood, *Sensors and Actuators B-Chemical*, 2000, **71**, 184-191.
17. J. X. Huang and R. B. Kaner, *Angewandte Chemie-International Edition*, 2004, **43**, 5817-5821.
18. W. S. Huang, B. D. Humphrey and A. G. Macdiarmid, *Journal of the Chemical Society-Faraday Transactions I*, 1986, **82**, 2385-&.
19. S. Virji, J. X. Huang, R. B. Kaner and B. H. Weiller, *Nano Letters*, 2004, **4**, 491-496.
20. J. Huang, S. Virji, B. H. Weiller and R. B. Kaner, *Chemistry-a European Journal*, 2004, **10**, 1315-1319.
21. J. X. Huang and R. B. Kaner, *Journal of the American Chemical Society*, 2004, **126**, 851-855.
22. J. X. Huang, S. Virji, B. H. Weiller and R. B. Kaner, *Journal of the American Chemical Society*, 2003, **125**, 314-315.
23. K. Ramanathan, M. A. Bangar, M. H. Yun, W. F. Chen, A. Mulchandani and N. V. Myung, *Nano Letters*, 2004, **4**, 1237-1239.
24. M. M. Alam, J. Wang, Y. Y. Guo, S. P. Lee and H. R. Tseng, *Journal of Physical Chemistry B*, 2005, **109**, 12777-12784.
25. M. D. Shirsat, M. A. Bangar, M. A. Deshusses, N. V. Myung and A. Mulchandani, *Applied Physics Letters*, 2009, **94**, -.
26. S. C. Hernandez, D. Chaudhuri, W. Chen, N. V. Myung and A. Mulchandani, *Electroanalysis*, 2007, **19**, 2125-2130.
27. M. A. Bangar, C. M. Hangarter, B. Yoo, Y. Rheem, W. Chen, A. Mulchandani and N. V. Myung, *Electroanalysis*, 2009, **21**, 61-67.
28. R. M. Hernandez, L. Richter, S. Semancik, S. Stranick and T. E. Mallouk, *Chemistry of Materials*, 2004, **16**, 3431-3438.
29. Y. P. Dan, Y. Y. Cao, T. E. Mallouk, A. T. Johnson and S. Evoy, *Sensors and Actuators B-Chemical*, 2007, **125**, 55-59.
30. Y. Cao, A. E. Kovalev, R. Xiao, J. Kim, T. S. Mayer and T. E. Mallouk, *Nano Letters*, 2008, **8**, 4653-4658.

31. B. Dong, M. Krutschke, X. Zhang, L. F. Chi and H. Fuchs, *Small*, 2005, **1**, 520-524.
32. B. Dong, D. Y. Zhong, L. F. Chi and H. Fuchs, *Advanced Materials*, 2005, **17**, 2736-+.
33. Z. J. Hu, B. Muls, L. Gence, D. A. Serban, J. Hofkens, S. Melinte, B. Nysten, S. Demoustier-Champagne and A. M. Jonas, *Nano Letters*, 2007, **7**, 3639-3644.
34. Y. S. Jung, W. Jung, H. L. Tuller and C. A. Ross, *Nano Letters*, 2008, **8**, 3776-3780.
35. B. W. Maynor, S. F. Filocamo, M. W. Grinstaff and J. Liu, *Journal of the American Chemical Society*, 2002, **124**, 522-523.
36. M. Yang, P. E. Sheehan, W. P. King and L. J. Whitman, *Journal of the American Chemical Society*, 2006, **128**, 6774-6775.
37. J. L. Duvail, Y. Z. Long, S. Cuenot, Z. J. Chen and C. Z. Gu, *Applied Physics Letters*, 2007, **90**, -.
38. J. L. Duvail, P. Retho, V. Fernandez, G. Louarn, P. Molinie and O. Chauvet, *Journal of Physical Chemistry B*, 2004, **108**, 18552-18556.
39. Y. Chen and Y. Luo, *Advanced Materials*, 2009, **21**, 2040.
40. T. S. Hansen, A. E. Daugaard, S. Hvilsted and N. B. Larsen, *Advanced Materials*, 2009, **21**, 1-4.
41. S. S. P. Parkin, *Physical Review Letters*, 1993, **71**, 1641-1644.
42. F. J. Jedema, A. T. Filip and B. J. van Wees, *Nature*, 2001, **410**, 345-348.
43. J. C. Slonczewski, *Journal of Magnetism and Magnetic Materials*, 1996, **159**, L1-L7.
44. A. A. Tulapurkar, Y. Suzuki, A. Fukushima, H. Kubota, H. Maehara, K. Tsunekawa, D. D. Djayaprawira, N. Watanabe and S. Yuasa, *Nature*, 2005, **438**, 339-342.
45. M. Steiner, G. Meier, U. Merkt and J. Nitta, *Physica E-Low-Dimensional Systems & Nanostructures*, 2004, **24**, 124-128.
46. M. Steiner and J. Nitta, *Applied Physics Letters*, 2004, **84**, 939-941.

47. D. M. Davis, M. Moldovan, D. P. Young, M. Henk, X. G. Xie and E. J. Podlaha, *Electrochemical and Solid State Letters*, 2006, **9**, C153-C155.
48. M. Jung, J. S. Lee, W. Song, Y. H. Kim, S. D. Lee, N. Kim, J. Park, M. S. Choi, S. Katsumoto, H. Lee and J. Kim, *Nano Letters*, 2008, **8**, 3189-3193.
49. M. S. Dresselhaus, G. Chen, M. Y. Tang, R. G. Yang, H. Lee, D. Z. Wang, Z. F. Ren, J. P. Fleurial and P. Gogna, *Advanced Materials*, 2007, **19**, 1043-1053.
50. M. S. Hu, H. L. Chen, C. H. Shen, L. S. Hong, B. R. Huang, K. H. Chen and L. C. Chen, *Nature Materials*, 2006, **5**, 102-106.
51. W. Kim, J. Zide, A. Gossard, D. Klenov, S. Stemmer, A. Shakouri and A. Majumdar, *Phys Rev Lett*, 2006, **96**, -.
52. S. Mubeen, T. Zhang, B. Yoo, M. A. Deshusses and N. V. Myung, *Journal of Physical Chemistry C*, 2007, **111**, 6321-6327.
53. S. A. Maier, P. G. Kik, H. A. Atwater, S. Meltzer, E. Harel, B. E. Koel and A. A. G. Requicha, *Nature Materials*, 2003, **2**, 229-232.
54. L. F. Liu, W. Lee, R. Scholz, E. Pippel and U. Gosele, *Angewandte Chemie-International Edition*, 2008, **47**, 7004-7008.
55. S. Jin, D. M. Whang, M. C. McAlpine, R. S. Friedman, Y. Wu and C. M. Lieber, *Nano Letters*, 2004, **4**, 915-919.
56. H. K. Ye, Z. Y. Gu, T. Yu and D. H. Gracias, *IEEE Transactions on Nanotechnology*, 2006, **5**, 62-66.
57. N. A. Melosh, A. Boukai, F. Diana, B. Gerardot, A. Badolato, P. M. Petroff and J. R. Heath, *Science*, 2003, **300**, 112-115.
58. B. Y. Yoo, Y. W. Rheem, W. P. Beyermann and N. V. Myung, *Nanotechnology*, 2006, **17**, 2512-2517.
59. E. W. H. Jager, E. Smela and O. Inganäs, *Science*, 2000, **290**, 1540-1545.
60. E. Smela, *Journal of Micromechanics and Microengineering*, 1999, **9**, 1-18.
61. S. Ingole, P. Aella, S. J. Herne and P. S. T, *Applied Physics Letters*, 2007, **91**, 3.
62. C. R. Martin, *Science*, 1995, **266**, 1961-1966.
63. C. R. Martin, R. Parthasarathy and V. Menon, *Electrochimica Acta*, 1994, **39**, 1309-1313.

64. E. L. Kupila and J. Kankare, *Synthetic Metals*, 1995, **69**, 383-384.
65. L. H. Dall'Antonia, M. E. Vidotti, S. I. C. de Torresi and R. M. Torresi, *Electroanalysis*, 2002, **14**, 1577-1586.
66. T. Zhang, S. Mubeen, E. Bekyarova, B. Y. Yoo, R. C. Haddon, N. V. Myung and M. A. Deshusses, *Nanotechnology*, 2007, **18**, -.
67. R. J. Tseng, C. O. Baker, B. Shedd, J. X. Huang, R. B. Kaner, J. Y. Ouyang and Y. Yang, *Applied Physics Letters*, 2007, **90**, -.
68. A. C. C. Tseung and K. Y. Chen, *Catalysis Today*, 1997, **38**, 439-443.
69. K. Potje-Kamloth, *Chemical Reviews*, 2008, **108**, 367-399.
70. G. K. Chandler and D. Pletcher, *Journal of Applied Electrochemistry*, 1986, **16**, 62-68.
71. G. L. Duffitt and P. G. Pickup, *Journal of the Chemical Society-Faraday Transactions*, 1992, **88**, 1417-1423.
72. Y. Berdichevsky and Y. H. Lo, *Advanced Materials*, 2006, **18**, 122-125.
73. M. M. Baum, E. S. Kiyomiya, S. Kumar, A. M. Lappas, V. A. Kapinus and H. C. Lord, *Environmental Science & Technology*, 2001, **35**, 3735-3741.
74. N. M. Ratcliffe, *Analytica Chimica Acta*, 1990, **239**, 257-262.
75. S. Krogan, *Electronic Noise and Fluctuations in Solids*, Cambridge University Press, New York, 1996.
76. L. Torsi, M. Pezzuto, P. Siciliano, R. Rella, L. Sabbatini, L. Valli and P. G. Zambonin, *Sensors and Actuators, B*, 1998, **48**, 362-367.
77. J. Janata and M. Josowicz, *Nature Materials*, 2003, **2**, 19-24.
78. W. Brutting, H. Riel, T. Beierlein and W. Riess, *Journal of Applied Physics*, 2001, **89**, 1704-1712.
79. N. I. Kovtyukhova, B. R. Martin, J. K. N. Mbindyo, T. E. Mallouk, M. Cabassi and T. S. Mayer, *Materials Science & Engineering C-Biomimetic and Supramolecular Systems*, 2002, **19**, 255-262.
80. H. Nagase, K. Wakabayashi and T. Imanaka, *Sensors and Actuators B-Chemical*, 1993, **14**, 596-597.

81. V. C. Nguyen and K. Potje-Kamloth, *Thin Solid Films*, 1999, **338**, 142-148.
82. Y. Huang, X. F. Duan, Q. Q. Wei and C. M. Lieber, *Science*, 2001, **291**, 630-633.
83. M. A. Bangar, D. J. Shirale, W. Chen, N. V. Myung and A. Mulchandani, *Analytical Chemistry*, 2009, **81**, 2168-2175.
84. C. M. Hangarter, M. Bangar, S. C. Hernandez, W. Chen, M. A. Deshusses, A. Mulchandani and N. V. Myung, *Applied Physics Letters*, 2008, **92**, -.
85. F. Jonas and L. Schrader, *Synthetic Metals*, 1991, **41**, 831-836.
86. M. Dietrich, J. Heinze, G. Heywang and F. Jonas, *Journal of Electroanalytical Chemistry*, 1994, **369**, 87-92.
87. G. Heywang and F. Jonas, *Advanced Materials*, 1992, **4**, 116-118.
88. B. L. Groenendaal, F. Jonas, D. Freitag, H. Pielartzik and J. R. Reynolds, *Advanced Materials*, 2000, **12**, 481-494.
89. G. A. Sotzing, J. R. Reynolds and P. J. Steel, *Advanced Materials*, 1997, **9**, 795-&.
90. A. Zykwinska, W. Domagala, B. Pilawa and A. Lapkowski, *Electrochimica Acta*, 2005, **50**, 1625-1633.
91. R. Xiao, S. Il Cho, R. Liu and S. B. Lee, *Journal of the American Chemical Society*, 2007, **129**, 4483-4489.
92. L. Niu, C. Kvarnstrom, K. Froberg and A. Ivaska, *Synthetic Metals*, 2001, **122**, 425-429.
93. A. R. Hillman and E. F. Mallen, *Journal of Electroanalytical Chemistry*, 1987, **220**, 351-367.
94. S. G. Im and K. K. Gleason, *Macromolecules*, 2007, **40**, 6552-6556.
95. S. G. Im, E. A. Olivetti and K. K. Gleason, *Surface & Coatings Technology*, 2007, **201**, 9406-9412.
96. R. H. Baughman and L. W. Shacklette, *Journal of Chemical Physics*, 1989, **90**, 7492-7504.
97. A. N. Aleshin, S. R. Williams and A. J. Heeger, *Synthetic Metals*, 1998, **94**, 173-177.

98. B. G. Streetman and S. K. Banerjee, *Solid State Electronic Devices*, Pearson Prentice Hall, Upper Saddle River, 2006.
99. F. Tran-Van, S. Garreau, G. Louarn, G. Froyer and C. Chevrot, *Synthetic Metals*, 2001, **119**, 381-382.
100. F. Tran-Van, S. Garreau, G. Louarn, G. Froyer and C. Chevrot, *Journal of Materials Chemistry*, 2001, **11**, 1378-1382.
101. H. Mao, X. F. Lu, D. M. Chao, L. L. Cui and W. J. Zhang, *Materials Letters*, 2008, **62**, 2543-2546.
102. D. Blackwood and M. Josowicz, *Journal of Physical Chemistry*, 1991, **95**, 493-502.
103. L. I. Ahmed, *Journal of Physics and Chemistry of Solids*, 1968, **29**, 1653-&.
104. J. Janata and M. Josowicz, *Accounts of Chemical Research*, 1998, **31**, 241-248.
105. J. S. Huang, P. F. Miller, J. S. Wilson, A. J. de Mello, J. C. de Mello and D. D. C. Bradley, *Advanced Functional Materials*, 2005, **15**, 290-296.
106. S. A. Wolf, D. D. Awschalom, R. A. Buhrman, J. M. Daughton, S. von Molnar, M. L. Roukes, A. Y. Chtchelkanova and D. M. Treger, *Science*, 2001, **294**, 1488-1495.
107. T. Valet and A. Fert, *Journal of Magnetism and Magnetic Materials*, 1993, **121**, 378-382.
108. T. Valet and A. Fert, *Physical Review B*, 1993, **48**, 7099-7113.
109. G. A. Prinz, *Science*, 1998, **282**, 1660-1663.
110. D. D. Awschalom and M. E. Flatte, *Nature Physics*, 2007, **3**, 153-159.
111. Y. Rheem, B. Y. Yoo, W. P. Beyermann and N. V. Myung, *Nanotechnology*, 2007, **18**, -.
112. J. Escrig, P. Landeros, D. Altbir, E. E. Vogel and P. Vargas, *Journal of Magnetism and Magnetic Materials*, 2007, **308**, 233-237.
113. R. M. Bozorth, *Ferromagnetism*, IEEE Press, Piscataway, N.J., 1993.
114. K. Sekiguchi, E. Saitoh and H. Miyajima, *Journal of Applied Physics*, 2005, **97**, -.
115. J. A. Sioss and C. D. Keating, *Nano Letters*, 2005, **5**, 1779-1783.

116. Y. Qin, L. F. Liu, R. B. Yang, U. Gosele and M. Knez, *Nano Letters*, 2008, **8**, 3221-3225.
117. F. Xiao, B. Yoo, K. H. Lee and N. V. Myung, *Journal of the American Chemical Society*, 2007, **129**, 10068-+.
118. Y. G. Sun, B. T. Mayers and Y. N. Xia, *Nano Letters*, 2002, **2**, 481-485.
119. Y. G. Sun, B. Mayers and Y. N. Xia, *Advanced Materials*, 2003, **15**, 641-646.
120. Y. G. Sun, B. Wiley, Z. Y. Li and Y. N. Xia, *Journal of the American Chemical Society*, 2004, **126**, 9399-9406.
121. Y. G. Sun and Y. N. Xia, *Advanced Materials*, 2004, **16**, 264-+.
122. R. F. Bunshah, *Deposition technologies for films and coatings : developments and applications*, Noyes Publications, Park Ridge, N.J., U.S.A., 1982.
123. Y. Rheem, C. H. Chang, K.-H. Lee, C. M. Hangarter and N. V. Myung, *Submitted*, 2009.
124. M. S. Baba, R. Viswanathan and C. K. Mathews, *Rapid Communications in Mass Spectrometry*, 1996, **10**, 691-698.